

FLASH SINTERING TECHNIQUES FOR RAPID AND SUSTAINABLE  
METAL PROCESSING AT ROOM TEMPERATURE

by

EMMANUEL ANUOLUWA BAMIDELE

B.ENG., Metallurgical and Materials Engineering  
Federal University of Technology Akure, 2015

MS., Materials Science and Engineering  
University of Colorado Boulder, 2021

A thesis submitted to the  
Faculty of Graduate School of the  
University of Colorado in partial fulfilment  
of the requirement for the degree of  
Doctor of Philosophy  
Materials Science and Engineering Program

2023

Committee Members

Prof. Rishi Raj (Chair)

Prof. Alan Weimer

Prof. Wil V Srubar

Prof. Gregory Whiting

Dr. Jhonathan Rosales

## ABSTRACT

Bamidele, Emmanuel Anuoluwa (Ph.D., Materials Science and Engineering)

Flash Sintering Techniques for Rapid and Sustainable Metal Processing at Room Temperature

Thesis directed by Professor Rishi Raj

Flash sintering has gained significant attention since it was first discovered in 2010, however, no study has conclusively studied the flash sintering of metal. The present study applied flash sintering technique to achieve rapid and sustainable sintering of metals including tungsten (W), nickel (Ni), and rhenium (Re).

While ceramics require furnace heating to initiate flash sintering, metals do not. They can be sintered at room temperature by direct injection of current. Nevertheless, the experiment performed with tungsten presented results with and without a furnace, while nickel and rhenium were sintered without furnace. In all cases, sintering occurs when the specimen temperature is around 1000°C.

The pattern of flash sintering is similar in all the metals studied. The resistivity behavior when plotted as a function of temperature show similar behavior. The general features observed are as follow: (i) an incubation period where electric voltage breakdown is observed as inter-particle contact are established (ii) followed by the initiation of electroluminescence which has been seen between 5 and 7 A mm<sup>-2</sup> in all metals. This optical emission signals the onset of flash characterized by a plateau in temperature and generation of defects. (iii) Finally, the temperature surges and abrupt sintering follows between 20 and 24 A mm<sup>-2</sup>.

The role of large defect generation was emphasized in each of the metals studied – Ni, W, and Re. The difference between the input electrical energy and energy loss to black body radiation, convection and specific heat was calculated, and termed “energy deficit”. The energy deficit was divided by the formation enthalpy of the metal to obtain the mol fraction of Frenkel pairs generated during the flash sintering process. Point Defect estimated include 26mol% for W, 14 mol% for Re and 0.3-0.4 mol% for Ni. These values are several orders of magnitude higher than what is expected from thermal equilibrium.

The result of variation of current rate in W and Ni studies showed that sintering depends on current density and not current rate. This result was rationalized by recognizing that the rate of mass transport by diffusion depends on the product of the defect concentration and the mobility of defects. If the defect concentration is large, then it may weaken the influence of mobility on the rate of mass transport. Since the defect concentration depends on the current density, it can be postulated that sintering will also predominantly depend on the current density.

Comparison of the energy consumption during the flash sintering process and alternative sintering methods showed that flash sintering has less energy footprint. This study associates this energy efficiency to the controllable direct injection of current into the specimen without any barrier or need for furnace heating, which is paramount in the alternative sintering methods.

Finally, exploratory studies have shown the potential of metal flash sintering technique in several areas of applications such as additive manufacturing, surface coating/modification and alloy/composite fabrication. Importantly, Integrating flash sintering into metal additive manufacturing will enable rapid and more sustainable manufacturing of end-user components.

## DEDICATION

This thesis is lovingly dedicated to the memory of father, Mr. Joel Akinlolu Bamidele who passed away on November 10, 2021.

His unwavering support, attentive listening, continuous encouragement, and boundless fount of ideas/examples were instrumental throughout the course of my doctoral journey.

## ACKNOWLEDGEMENT

The success of this thesis was possible due to the support of Prof. Rishi Raj. As my advisor and a respected affiliate of Materials Science and Engineering, his meticulous guidance, timely corrections, and invaluable insights have been helpful. I would also like to thank every other member of my committee. Prof. Weimer's pivotal role as a PI in the NASA ESI grant that supported my research, coupled with his critical questioning and insights during exams and meetings are greatly appreciated. Dr. Jhonathan Rosales from the NASA Marshall Space Flight Center was instrumental with his monthly feedback, his assistance with the LECO oxygen analysis for tungsten, and collaborative efforts comparing various sintering techniques. I thank Prof. Wil Srubar for always extending a welcoming hand, be it for project discussions or examination scheduling/preparations. I would also like to thank Prof. Gregory Whiting for demonstrating understanding and commitment when called upon.

I greatly appreciate the grant provided by the National Aeronautics and Space Administration – Early-Stage Innovation (NASA-ESI) that supported my tuition, stipends and equipment purchase for the duration of my doctoral studies.

Dr. Syed Jalali's involvement during his time in our lab as a post-doc in 2021 played a crucial role in kick-starting several projects. His discussions on methodologies and proactive approach to resolving lab-related challenges were a tremendous asset. My learning curve was significantly enhanced by the hands-on training provided by the Colorado Shared Instrumentation for Nanofabrication and Characterization (COSINC), Idea Forge, and Integrated Teaching and Learning Laboratory (ITLL), therefore, I appreciate these facilities and their staff.

Deep appreciation is extended to my past advisors, Prof. John Ade Ajayi and Prof. Elizabeth Makhatha. Prof. Ade Ajayi, in particular, has been a father figure since my undergraduate days,

guiding and inspiring me every step of the way. Amidst academic rigors, the genuine support from friends such as Oluwaniyi Ajiteru, Oluwafemi Sanumi, Ahmed Ijaola, Afure Martha Oyibo, Orimoloye Ifeoluwa was a consistent source of strength. Further bolstering my journey were the invaluable guidance from my mentor, Dr. Bodunrin Michael, and the collaboration with Prof. Baowen Li. Special thanks to my graduate school applications reviewers, Dr. Koby Sarpong and Dr. Samuel Nunoo. I thank Prof Baowen Li, Prof Charles Wyatt Shield, Dr Ovie Ohimo and Prof Eylem Asmatulu for writing my EB2-NIW recommendation letters.

To the leaders of the Materials Science and Engineering program, notably Prof. Robert McLeod, Prof. Tanja Cuk, Prof. Stephanie Bryant, Alex Schultz, and Laramie Rose, I am deeply grateful. Their encouragement and support have been cornerstones of my academic journey.

My family has been my grounding force throughout this voyage. Their steadfast support, patience, and belief in my vision have been the backbone of my perseverance. I owe a particular debt of gratitude to my uncle, Tunde Olaoye. Since my move to the USA, he has been an anchor, always extending support and guidance. Additionally, my heartfelt appreciation goes to Mark, Heather, Michael, and Caleb Perrys, also Kevin and Natalie Clark's family. Their warmth and open arms, treating me as family, have provided much-needed solace and support during my stay in Colorado.

I would like to thank all my past and present lab mates, Dr. Camilla Uzcategi, Dr. John Elliot Hergert, Dr. Jamie Kowalski, Dr. Archish Muralidharan, Seohyeon Jo, Rushi Kathiria, Dr. Nagaraj Chelliah Machavallavan, Raghav Mundra, Dr. Zeynep Cetinkaya. I also thank all my present and past roommates, Babatunde Adegoke, Dr. Clifton De Mesquita, Saish Sawant, Arvind Aradhya and Samantha Crocker. I appreciate my collaborators, Davis Conklin and Hailey Loehde-Woolard. I thank my partner Aniekan Inyang for her support. I thank everyone who stood beside me through this journey. Most importantly, I appreciate God for everything. I return all the glory to Him.

## TABLE OF CONTENTS

ABSTRACT.....	ii
DEDICATION.....	iv
ACKNOWLEDGEMENT .....	v
TABLE OF CONTENTS.....	vii
LIST OF TABLES.....	xi
LIST OF FIGURES .....	xii
CHAPTER ONE: INTRODUCTION AND OBJECTIVES.....	16
1.0.    INTRODUCTION .....	16
1.1.    Introduction to Sintering .....	16
1.1.1.    Sintering of Metals.....	16
1.1.2.    Sintering of Refractory Metals.....	17
1.2.    Introduction to Flash Sintering .....	20
1.3.    Major Drawbacks of Traditional Sintering Methods .....	22
2.0.    THESIS OBJECTIVES .....	23
Aim of this thesis .....	23
Objective 1: Flash Sintering Demonstrations in Metals .....	23
Objective 2: Comparative Analysis of Energy Consumption.....	24
CHAPTER TWO: REVIEW OF RELEVANT LITERATURE.....	25
3.0.    LITERATURE REVIEW .....	25
3.1.    Sintering Methods for Metals .....	25
3.2.    Sintering Theory .....	28
3.3.    Conventional Sintering of Tungsten .....	32
3.4.    Sintering Kinetics and Densification Mechanism in Metals.....	32
3.5.    Flash Sintering .....	33
3.5.1.    Joule Heating during Flash Sintering.....	36
3.5.2.    Defect Generation during Flash Sintering .....	37
CHAPTER THREE: MATERIALS AND METHODS .....	39
4.0.    EXPERIMENTAL METHODS.....	39
4.1.    Existing Approach: Flash Sintering Experiments in Ceramics.....	39
4.2.    Flash Sintering Experiments in Metals .....	40
4.2.1.    Powder and Sample Preparation .....	40

4.2.2.	Current Injection .....	41
4.2.3.	Measurement of Temperature .....	43
4.2.4.	Measurement of Shrinkage .....	43
4.2.5.	Electroluminescence .....	44
4.2.6.	Microstructural Examination .....	44
4.2.7.	Hardness.....	44
CHAPTER FOUR: FLASH SINTERING DEMONSTRATIONS .....		46
5.0.	Flash sintering of tungsten at room temperature (without a furnace) in < 1 min by injection of electrical currents at different rates .....	46
5.1.	Summary .....	46
5.2.	Introduction.....	47
5.3.	Methods.....	50
5.4.	Results.....	53
5.4.1.	Sintering.....	53
5.4.2.	Measurement of Resistivity .....	55
5.4.3.	Measurement of Temperature .....	56
5.4.4.	Calorimetry: Endothermic Enthalpy .....	58
5.4.5.	Molecular Dynamics Simulation .....	63
5.4.6.	Phenomenological Description of Flash in Metals .....	64
5.4.7.	Microstructure and Hardness .....	65
5.5.	Discussion .....	67
5.6.	Conclusion .....	69
6.0.	Flash Sintering of Rhenium at Ambient Temperature in < 1 Minute with Electrical Current	71
	71	
6.1.	Summary .....	71
6.2.	Introduction.....	72
6.3.	Methods.....	73
6.4.	Results.....	75
6.4.1.	Sintering.....	75
6.4.2.	Three Cycles .....	76
6.4.3.	Temperature and Luminescence .....	77
6.4.4.	Resistivity .....	78
6.4.5.	Energy Deficit Analysis.....	79

6.5.	Discussion .....	85
6.6.	Conclusion .....	87
7.0.	Current rate flash sintering of nickel at ambient temperature in < 1 minute .....	88
7.1.	Summary .....	88
7.2.	Introduction.....	89
7.3.	Methods.....	90
7.4.	Results.....	91
7.4.1.	Sintering .....	91
7.4.2.	Resistivity during flash .....	92
7.4.3.	Temperature and Electroluminescence .....	93
7.4.4.	Resistivity Comparison for Insitu flash, post flash and handbook reference. ....	95
7.4.5.	Energy Deficit.....	96
7.4.6.	Microstructure and Mechanical Behavior.....	99
7.5.	Discussion .....	100
7.6.	Conclusion .....	102
CHAPTER FIVE: COMPARISON OF ENERGY CONSUMPTION FOR FLASH SINTERING AND OTHER METHODS .....		103
8.0.	Comparative Analysis of Energy Consumption in Flash Sintering and other Metal Sintering Techniques .....	103
8.1.	Summary .....	103
8.2.	Introduction.....	104
8.3.	Methods.....	106
8.4.	Results.....	106
8.4.1.	Flash Sintering .....	107
8.4.2.	Other Sintering Methods.....	111
8.5.	Discussion .....	118
8.6.	Conclusion .....	119
CHAPTER SIX: EXPLORATORY STUDIES FOR FUTURE RESEARCH.....		120
9.0.	Exploratory Study1: Surface coating of Titanium Metal with Copper.....	121
9.1.	Summary .....	121
9.2.	Introduction.....	121
9.3.	Method .....	122
9.3.1.	Preparation of Titanium Specimens.....	122

9.3.2.	Flash Sintering .....	122
9.3.3.	Flash Deposition .....	123
9.3.4.	Microstructure Analysis.....	123
9.4.	Results and Discussion .....	124
9.4.1.	Resistance Analysis during Deposition .....	124
9.4.2.	Microstructural Analysis of Cu-coated-Ti Specimen .....	126
9.4.3.	Fracture Surface Morphological Analysis of Cu-coated-Ti.....	127
9.4.4.	Analysis of Coating Layer Thickness on Cu-coated-Ti.....	128
9.4.5.	Electrical Conductivity Enhancement of Cu-coated-Ti.....	130
9.5.	Conclusion .....	130
	Bibliography .....	132

## LIST OF TABLES

Table 1-1: Thermodynamic and Physical properties of Refractory Metals <sup>7</sup> .	18
Table 3-1: Mechanism of Sintering <sup>36</sup>	31
Table 5-1: W unaltered oxygen composition in %wt.	52
Table 5-2: Analysis of time, temperature, electrical power input for obtaining the energy deficit, and from that the mole fraction of Frenkel defects.	61
Table 5-3: A comparison of the hardness values for the current specimens and those processing in different ways from the literature <sup>88</sup> .	67
Table IV: Frenkel Defect Analysis Based on Energy Deficit	82
Table 7-1: The parameters used to estimate the energy deficit in Eq. (7-1).	97
Table 8-1: Summary of energy consumption at different rates for flash sintered nickel at various rates	108
Table 8-2: Selective laser melting of 316L stainless steel deposition parameters and energy density at a constant beam diameter of 55 $\mu\text{m}$ . Obtained from Bertoli et al. <sup>128</sup> . VED is Volumetric Energy Density.	117
Table 9-1: Summary of specimen thickness before and after coating. The points 1, 2 and 3 here in refers to the points highlighted in Figure 9-5.	129

## LIST OF FIGURES

Figure 3-1: (a) Illustration of sintering stages (b) Two-spheres sintering model showing the neck growth and fusion into one sphere that is 1.26 times the diameter of starting spheres <sup>34</sup> .	29
Figure 3-2: Basic illustration of sintering process causing densification and coarsening from green compact <sup>35</sup> .	30
Figure 3-3: Neck formation during sintering (a) without shrinkage and (b) with shrinkage <sup>35</sup>	31
Figure 3-4: Enhancement of 3YSZ sintering rate by the application of dc electrical field <sup>13</sup> .	34
Figure 3-5: Arrhenius plot of power density vs temperature for different materials at different combination of electric field and temperature <sup>45</sup> .	35
Figure 4-1: (a) Dog-bone design die (b) dog-bone specimen and typical sample dimension <sup>62</sup>	39
Figure 4-2: Flash experiments setup in metals (a) with furnace and (b) without a furnace	43
Figure 5-1: Current rate flash sintering. (a) The current-time profiles at current rates varying from 50 mA min <sup>-1</sup> up to 5000 mA min <sup>-1</sup> . (b) Shrinkage strain as a function of time at different current rates. (c) and (d) Shrinkage strain plotted against the instantaneous value of the current density, separated into two ranges: current rates < 600 mA min <sup>-1</sup> on the left, and >1000 mA min <sup>-1</sup> on the right. At the higher rates the collection is shifted slightly to the right because the onset of flash occurs at slightly over 20 mA min <sup>-1</sup> versus just below 20 mA min <sup>-1</sup> on the left.	49
Figure 5-2: Illustration of Flash Sintering setup for tungsten	51
Figure 5-3: (a) Linear shrinkage measured as a function of time while the current is increased at constant rates, ranging from 0.1 A s <sup>-1</sup> to 10 A s <sup>-1</sup> . (b) When the strain is plotted against the current density then the data for all current rates merge into a master curve, suggesting current density as the fundamental sintering parameter.	54
Figure 5-4: Sintering behavior at 0.1 A/s, repeated twice.	55
Figure 5-5: (a) Change in resistivity with current density during flash sintering of green tungsten compact, and two cycles of flash of dense tungsten compact with flash history. (b) Comparison of resistivity vs temperature during the two cycles of re-flash with the handbook reference values.	56
Figure 5-6: (a) Plot of Temperature vs Current Density for both furnace-ON and furnace-OFF experiments (b) Optical emission spectra for furnace-OFF experiment	57
Figure 5-7: (a) Plot of BBR and Convection losses as a function of temperature. (b) Energy deficit calculated as a difference between the input power and the power predicted from the BBR, Convection and specific heat. (c) Mol fraction of Frenkel pairs generated during flash sintering of tungsten without furnace	62
Figure 5-8: (a) Kinetic energy of phonons injected into an aluminum single crystal at first raises the temperature but then plateaus above the Debye Temperature, Thereafter, as shown in (b) the energy is consumed in the generation of Frenkel pairs. This behavior is similar to the data in Figure 5-4 where the temperature of the specimen does not increase as the current density is increases (up to 7.5 A mm <sup>-2</sup> ).	63

Figure 5-9: (a) The three regimes characterizing the phenomenological behavior in flash sintering of metals; the transitions are prescribed by three regimes: the incubation regime, followed by the flash regime, followed by the sintering to full density. The measurement of (b) temperature, (c) the estimate of defect generation, and (d) the resistivity, consistently show this three-regimes pattern. \_\_\_\_\_ 65

Figure 5-10: The microstructure of the sample before and after sintering. The grain size of the sintered sample was nearly the same as the size of the particles in the powder, approximately 12  $\mu\text{m}$ . \_\_\_\_\_ 66

Figure 6-1: Illustration of flash sintering of metals without a furnace \_\_\_\_\_ 74

Figure 6-2: This figure depicts the linear shrinkage as recorded by a CCD Camera across three current rates. The visual data from the video was processed and analyzed using Fiji software to determine the shrinkage. Linear shrinkage is plotted against current density and time, providing insight into the rate of compaction over the given durations and role of current density in the sintering process. \_\_\_\_\_ 76

Figure 6-3: The change in resistance with current density. The first cycle refers to the sintering of the powder pressed sample. Cycles 2 and 3 were repeated on this sintered specimen. Sintering lowers the resistance and gives reproducible results. Note the expanded resistivity scale on the right. \_\_\_\_\_ 76

Figure 6-4: The change in the specimen temperature with current density, (a) and with it the intensity of optical emission, (b). Figure (b) is shown with a wide range of intensity units at high current densities ( $22 - 30 \text{ A mm}^{-2}$ ), and then with a high resolution scale which shows the emission at low current densities ( $6 - 13 \text{ A mm}^{-2}$ ). \_\_\_\_\_ 77

Figure 6-5: Resistivity behavior during cycle 2 flash compared with literature resistivity of rhenium. \_\_\_\_\_ 78

Figure 6-6: A plot of BBR loss and Convective loss assuming  $h = 15 \text{ W m}^{-2}\text{K}^{-1}$  \_\_\_\_\_ 81

Figure 6-7: (a) Plots of the energy deficit, and (b) the corresponding concentration (in units of mol %) calculated from the endothermic enthalpy divided by the energy of formation of Frenkel pairs. \_\_\_\_\_ 84

Figure 6-8: (a) The three regimes depicting the phenomenological behavior in flash sintering of metals; the transitions are prescribed by three regimes: the incubation regime, followed by the flash regime, followed by the sintering to full density. The measurement of (b) temperature, (c) the estimate of defect generation, and (d) the resistivity, consistently show this three-regimes pattern. \_\_\_\_\_ 85

Figure 7-1: (a) As-pressed nickel specimen before flash sintering (b) Illustration of flash sintering setup for metals in an inert atmosphere of less than 100 ppm oxygen \_\_\_\_\_ 91

Figure 7-2: Linear shrinkage measured from the video captured using a CCD Camera. The insitu video captured at all rates were analyzed for shrinkage using Fiji software. \_\_\_\_\_ 92

Figure 7-3: Resistivity curve of nickel as a function of current density and time during the flash sintering of green specimen (black). The other two data sets were obtained by re-flashing the specimen after the first cycle. The first cycle data are for powder specimen (black) and the latter two for dense sample (red and green). \_\_\_\_\_ 93

Figure 7-4: (a) Measurement of the specimen temperature as a function of the current density. (b) The luminescence spectra at different current densities. The emission is ascribed to electroluminescence.	94
Figure 7-5: Resistivity behavior during flash, and with furnace heating of the flash sintered specimen. The temperature dependent resistivity data from literature are shown in green color.	95
Figure 7-6: A plot for the BBR loss and the convective loss assuming $h = 7 \text{ W m}^{-2} \text{ K}^{-1}$	98
Figure 7-7: (a) Plots of the energy deficit, and (b) the corresponding concentration (in units of mol %) calculated from the endothermic enthalpy divided by the energy of Formation of Frenkel pairs.	98
Figure 7-8: (a) Tensile stress-strain curve for the flash sintered nickel specimen (b) The SEM fractography showing dimples fracture surface morphology.	99
Figure 8-1: Power and Temperature relationship during laboratory scale furnace heating	105
Figure 8-2: (a) Resistivity as a function of current density during the flash sintering of nickel. Cycle 1 depicts a first repeat of the flash of an already flashed specimen while another repeat was depicted by cycle 2. (b) Power density as a function of time during the flash sintering of nickel.	108
Figure 8-3: (a) Curve of resistivity vs current density for flash sintering of green titanium compact (black) and flash of a dense titanium specimen with flash history (red). (b) Power vs time during the flash sintering of green titanium compact.	109
Figure 8-4: (a) Curve of resistivity vs current density for flash sintering of green tungsten compact (black) and flash of a dense tungsten specimen with flash history (red and blue). (b) Power vs time during the flash sintering of green tungsten compact.	110
Figure 8-5: : (a) Curve of resistivity vs current density for flash sintering of green rhenium compact (black) and flash of a dense rhenium specimen with flash history (red and blue). (b) Power density. vs time during the flash sintering of green rhenium compact	111
Figure 8-6: Comparison of power consumption and heating profile of microwave and conventional sintering of 92.5W-6.4Ni-1.1Fe alloy.	112
Figure 8-7: Power consumption for (10/28.7) and (15/30) dies as a function of time at 750 °C, 70 MPa and 50°C min <sup>-1</sup> heating rate.	114
Figure 9-1: a) illustration of the flash deposition setup. (b) CCD camera images of the specimen before and after deposition. The “before coating” image shows the 0.25mm thick and 100 mm long copper wire coiled around the dense titanium dogbone. The “after coating” image shows the copper coated titanium (c) Phone captured images of the titanium dogbone after pressing, after flash sintering, after the copper wire is coiled around it and after deposition.	124
Figure 9-2: (a) Voltage vs current during flash deposition (b) Resistance vs Current Density (c) Power vs Time during flash deposition of Cu-coated-Ti	125
Figure 9-3: (a) & (b) Micrograph of the cross section after flash deposition showing the layer of Cu on flash sintered Ti dogbone showing excellent bonding at the interface. (c) EDS line scan analysis shows 71.39 at% and 28.61 at% of Ti	127

Figure 9-4: SEM images of the fracture microstructure of the (a) dense titanium after flash sintering, and (b) copper coated titanium after flash deposition \_\_\_\_\_ 128

Figure 9-5: Phone capture image of copper coated titanium showing regions where copper layer thickness was measured. \_\_\_\_\_ 129

Figure 9-6: Voltage and Current relationship of the sintered titanium and Cu-coated-Ti after flash deposition. The measurement was done using a four-point probe measurement setup. \_\_\_\_\_ 130

## CHAPTER ONE: INTRODUCTION AND OBJECTIVES

### 1.0. INTRODUCTION

#### 1.1. Introduction to Sintering

Subjecting metals, glasses, or ionic crystals to temperature close to their melting points leads to fusion between the individual particles, thereby leading to improved density. This well-known process is referred to as “sintering”. Historically, some metals are fabricated from solid lumps because they could not be liquefied. Today, high melting point metals such as tungsten are produced by sintering, even though it can be a complex process. While it has become possible to melt most metals since the middle of the last century, interest in sintering waned for a while but has surged in the last few decades due to the cost effectiveness of sintering small components compared to casting and machining. Furthermore, unique products like porous bearings and expanded glass items - by incorporating gas-producing materials into the compacts - are easy to manufacture by sintering techniques. The history of sintering in the early days was provided by <sup>1,2</sup> while a more recent review is given by<sup>3</sup>.

Two major steps in sintering process include the elimination of pores and the fusion of particles to make a compact component <sup>4</sup>. Studies on the mechanism of sintering over the years have ascribed the driving force of both processes to the excess surface free energy. As sintering progresses, particles coalesce due to the excess free surface energy. An equilibrium system is reached because the total surface area is reduced because of the coalescence of particles<sup>5</sup>. Different categories of sintering include liquid-phase sintering, solid-phase sintering, and viscous sintering.

##### 1.1.1. Sintering of Metals

Powder metallurgy is a popular technology for metal components manufacturing. Unlike traditional metal processing approaches like casting, powder metallurgy process does not require

full melting of the metals thereby making it easy to manufacture high-temperature metals. Sintering is a major method of fabricating metal in powder metallurgy, which entails the production of solid metals from metal powders. Sintering of metallic powders are usually carried out on prepressed components at a temperature that is lower than the melting point of the constituents metal. Metal sintering is usually carried out in a controlled atmosphere or vacuum to avoid the reaction of the metal and oxygen at high temperature attained during sintering. Many studies have found it complex to completely eliminate porosity in the sintering of metallic powders, hence the development of hot pressing techniques that combines pressure and temperature to get rid of the pores and achieve higher densification of the compacts<sup>6</sup>. Common methods used in sintering metals include furnace sintering, mostly referred to as conventional sintering in this thesis, hot pressing, spark plasma sintering, electro discharge sintering and microwave sintering. A more elaborate description of these methods and some examples of them are given in section 3.1 of this thesis.

An interesting class of metals that requires even longer holding time, higher furnace temperature and relatively high energy consumption when employing traditional sintering and electric field assisted sintering approaches are the refractory metals. The present thesis demonstrates the possibility of consolidating two highly refractory metals, tungsten, and rhenium, to near-full density without a furnace, in less than a minute while consuming relatively low energy. The physical, thermophysical and chemical properties of refractory metals are introduced in the following section.

### **1.1.2. Sintering of Refractory Metals**

Refractory metals are naturally occurring transition metals whose melting points are above 2000°C. They have interesting applications in aerospace, nuclear, electronics, industrials, and

chemical industries. They have broadly varying availability and desired properties. The desirability of the properties of refractory metals especially in space and aerospace applications have made them a subject of intensive research and development over the years. In most of these applications, the desired properties of refractory metals sought after include their high melting point and strength above 1100°C or beyond<sup>7</sup>.

Refractory metals are all transition metals. Their position in the periodic table influences their crystal structures. Refractory metals in Group VA and VIA are body-centered cubic while Hafnium in Group IVA is hexagonal close packed at low temperature, but becomes body-centered cubic at 1300°C. In Group VIIA, rhenium is hexagonal closed packed. Likewise, osmium and ruthenium in Group VIIIA have hexagonal closed packed crystal structures. In Group VIIIB, iridium and rhodium are face-centered cubic. The refractory metals with body-centered cubic crystal structure have the strongest atomic-bond. In Table 1-1, some of the desirable thermodynamics and physical properties of refractory metals are captured.

Table 1-1: Thermodynamic and Physical properties of Refractory Metals<sup>7</sup>.

Metals	Melting Points, °C	Boiling Point, °C	Crystal Structure(s)	Density, g/cm³	Thermal Conductivity, cal/cm²/cm/C/sec	Electrical Resistivity, μΩ·cm at 20°C	Heat Capacity, cal/g at 20°C	Coefficient of Linear Expansion, 10⁻⁶/°C, near 20°C
Tungsten	3422	5930	BCC	19.3	0.48	5.5	0.032	4.5
Rhenium	3186	5630	HCP	21.0	0.17	19.3	0.033	6.7
Osmium	3033	5012	HCP	22.5	--	9.5	0.031	6.6
Tantalum	3017	5458	BCC	16.6	0.13	13.5	0.033	6.6
Molybdenum	2623	4639	BCC	10.28	0.35	5.21	0.061	5.4
Iridium	2446	4130	FCC	22.56	0.35	5.3	0.032	6.5
Niobium	2477	4744	BCC	8.57	0.125	14.8	0.065	7.1
Ruthenium	2334	4150	HCP	12.45	--	9.5	0.058	9.6
Hafnium	2233	4603	HCP<1310 BCC>1310	13.31	0.053	30	0.035	6.0
Rhodium	1964	3695	FCC	12.41	0.36	4.7	0.059	8.5

Vanadium	1910	3407	BCC	6.11	0.074	24.8	0.119	9.7
Chromium	1907	2671	BCC	7.15	0.16	12.8	0.107	6.2

BCC – Body-centered cubic, HCP – hexagonal closed packed and FCC – face-centered cubic

Refractory metals are processed by producing their powder through chemical precursors, blending the powders using various metallurgical methods and solid-state sintered using furnace sintering. More recently, field assisted sintering techniques have been reported as a means of consolidating refractory metals. Sintering refractory metals generally require high furnace temperature due to their high melting points, this can be altered by variables such as particle size, alloy, and impurities. Refractory metals have tendency to oxidize at high temperature thereby making oxygen restricted environment the ideal sintering environment. Tungsten, molybdenum, and rhenium have higher tendency to oxidize, inert atmosphere containing hydrogen and argon are typical for their sintering. Vacuum sintering is suitable for ruthenium and iridium since they have less tendency to oxidize. High vacuum sintering or inert atmosphere is often adopted for tantalum, niobium, and hafnium because they form hybrids in air sintering. Unlike other refractory meals, this trio - tantalum, niobium, and hafnium - is less tolerant of impurities <sup>8</sup>.

The first demonstration of flash sintering of metal presented herein is carried out on tungsten. Tungsten has many desirable properties and vast applications in different industries especially space <sup>9</sup>. Tungsten possesses the highest melting point and boiling points, 3422°C and 5930°C respectively, among all the refractory metals as seen in Table 1-1. This property alongside its high density, 19.3 g/cm<sup>3</sup>, high strength at high temperature and high thermal properties has made it an ideal material for space and fusion applications. Tungsten has a strong atomic bond owing to its BCC crystal structure <sup>10</sup>. Other attractive properties of tungsten include an elastic modulus of 407 GPa, a hardness of 9.75 GPa, a thermal conductivity of 175 W/(m.K) at room temperature, an

electrical conductivity of 17.9 MS/m at room temperature, and a low thermal expansion coefficient of  $4.5 \mu\text{m}/(\text{m.K})$  at room temperature<sup>11</sup>.

Further demonstration of flash sintering is reported on another highly refractory metal, rhenium. It is a naturally occurring element numbered 75 in the periodic table. It has a density of  $21.02 \text{ g/cm}^3$ , melting point of  $3180^\circ\text{C}$ , hardness of 7.0 on Mohs scale, specific heat capacity of  $0.14 \text{ J}/(\text{g}^\circ\text{C})$  at room temperature, electrical resistivity of  $18.40 \text{ n}\Omega\cdot\text{m}$  and thermal resistivity of  $48 \text{ W}/(\text{m}^\circ\text{C})$ . Rhenium has interesting properties like retaining its ductility at high temperature, this has also made it a desired candidate for alloying tungsten and molybdenum to increase their recrystallization temperature, reduce their brittle characteristics thereby improving their ductility and ultimate tensile strength<sup>12</sup>.

## 1.2. Introduction to Flash Sintering

Flash sintering was first reported in 2010 by Cologna et al.<sup>13</sup> at the Raj's lab of the University of Colorado Boulder when nanograins of zirconia (3YSZ) was sintered in less than 5 seconds at a furnace temperature of  $850^\circ\text{C}$ . In flash sintering, densification is achieved at a critical combination of electric field and temperature. The temperature required is reduced as the applied electric field increases. In flash sintering of ceramics and other nonmetallic materials, the onset of flash is signaled by an abrupt rise in conductivity. This is usually accompanied by electroluminescence with a single peak spectrum usually seen around 700 nm. The intensity of the spectra increases with increasing current density, but the position of the peak remains the same even with increasing temperature. This suggests that the blackbody radiation effects where the peak shift towards the blue region does not come into play in flash sintering<sup>14</sup>. Flash events normally follow an incubation period which depends on the magnitude of the applied field and furnace temperature.

Following the first demonstration of flash on 3YSZ, the flash sintering technique has been applied to different kinds of materials including ionic conductors, semiconductors, room temperature insulators, electronic conductors, among others<sup>15</sup>. Before the studies reported in this thesis, no conclusive report of flash sintering of pure metals has been published. In previous flash sintering studies, the ceramic powders are usually mixed with a binder, dispersant, or sintering aid, then cold pressed into a desired geometry. Most of the reports have used dogbone, cylindrical, and rectangular shapes. In some cases, the samples are pre-sintered after cold pressing to burn out the powder and enhance easy handling. To perform the flash sintering experiment, the sample is heated to the set furnace temperature, followed by the application of electric field.

Several studies have proposed different mechanisms of flash sintering based on experiments and theories. The three most reported mechanism include ultra-fast joule heating<sup>16</sup> and generation of Frenkel pairs. A narrow band of power density was observed for flash transition in all oxides materials that have been flashed which suggest the role of lattice vibration in the flash process. A previous study has indicated that flash events are accompanied by unusual vibration of the lattice structure, which could be explained by the creation of Frenkel defects through ab-initio simulations. Direct observations of significant atom movement during flash events also suggest that lattice vibrations play a role in defect generation<sup>17</sup>. A simulation was conducted using molecular dynamics to introduce phonons into a single crystal of aluminum under ideal conditions, with the expectation of a constant rise in crystal temperature as phonons spread. However, the simulation showed that the temperature stabilized at the Debye temperature, regardless of the starting temperature. The results reveal that at the vicinity of the Debye temperature, Frenkel pairs are generated in the form vacancy-interstitial pairs. The flattening of temperature is linked to the phonon energy being absorbed into the energy required to form Frenkel pairs<sup>18</sup>.

### 1.3. Major Drawbacks of Traditional Sintering Methods

Traditional sintering has been associated with numerous challenges. At the heart of these challenges is the reliance on excessive furnace temperatures, which not only stresses the furnace components but also escalates operational costs. Coupled with this is the long holding durations that these methods require, a factor that often limits production efficiency and scalability.

Equally disconcerting is the energy footprint of these conventional sintering techniques. Taking a snapshot of the status quo, it's startling to note that standard laboratory furnaces, pivotal for processes such as conventional sintering, spark plasma sintering, and hot pressing, expends between 5 to 10 kW of energy throughout the operational span of a single sintering experiment<sup>19</sup>. This consumption not only represents an economic overhead but also raises ecological concerns, casting a shadow over the sustainability of these practices.

Given these factors, it becomes imperative to continue to search for a solution for efficient and sustainable methods of manufacturing metals from powders. The path forward requires innovations to the process such that it is not just efficient but also environmentally friendly. This thesis offers an alternative metal sintering strategy, with the aim to revolve the challenge of energy conservation, process efficiency, and understanding the mechanism behind the suggested approach, forging a new era in metal sintering methodologies.

## 2.0. THESIS OBJECTIVES

The primary objective of this thesis is to introduce and examine flash sintering techniques as a potential solution to three of the major challenges limiting the conventional sintering of metallic components: (i) the need for furnace heating at high temperature, (ii) long holding times, and (iii) extensive energy consumption. This chapter outlines the objectives aimed to be achieved through the research and experimentation conducted.

### Aim of this thesis

- 1) To successfully implement flash sintering technique for metals, achieving sintering at room temperature and significantly reducing the processing time and energy associated with traditional methods.
- 2) To uncover the features of flash sintering in metals and understand the role of defects as a driving mechanism of the process.

### Objective 1: Flash Sintering Demonstrations in Metals

- 1) **Tungsten:** investigate the first conclusive application of flash sintering technique to metal, in this case, tungsten. The study emphasized the potential of extensive defect generation as the flash sintering mechanism. This is informed by the energy deficit observed between the input electrical energy and losses attributed to radiation, convection, and specific heating. Mechanical hardness of the sintered specimen will be investigated and compared to tungsten compact fabricated using different methods. Flash phenomena such as electroluminescence and shrinkage will be studied.
- 2) **Rhenium:** Apply and investigate the application of flash sintering technique to rhenium, another highly refractory metal. This study draws parallels from tungsten results. The study

also ensures consistency in the behaviors observed in the flash sintering of refractory metals.

- 3) **Nickel:** Extends the flash sintering approach to nickel, showing the generality of flash sintering in metals. Beyond just sintering and observing micrographs, this study examines the mechanical properties of the sintered nickel using ultimate testing machine. The fracture surface morphology will be analyzed.

## **Objective 2: Comparative Analysis of Energy Consumption**

Compare flash sintering and other alternatives including conventional sintering, microwave sintering, spark plasma sintering, selective laser melting, and electro discharge sintering. This dissection is mainly focused on energy consumption and efficiency of the sintering process.

## CHAPTER TWO: REVIEW OF RELEVANT LITERATURE

### 3.0. LITERATURE REVIEW

Sintering is a process of consolidating materials – such as ceramics and metals – from compacted powder using thermal energy with/without the application of external forces. Ceramics, metals, alloys, high-complex medical implants among others are fired and consolidated into useful shapes using this approach. The sintering process is a complex process owing to the combination of factors involved, including particle size, shape, degree of agglomeration, chemical composition, temperature, time, pressure, atmosphere, heating rate, and cooling rate. Thermodynamically, sintering is driven by reduction in surface energy. Rate of sintering can be increased by reducing particle size, since smaller particles have more surface energy. Also, higher temperature accelerates sintering because atomic motion increases with increasing temperature<sup>20</sup>. Sintering of refractory metals requires high temperature since sintering typically occurs within 75 to 90% of the material's melting point.

#### 3.1. Sintering Methods for Metals

Various sintering methods have been used to consolidate metals. Some of these methods include conventional sintering, microwave sintering, spark plasma sintering, hot isostatic pressing, electro-discharge sintering and laser sintering. Microwave sintering has been applied to different kinds of metals. Unlike conventional sintering where convection heating is followed by thermal energy transfer to the bulk of the specimen through thermal conductivity mechanism in a slow process, microwave sintering heating takes place through absorption of microwave field which is accompanied by volumetric heating of the specimen when thermal energy gets converted to electromagnetic energy. The absence of thermal conductivity mechanism makes it a faster and instantaneous process. Application of microwave sintering to metals achieved lower sintering

temperature and faster densification. Mondal et al. 2009<sup>21</sup> achieved 95% of the theoretical density of tungsten using microwave sintering. This was attained at a sintering temperature of 1775°C in 30 minutes and in a hydrogen atmosphere. Another study reported 1800°C sintering temperature and 20 kW power consumption in 6 – 7 hours to also achieve 93% final density using microwave sintering<sup>22</sup>. Molybdenum was sintered conventionally at a sintering temperature of >1750°C to achieve densities between 90 to 95% in 10 to 40 hours, further improvement of the process resulted in 98% final density in 10 hours at a sintering temperature of 1400°C. Changing the approach to microwave sintering, 99% final density at a furnace temperature of 1400°C was achieved in 30 minutes for the same molybdenum<sup>21</sup>. Rhenium was sintered using microwave sintering approach to 95% final density of rhenium at a sintering temperature of 2000°C for a 20 minutes soaking time<sup>21</sup>.

Metals have been sintered using pressure relief where a combination of temperature and pressure have been employed to achieve full densification of the metal powder. Material transport at atomic scale is attained by reaching high temperature while application of pressure helps intensify material transport. This type of sintering could be hot isostatic pressing (HIP) or hot uniaxial pressing (HUP). The former involves following sintering with hot isostatic press while the later involves uniaxial press being coupled to a furnace. The HIP method process subjects the components to high temperature, >1000°C, and pressure above 98 MPa to get rid of porosity and achieve consolidation of the components. For instance, tungsten was consolidated by a combination of spark plasma sintering – which was used in presintering the components to relative density about 90.4% – and accompanied by hot isostatic pressing. The HIP parameters included a temperature of 1650°C for a duration of 2 hours. The relative density obtained was in the range of 96.4% to 97.2%<sup>23</sup>. Another study by<sup>24</sup> applied HIP to sinter a tungsten alloy containing 93% tungsten, and

7% mixture of nickel and iron. In that study, the tungsten alloy was consolidated to 93.68% at 1400°C and 140 MPa. Another study investigated the application of hot pressing to sinter nickel<sup>25</sup>. HUP at a pressure of 300°C and 900 MPa pressure were used to achieve 7.15 g/cm<sup>3</sup> density of nickel while HIP technique achieved 7.51 g/cm<sup>3</sup> at a temperature of 900 °C and pressure of 150 MPa.

Selective laser sintering/melting method has been applied to many metals. This technique uses laser beam to achieve bonding of the specimen and can be done on several layers to manufacture parts. The result of the application of selective laser sintering/melting depends largely on the processing parameter. A well optimized selective laser melting process used to fabricate tungsten produced dense tungsten of > 98% final density and good mechanical properties with up to 460 HV<sub>0.05</sub> and an ultimate compressive strength up to 1 GPa<sup>26</sup>. Similar study but with different processing parameter yielded a 94.3% final density for pure W<sup>27</sup>. Dense molybdenum, and tantalum have been fabricated using the selective laser melting approach<sup>28,29</sup>.

Spark plasma sintering is a popular field assisted sintering technique because to its ability to achieve rapid densification through direct current injection through a setup containing punches, dies and the specimen. Tungsten has been sintered at temperature between 1200 to 2000°C under a pressure of 40 MPa. The study achieved densification without grain growth at temperature between 1200 to 1450°C while densification with grain growth was seen at temperature between 1500 to 2000°C<sup>30</sup>. A similar study achieved relative densities between 81 to 95% at temperatures ranging from 1600 to 1800 °C under pressures ranging from 60 to 120 MPa<sup>31</sup>. For nickel, high density of nickel was achieved using SPS under pressures of 50, 65 and 80 MPa under the application of temperatures 700, 850 and 1000°C. The consolidated specimen gave a yield strength ranging from 130 to 278 MPa and grain size of 5 to 45 μm.

Another interesting sintering technique that is fast, and energy efficient is the electro discharge sintering method. This method combines spark plasma sintering with capacitor discharge welding to consolidate a prepressed materials powder. The setup contains a die comprising a movable upper and static lower punches that serve as the electrodes that are connected to a capacitor bank. The capacitor bank can store energy through a step-down transformer, the energy is discharged to the pressed specimen, causing electric field to flow through it via the punches. The electrical energy is converted to Joule heating and leads to fusion of the particles together to achieve densification. For instance, pure tungsten, steel and an alloy of steel and tungsten have been densified using the electro-discharge sintering technique by using a capacitor bank that stores 80 kJ of electrical energy through a 19 mm diameter punches containing the specimen. The pressure used in that study is 388 MPa and the process was completed in milliseconds<sup>32</sup>. The major constraint of this technique is the limited process parameters which include the size of powder, pressure, and discharge energy.

### **3.2. Sintering Theory**

Conventional sintering has been classified into three stages including initial, intermediate, and final stages of sintering. The initial stage includes neck and grain boundary formation and surface smoothing. In this stage, the gradient in particle curvature determines the behavior of sintering. The intermediate stage entails the creation of isolated pores structures, grain growth, and densification. In the final stage, pore shrinkage and closure causes a reduced hindrance to grain growth are observed<sup>33</sup>. In Figure 3-1a, the sintering stages are illustrated. To model the sintering process with a two-sphere sintering model – the simplest model of sintering, two equally sized spheres are placed side by side making contacts and observed until it fuses into one another forming one larger sphere that is 1.26 times the diameter of the initial spheres - this is illustrated

in Figure 3-1b<sup>20</sup>. The model is based on the transport of matter from regions of high chemical potential to regions of lower chemical potentials. The former is along the convex surface of the particles and the grain boundary or the contact region while the latter is the concave surface of the particles.

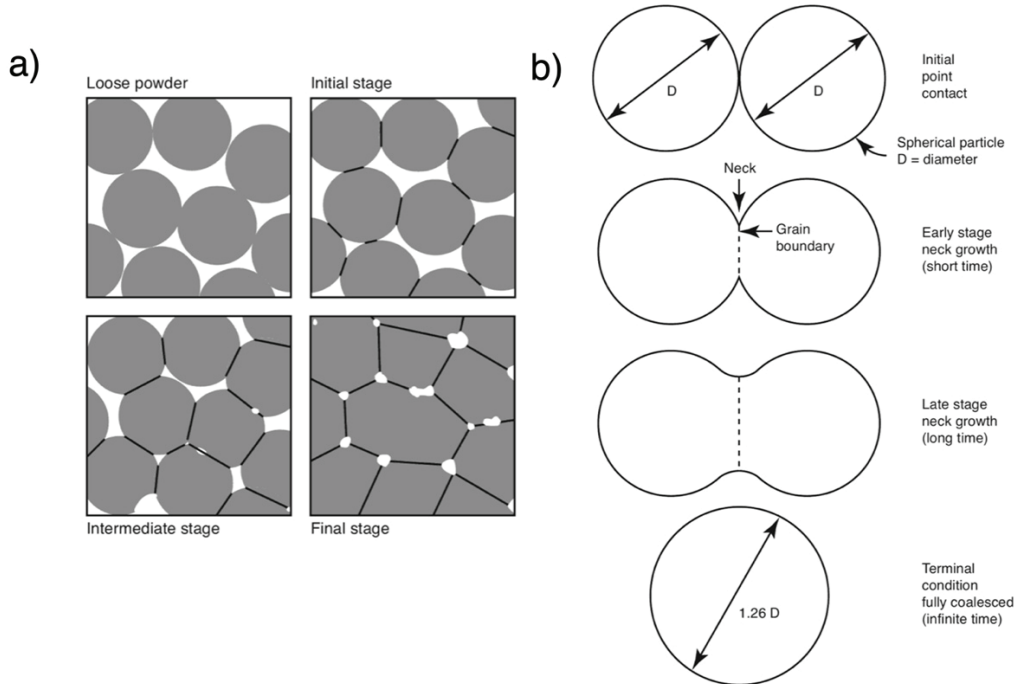


Figure 3-1: (a) Illustration of sintering stages (b) Two-spheres sintering model showing the neck growth and fusion into one sphere that is 1.26 times the diameter of starting spheres<sup>34</sup>.

The thermodynamic cause of sintering is the reduction in total interfacial energy. Using an ideal crystal as a starting point, each atom occupies repetitive sites in the crystals and are bonded together as represented by the lines. Materials with higher melting points like metals have stronger bonding, thereby have higher surface energy that must be reduced before sintering takes place<sup>34</sup>. The total interfacial energy of a material is expressed as  $\gamma * A$ , where  $A$  is the total interface (surface) area and  $\gamma$  is the surface/interface energy. The following equation is obtained when the interfacial energy expression is differentiated as follow:

$$\Delta(\gamma A) = \Delta\gamma \cdot A + \gamma \cdot \Delta A$$

The left component of the right-hand side,  $\Delta\gamma \cdot A$ , is the surface energy reduction occurring when particle-pore interface is reduced by particle-particle (grain boundaries) interface, which results in densification. In the right component,  $\gamma \cdot \Delta A$ , interfacial area removal by grain coarsening is depicted, the volume of the material remains the same as the size of the pores grows. In Figure 3-2, the schematics of the two processes described are presented.

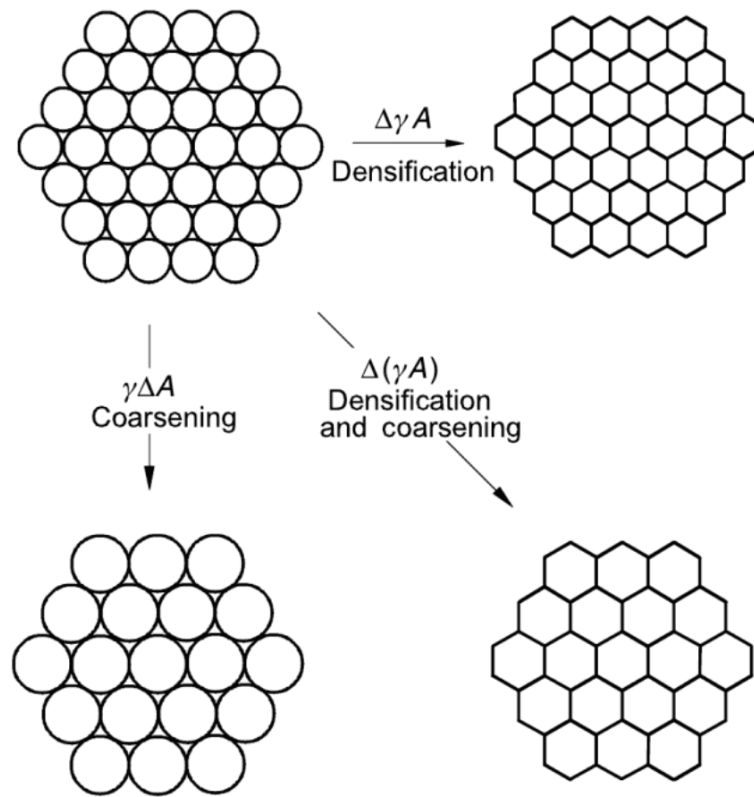


Figure 3-2: Basic illustration of sintering process causing densification and coarsening from green compact<sup>35</sup>.

Additionally, from a thermodynamic viewpoint, contact of two particles can be accompanied by material transfer and this could be of two different types. Type one, mass transfer from the surface to the neck between the two particles. The other type of mass transfer that could occur involves the transfer of material from the grains or the bulk of the material to the neck. The former will not cause reduction in distance between the particle center while the latter will cause a decrease in

distance between the particle center. The formation of the neck as a result of these two types of mass transfer is shown in Figure 3-3.

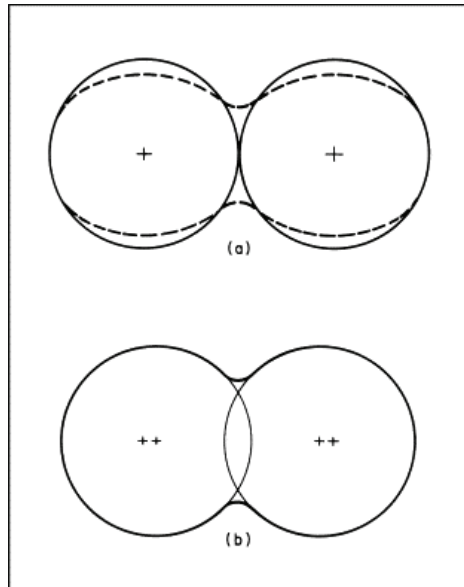


Figure 3-3: Neck formation during sintering (a) without shrinkage and (b) with shrinkage <sup>35</sup>

Mechanisms that cause particle necking and joining during sintering include surface diffusion, volume diffusion, vapor transport, grain boundary diffusion, plastic flow, and lattice diffusion. In Table 3-1, the source and sink of the mentioned mechanisms are listed.

Table 3-1: Mechanism of Sintering <sup>36</sup>

Mechanism	Source	Sink
Lattice diffusion	Surface	Neck
Surface diffusion	Surface	Neck
Grain boundary diffusion	Grain Boundary	Neck
Volume diffusion	Grain Boundary	Neck
Vapor Transport	Surface	Neck
Plastic Flow (dislocation mechanism)	Bulk	Neck

### 3.3. Conventional Sintering of Tungsten

Conventionally, tungsten has been sintered at temperature above 1650°C<sup>37</sup>, enhancement of the sintering process has been achieved by adding additives such as group VIII transition elements. For instance, addition of palladium or nickel can bring down the sintering temperature of tungsten from 2500°C to 1400°C<sup>38</sup>. Enhancement of densification by the addition of transition elements have been attributed to mass transport kinetics and enhanced solubility where these elements acts as a short circuit diffusion pathway<sup>39</sup>. Another approach that has been used to reduce sintering temperature in tungsten is particle size reduction. The following studies<sup>8,11,40,41</sup> reported reduction in sintering temperature of tungsten by reducing the particle size to submicron or nano-size level. Other conventional sintering methods have been used to obtain a sintering temperature lower than conventional sintering temperature in tungsten. Bose et al.<sup>40</sup> reported reduction in sintering temperature of nano-sized tungsten from 2500°C to 1700°C with the application of pressure assisted sintering method where plasma pressure was used to compact the tungsten powder. Using spark plasma sintering, Oda et al.<sup>42</sup> reported a sintering temperature of 1000°C for a 450 nm sized tungsten powder. Microwave sintering method achieved a sintering temperature of 1800°C<sup>22</sup>.

### 3.4. Sintering Kinetics and Densification Mechanism in Metals

Sintering kinetics of metallic powders have been attributed to bonding between compacted particles when mass transport occurs at temperature below their respective melting points. Densification and grain growth are the two major processes that happens during sintering processes.

Early studies on tungsten reported an estimated activation energy of 143 kcal/mole for volume diffusion or lattice self-diffusion<sup>43</sup>. In a separate examination involving calculation of the activation energies at varying time as the shape of tungsten changes during sintering, an activation

energy of  $106 \pm 8$  kcal/mole was reported. The change in shape with time was attributed to surface diffusion<sup>43</sup>. Kothari<sup>43</sup> sintered pressed compacts of  $3\mu\text{m}$  size tungsten at times ranging from 30 to 500 minutes, and at temperature ranging from 1100 to 1500°C. Relative densities between 63 and 75% of the theoretical densities were obtained and activation energy of  $102 \pm 2$  kcal/mole was calculated. Activation energies lower than volume diffusion obtained from the sintering of tungsten by<sup>43</sup> led to a conclusion that the diffusion mechanism of the sintering of tungsten may be attributed to other diffusion mechanisms, suggesting grain boundary diffusion instead of volume diffusion. In another study, which seems to agree with the findings of<sup>43</sup>, experiments were carried out at a temperature ranging between 1300-1750°C using tungsten particle sizes ranging from 0.45 to  $0.88\mu\text{m}$ . An activation energy of 110.7 kcal/mole was calculated. This study, which reported 75 to 92% relative density, also attributed the lower activation energy but larger diffusion coefficient to grain boundary diffusion densification mechanism<sup>44</sup>.

### **3.5. Flash Sintering**

Flash sintering first came to light in Raj's laboratory through the work of Cologna et al.<sup>13</sup>, who first sintered nanograin zirconia to complete density in under 5 seconds at a temperature of 850°C. They used 3YSZ powder with a particle size of 60 nm, shaping it into a dog-bone form and heating it within a tubular furnace. As shown in Figure 3 4, the full density of 3YSZ was attained at a specific critical mix of temperature and electric field.

Flash sintering was first reported in the Raj's lab by Cologna et al.<sup>13</sup> when nanograin zirconia was sintered to full density in less than 5s at 850°C. The 3YSZ powder of particle size 60 nm was uniaxially pressed to a dog-bone shape and heated in a tubular furnace. As presented in Figure 3-4, full density of 3YSZ was achieved at a critical combination of temperature and electric field.

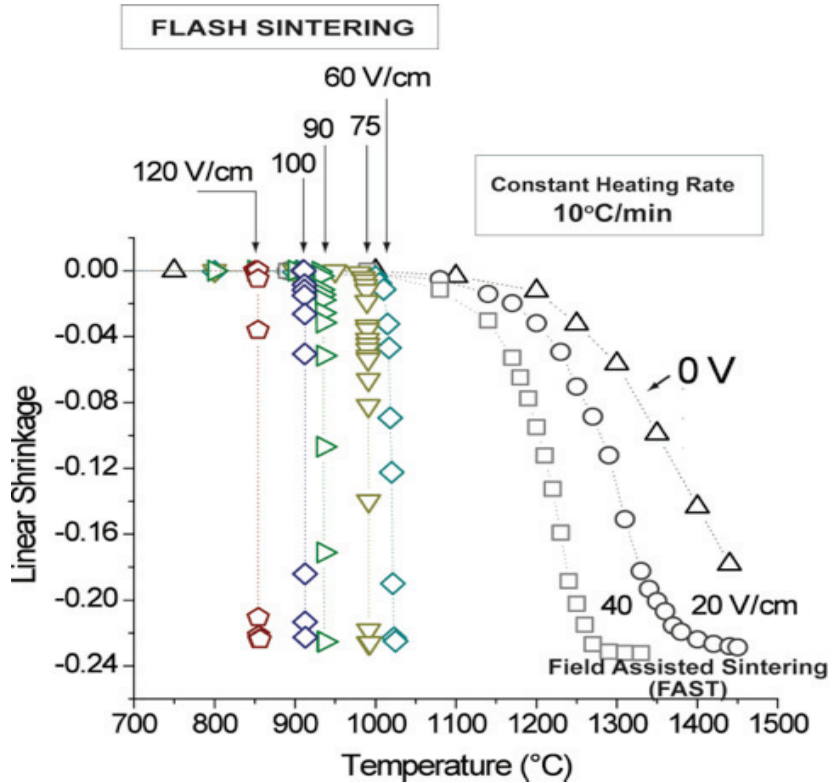


Figure 3-4: Enhancement of 3YSZ sintering rate by the application of dc electrical field<sup>13</sup>.

By applying lower field, <40 V/cm, gradual densification was recorded at temperature higher than 1200°C. Increasing the electric field to 60 V/cm shifted the flash onset to lower temperature, ~1000°C, and facilitated an almost instantaneous sintering. Intriguingly, instantaneous sintering was achieved by applying 120 V/cm and moving the temperature to 850°C. This phenomenon is termed “Flash Sintering”, heralding the beginning of the flash sintering era in materials processing and sintering technology. The onset of flash was signaled by an abrupt increase in conductivity and unusual electroluminescence which has a peak at ~700 nm. The intensity of the electroluminescence usually increases with increasing current density, which also means increasing temperature. The peak of the emission spectrum remains the same regardless of the temperature or current density attained. These two phenomena, rise in conductivity and electroluminescence, have been the two signature events of flash sintering.

Flash sintering has been applied to most oxides, if not all<sup>45</sup>. Flash sintering have been demonstrated on semiconductors like  $\text{CoMnO}_4$ <sup>46</sup> and ionic conductors like yttria stabilized zirconia<sup>47</sup>, electronic conductors like titania<sup>48</sup>, wide band-gap insulators like MgO-doped alumina<sup>49</sup> and undoped yttria<sup>50</sup>, silicon carbide and complex oxides like  $\text{BaTiO}_3$ <sup>51</sup>. A common behavior observed in the flash sintering of these different oxides is that flash is signaled by nonlinear rise in power density at the onset of flash. This is made obvious by creating an Arrhenius plot of power dissipation as a function of temperature, as given in Figure 3-5. An interesting finding from this plot is that transition to flash occur under a narrow band of power density, within 10 to 50 mW mm<sup>-3</sup>, for all materials even though these studies were performed at different combinations of temperature and electric field.

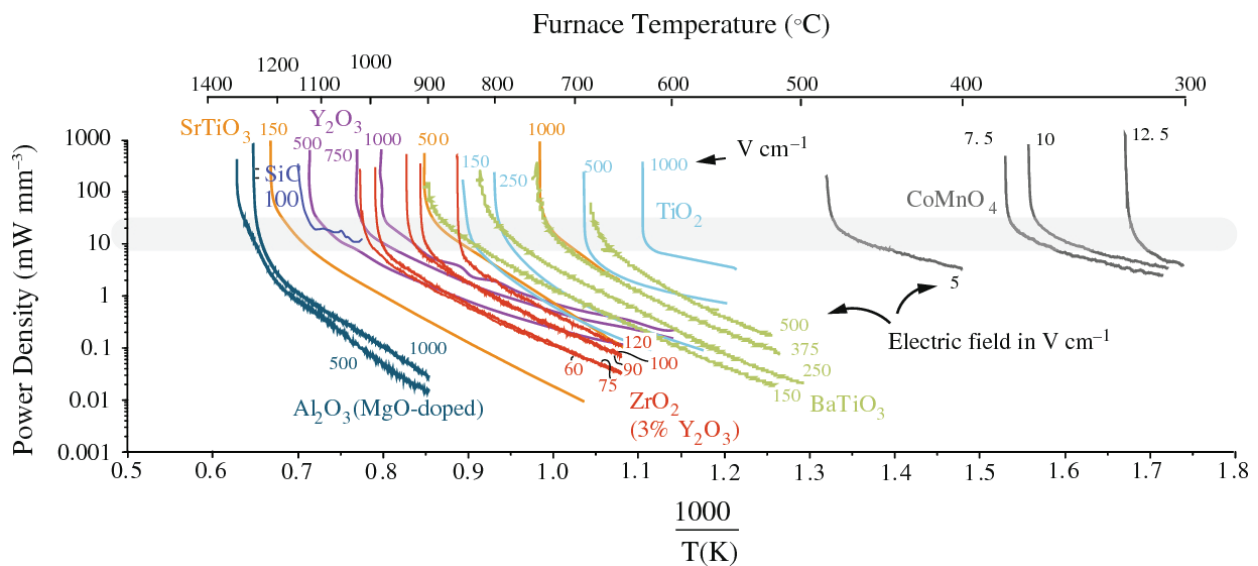


Figure 3-5: Arrhenius plot of power density vs temperature for different materials at different combination of electric field and temperature<sup>45</sup>.

In more recent studies, reports of application of flash have been made for single phase of multicomponent ceramic, high entropy oxide of five separate oxides<sup>52</sup>, and alumina-doped lithium lanthanum zirconate<sup>53</sup>. This application, termed reactive flash sintering have significantly reduced

the long hours required of these materials in conventional sintering to few seconds in flash sintering.

Early applications of flash sintering were carried out by applying electric field, and switching to current control when flash is initiated. A study by Kumar et al.<sup>54</sup> reports the possibility of controlling the experiment by injecting current at a constant rate into the specimen from the beginning. Like the previous approach, the two signature events in flash were observed including abrupt rise in conductivity at flash onset and electroluminescence.

### **3.5.1. Joule Heating during Flash Sintering**

The specimen heats up during flash sintering because of Joule heating. There have been questions on the role of Joule heating in the ultra-fast rate of sintering in flash. Chen and Park<sup>55</sup> measured electrical conductivity using in-situ impedance spectroscopy in comparison to the extrapolated conductivity of 3YSZ in the flash regime. They estimated 2100°C to 2500°C as the specimen temperature of 3YSZ. The estimation was based on assumptions like (i) transport number remains the same during flash and (ii) no change in activation energy of conduction. Another study by Narayan asserted that there is preferential heating at the grain-boundary followed by melting, which facilitate the densification of the powder<sup>56</sup>. However, this claim was proven wrong by Holland et al by showing that thermal diffusivity is so high that such temperature gradient is not possible across a 100 nm grain<sup>57</sup>. The different views on the mechanism of flash sintering necessitated the need to accurately measure the specimen temperature. Ways to show the heat dissipation during the process include convection, conduction and radiation. However, with high temperature been reached during the experiment, the effect of conduction and convection can be neglected. The specimen temperature was determined using the simple black body equation given as:

$$\frac{\delta T}{T} = \frac{\delta W}{4A\sigma T^4} \quad (3-1)$$

where  $T$  is the ambient temperature,  $\delta T$  is the change in temperature of the specimen due to electrical energy heat dissipation,  $A$  is the surface area for radiation and  $\sigma$  is the Stefan-Boltzmann constant. Integrating the temperature from furnace temperature to specimen temperature, and integrating electrical power from 0 gives the following equation:

$$\frac{T_s}{T_0} = \left[ 1 + \frac{1000.W_v}{\varepsilon_m \sigma T_0^4} \left( \frac{V}{A} \right) \right]^{\frac{1}{4}} \quad (3-2)$$

where  $T_s$  is the specimen temperature, and  $T_0$  is the furnace/environmental temperature.  $\frac{V}{A}$  is the volume divided by the surface area and  $\varepsilon_m$  is the emissivity of the specimen. The modification of the equation (3-2) for current rate approach is given by Kumar et al<sup>54</sup>. For a typical 150 mWmm<sup>-3</sup> power density flash for zirconia, temperature between 1100 – 1150°C have been calculated. These values agree with temperature measured using optical pyrometer. The correctness of this method of measuring the specimen temperature have been validated in different studies.

### 3.5.2. Defect Generation during Flash Sintering

The mechanism of flash sintering has been ascribed to the combined effects of joule heating<sup>58</sup> and huge defects generation that leads to mass transport acceleration<sup>59</sup>. The universality of narrow band of power density for transition to flash in oxides materials (in Figure 3-5) suggests the pivotal role of lattice vibrations in the flash process. The size of this flash power transition matched the energy of phonons. The question is, how can lattice vibrations lead to crystal defects like Frenkel pairs when the phonon's energy is a thousand times less than the energy required to form these defects? It was suggested this can only happen if the lattice vibrations are not the simple harmonic motion, but rather more complex and nonlinear, different from traditional physics concepts. These complex

vibrations in the phonons' local strain fields can only occur if their wavelengths are short, about the size of the lattice unit or smaller. This led to the postulation that the Debye temperature could be the starting point for these power transition. Experiments performed to validate this proved that temperature can approach the Debye temperature as a lower bound<sup>60</sup>. Previous study has shown that flash is followed by unusual lattice expansion which was explained by ab initio simulation<sup>61</sup>. A subsequent study measuring the displacement of large atoms during in-operandi flash experiment using X-ray scattering shows lattice vibrations as possible genesis of defect formation<sup>17</sup>. Using molecular dynamics simulation approach to validate this postulation, Jongmanns et al<sup>18</sup>. injected phonons into a single crystal of aluminium under adiabatic conditions. Starting the simulation below the Debye temperature and keeping the wavelength of the phonons under the lattice parameter and at the edge of the Brillouin zone, it was found that the specimen heats up and stabilizes when it reaches the Debye temperature. If the initial temperature is higher than the Debye Temperature, it drops to the Debye temperature. Findings show that the phonon injection around the Debye temperature causes Frenkel pairs generation, which is why the temperature flattens as the phonon energies are absorbed into the enthalpy of formation of Frenkel pairs.

## CHAPTER THREE: MATERIALS AND METHODS

### 4.0. EXPERIMENTAL METHODS

#### 4.1. Existing Approach: Flash Sintering Experiments in Ceramics

Powders of the ceramic to be sintered are uniaxially pressed into a desired shape – usually dog-bone – at high pressure. Figure 4-1 shows a typical dog-bone die and the resulting dog-bone shaped specimen.

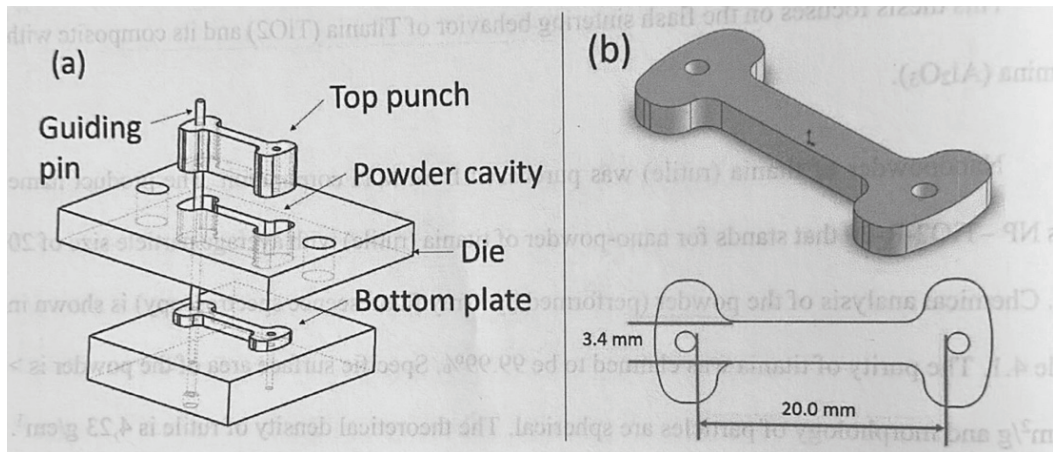


Figure 4-1: (a) Dog-bone design die (b) dog-bone specimen and typical sample dimension<sup>62</sup>

Specimens, hanged to two electrodes connected to a power source through the dog-bone holes, are heated to a specific furnace temperature in a furnace. The first flash experiment entails the application of electric field to the dog-bone specimens already heated to a certain temperature, and switching to current control at flash onset which is signaled by an abrupt rise in conductivity. Another approach reported by <sup>63</sup> rather control the current from the beginning of the experiment by injecting current, and increasing it a constant rate. In both cases, the power source is controlled using a computer program, written in MATLAB (and Python in some experiments) in Raj lab but can be written in various visual and non-visual programming languages. Data containing time, current, and voltage are returned from the program. Electric field is calculated by dividing the voltage by the length of the specimen, current density is calculated by dividing the current by the

area (width \* thickness) of the specimen. Power density is calculated by multiplying the electric field by the current density.

Temperature is measured in the specimen using an optical pyrometer which light is focused on the specimen and an emissivity value is set to obtain accurate temperature data. The temperature data is outputted in the program used to control the power source in order to obtain a synced data with the time and other parameters being measured.

Electroluminescence is captured using an optical spectrometer which is horizontally or vertically focused on the specimen to record the intensity of emission from the specimen during flash and at various wavelength which depends on the specification of the spectrometer.

To observe the microstructure, sintered specimens are cut, polished to  $1\text{-}3\mu\text{m}$  surface roughness, and etched at a selected temperature for a desired period. The microstructure is observed under a scanning electron microscope. Grain size can be measured from the micrograph by using the line intercept method.

## **4.2. Flash Sintering Experiments in Metals**

Flash sintering setup is similar in ceramics and metals. The major difference is that flash experiments can be performed with or without the furnace in metals, much higher current source is also required for flash experiments in metals, and most metals require an inert atmosphere or vacuum atmosphere to prevent oxidation. All experiments in this thesis followed the constant current rate approach reported in Kumar et al<sup>63</sup>.

### **4.2.1. Powder and Sample Preparation**

First set of experiments were performed using tungsten powder of 99.99% purity with a particle size of  $12\mu\text{m}$  purchased from Alfa Aesar. 5 wt% PVB binder was mixed with tungsten powder

before pressing to a dog-bone shape at 55 to 70 MPa to attain a green density of 72%. However, the specimens with the binder could only be sintered to a density of only ~92%. Significantly higher densities were obtained without the binder; therefore, the use of the binder was discontinued.

In subsequent experiments – reported herein – for all metals, the metal powders were pressed to higher pressure (172 – 200 MPa) and attaining higher green density. This significantly increased the final density, in the case of tungsten, to ~97 – 98% relative density. These binder-free specimens were prepared with less than 1g of the metals powder that was placed in mold and pressed to a dog-bone shape using a Carver Hydraulic laboratory press. There are two types of dies employed in this study, first type produces an average gage length of 1.6 cm, while the second type produces a dogbone with average gage length of 2.0 cm. Width of dogbone made from both types of dies has an average width of 3.5 mm and the thickness depends on factor such as maximum pressure attained and quantity of powder. Note that the length reported for voltage and emissivity measurements differs because it is the length between the voltage probes in a four-points measurement method. The green density of the dogbone shaped specimens was obtained using Archimedes density measurement method. The dogbone has two 1.1mm diameter holes in the ears for the purpose of connection to the anode and cathode of the power source.

#### **4.2.2. Current Injection**

Oxidation of metals at high temperature was avoided by carrying out the experiment within a glove box. The glove box was the Genesis model, manufactured by Vacuum Atmosphere Company, USA). Argon gas (99.9% purity) was procured from Airgas, USA. The oxygen level in the Glovebox was kept below 100 ppm.

Two tungsten electrodes (Weldmonger, USA) of 1mm diameter each were inserted into the two 1.1mm dog-bone ears and connected to the anode and cathode of a KEPCO KLN30-100 Power Supply with a 30 V and 100 A voltage and current output capacity respectively.

In experiments performed in the furnace, the setup was inserted into a furnace and ramped up to 800 °C (in the case of tungsten) before flash sintering. In experiments performed without a furnace, current was directly injected into the specimen at room temperature in the glovebox. The setup with and without the furnace is shown in Figure 4-2. A software written in Raj's lab was used to control the current injection and read the voltage between the specimen from data measured by a Keithley 2000 digital multimeter (USA). Current was injected into the specimen at a constant rate by sending the desired output current through the data acquisition software to an output channel of a National Instrument Data Acquisition (NI DAQ) device which is connected to the power supply. The current values sent through the NI DAQ to control the power source current output were recorded as a function of time. The voltage measured across the specimen using the Keithley multimeter was also recorded in real time. The specific resistance was calculated and recorded as a function of time. Other parameters including electric field, current density, power density and so on were calculated in Microsoft excel.

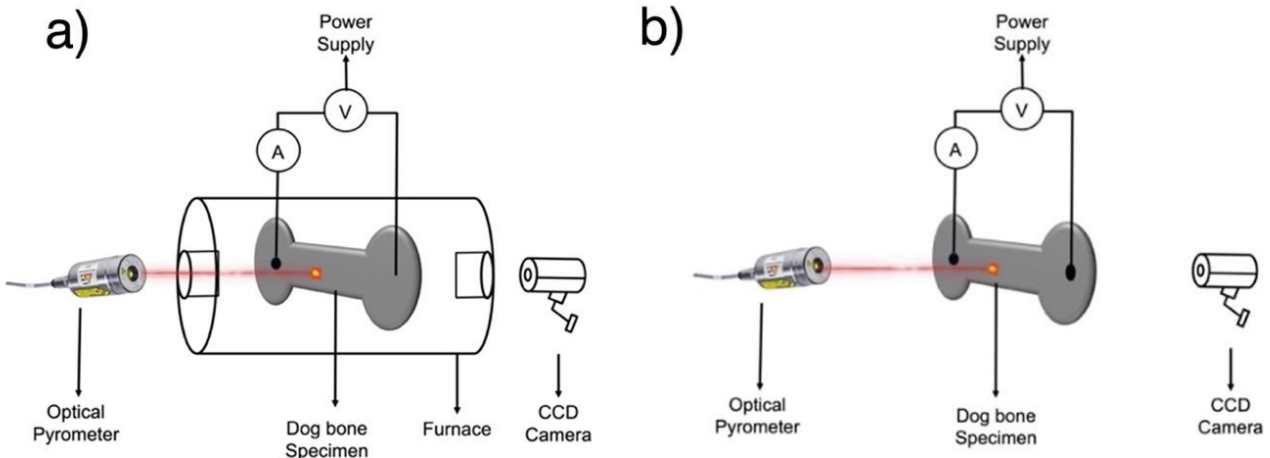


Figure 4-2: Flash experiments setup in metals (a) with furnace and (b) without a furnace

#### 4.2.3. Measurement of Temperature

Micro Epsilon (CTLM-1HCF4-C3 and CT-SF22-C8) pyrometers was employed to acquire the specimen temperature in real time. Temperature data was feed through an input channel of the NI DAQ and recorded as a function time using the data acquisition software. The emissivity value of the pyrometer was set to the surface emissivity of the metal been investigated. In the case of tungsten, the method used to determine the emissivity and error range is described in the following section. The lower limit of the pyrometer is 650°C.

#### 4.2.4. Measurement of Shrinkage

Sintering shrinkage was measured with a CCD camera manufactured by Imaging Source (Germany). It was placed in focus at the front of the set-up on the dog-bone. Fiji, an ImageJ software, was used to obtain the shrinkage data from the frames obtained from the CCD video. Linear shrinkage is calculated as true strain,  $\varepsilon$  using:

$$\varepsilon = \ln \left[ \frac{L}{L_o} \right]$$

4-1

where  $L$  is the length measured as a function of time during sintering,  $L_0$  is the initial length of the sample. The volumetric shrinkage is equal to  $3\varepsilon$ .

#### **4.2.5. Electroluminescence**

Electroluminescence is a constant feature of flash experiments in ceramics. We wished to see if metals also luminesce in the same way. Therefore, optical emission was measured using a spectrometer (USB4000-UV-VIS) manufactured by Ocean Optics (USA). The spectrometer was focused on the specimen during the flash with a collimating lens connected to an optical fiber. Data was collected and plotted Ocean Optics and Origin software respectively.

#### **4.2.6. Microstructural Examination**

The microstructures of the sintered metal specimens were obtained from cut and polished cross sections. The specimens were mounted using Allied QuickCure powder and liquid, then cured at room temperature for 5 minutes. The mounted specimens were polished using a LECO VP-160 polishing machine using polishing papers ranging from  $240\text{ }\mu\text{m}$  to  $1\mu\text{m}$ . The specimens were then rinsed, dried, and etched. The etched specimens were immediately rinsed in water.

A Hitachi SU3500 Scanning electron microscope with point and click real time 3D image observation capability owned by Colorado Shared Instrumentation in Nanofabrication and Characterization (COSINC) was used to observe the microstructure of the specimens. The equipment was set to back scattered electrons imaging mode at 10 to 15 kV.

#### **4.2.7. Hardness**

Vickers Hardness was measured using the standard ISO 6507-12018 via the Rockwell Hardness tester situated in Idea Forge, University of Colorado Boulder. Load between 15 and 150 Kgf was applied to the polished surface of the metal using a diamond indented. The hardness value was obtained using:

$$H_v = \frac{2F \sin \frac{136^\circ}{2}}{d^2} = 1.854 \frac{F}{d^2} \quad 4-2$$

where  $d$  is the average diagonal length of the indentation in mm and  $F$  is the load applied in kgf. Ten different measurements were made on each specimen and the average  $H_v$  is reported. The image of the indentation was captured using optical microscope and the diagonal was measured using Fiji software.

## CHAPTER FOUR: FLASH SINTERING DEMONSTRATIONS

### **5.0. Flash sintering of tungsten at room temperature (without a furnace) in < 1 min by injection of electrical currents at different rates<sup>1</sup>**

#### **5.1. Summary**

Sintering of tungsten nominally requires several hours at ultrahigh temperatures. We show this refractory metal can be sintered quickly by direct injection of current into dogbone shaped specimens. The current rate was varied from 10 A/s (fast) to 0.1 A/s (slow), leading to sintering in 2 s to 200 s, respectively. Sintering occurred at the same current density, regardless of the current rate. In all instances the samples sintered when they reached 1000°C. The phenomenological behavior of flash sintering of metals is described by three stages: an incubation time followed by electroluminescence, and finally by abrupt sintering to full density. It is conjectured that rapid sintering is instigated by the formation of Frenkel pairs (vacancies and interstitials), as well as electrons and holes. The point defects accelerate mass transport while electrons and holes recombine to form photons. Calorimetric measurements show an endothermic reaction attributed to the creation of defects. Estimates suggest an unusually large concentration of Frenkel pairs. PS: flash sintering is different than electro-discharge-sintering where a capacitor is discharged in a few milliseconds to sinter a metal. Here, instead of dumping large amount of energy at once, a power supply is programmed to control the rate of current injection.

---

<sup>1</sup> This manuscript has been published in Journal of American Ceramic Society and is currently under review as manuscript number JACERS-51489.R1. This work has inputs from Dr. Syed Idrees Jalali, Prof Alan Weimer and was directed by Prof Rishi Raj.

## 5.2. Introduction

The interest in field assisted sintering of materials started several decades ago with microwave sintering<sup>64</sup>. A major boost was the advent of Spark Plasma Sintering<sup>65</sup>. SPS has evolved as an enabling technology for densifying metals and ceramics that are difficult to consolidate by normal sintering<sup>66</sup>. This field received a further boost in the discovery of flash sintering (FS) where dogbone samples could be sintered without graphite dies in open air, within a conventional furnace, by applying field and current directly to the specimen<sup>67</sup>.

Flash sintering has been shown to apply widely<sup>68</sup>; to nearly all oxides as well as non-oxide ceramics<sup>69</sup>. The history of flash has been published recently<sup>68</sup>; it gives an overview of the developments since 2010. A recent review by Yu et al.<sup>70</sup> is also insightful. Two other advanced processing methods, ultrafast heating rate<sup>71</sup>, and cold sintering<sup>72</sup>, have emerged. Interestingly the equivalence between ultrafast heating rate experiments and flash sintering was recently demonstrated in experiments with thin layers made from fine powders<sup>73</sup>.

The in-operando, open access to the specimens allowed continuous measurement of the sintering strain with a rapid-rate camera<sup>67</sup>, the temperature with a pyrometer<sup>74</sup> and the optical emission spectrum with a spectrometer<sup>75</sup>. The simplicity of the experiment allowed gathering of fundamental data which helped to initiate a fundamental understanding of this unusual phenomenon. For example, the temperature of the specimen was measured with a platinum standard at Synchrotrons (Argonne and Brookhaven)<sup>74</sup>. The synchrotron experiments gave two additional results: (i) the unexpected evolution of far from equilibrium phases which grew and then faded when the flash was turned on and off<sup>76</sup>, and (ii) unusual expansion in the lattice parameter, which when coupled with first principles calculations was consistent with the formation of Frenkel pairs of vacancies and interstitials<sup>77</sup>. Very recently an ultrahigh conductivity solid state electrolyte for lithium-ion batteries of non-stoichiometric

compositions, was made by flash<sup>78</sup>; it points to the potential of flash in the discovery of unusual far-from-equilibrium materials.

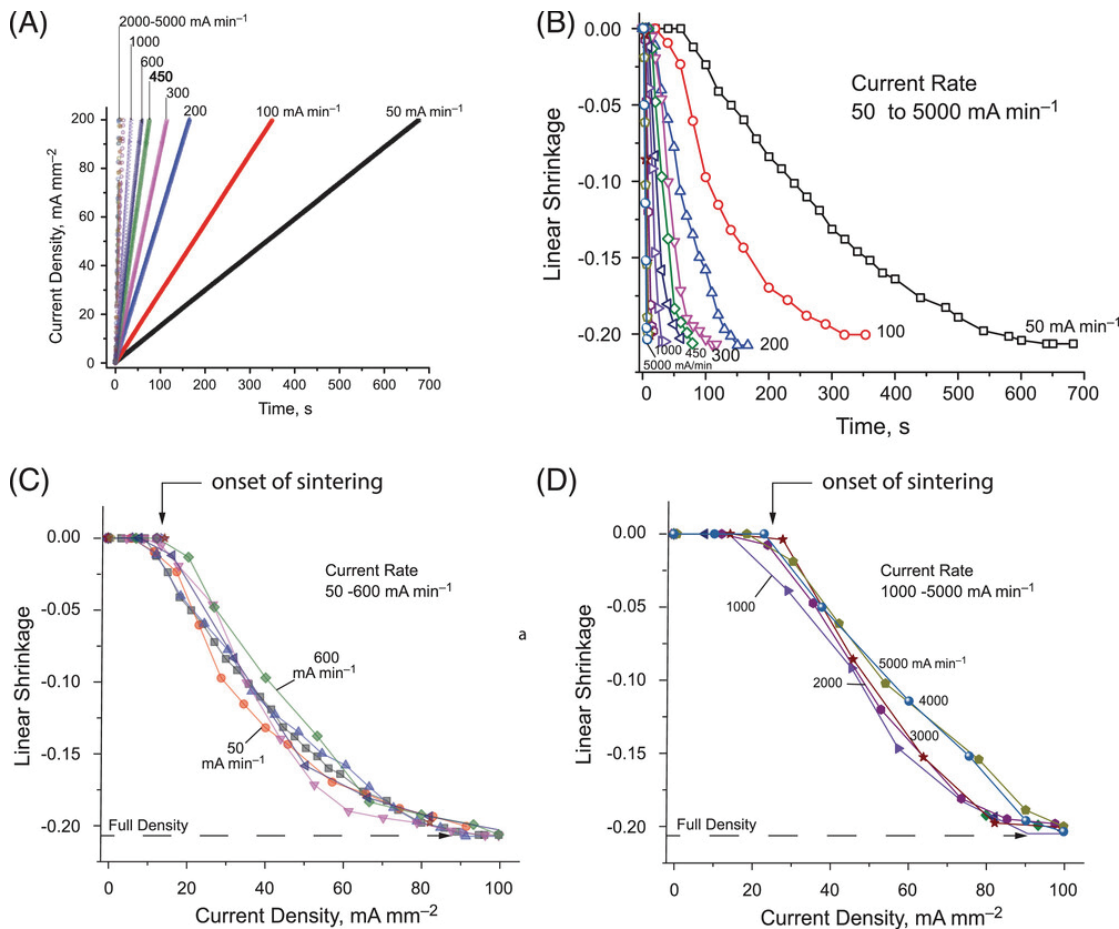
It has been possible to perform in-situ calorimetric measurements during flash by comparing the input electrical power with the estimate of energy expenditure from losses from radiation and convection, and specific heat. The radiation and convection losses could be determined from the measurement of the specimen temperature with a pyrometer. We have consistently discovered an energy deficit, that is, the electrical input is measurably greater than the energy expended in radiation losses. We have attributed this deficit to the endothermic formation of defects, which have been estimated to be many orders of magnitude higher than expected from thermal equilibrium<sup>79</sup>.

The sintering of metals embodies a uniquely simplifying feature: the experiment can be carried out at room temperature, without a furnace, using current-injection to raise the specimen temperature until it flashes and sinters. We present experiments on tungsten powders, with and without a furnace, to assess the influence of furnace heating on the sintering behavior.

Current rate flash sintering was first carried out with yttria stabilized zirconia. Those results are summarized in Figure 5-1. They give the unusual result that the extent of sintering depends only on the instantaneous value of the current density, despite the rate of current having been increased by two orders of magnitude<sup>63</sup>. We show that flash sintering of tungsten exhibits similar behavior.

The objective of the present work is to differentiate between flash sintering in ceramics and metals<sup>63</sup>. We show that sintering of metals can be separated into three regimes: an incubation period that is followed by the onset of electroluminescence, and finally by abrupt sintering to full density. The principal difference is that in ceramics sintering occurs continuously as the current is increased, while in metals it occurs abruptly at a specific current density.

It is possible that flash sintering of metals is equivalent to electro-discharge-sintering, also called electric-discharge-capacitance, capacitor-discharge-sintering, electric-pulse-sintering, and so on<sup>80</sup>, where a large amount of energy stored in a capacitor is dumped within a few milliseconds into a powder-pressed sample of a metal, causing it to sinter. Nevertheless, the ability to understand how current rate can be controlled for time dependent sintering can advance the science of flash. It may also have technological significance: for example, it can be applied to additive manufacturing where small quanta of metal can be sequentially sintered with electrical current for building ready-to-use metal parts.



Adopted from Kumar, Yadav, Lebrun and Raj, 2019, J. Am. Cer. Soc.

Figure 5-1: Current rate flash sintering. (a) The current-time profiles at current rates varying from  $50 \text{ mA min}^{-1}$  up to  $5000 \text{ mA min}^{-1}$ . (b) Shrinkage strain as a function of time at different current rates. (c) and (d) Shrinkage strain plotted against the instantaneous value of the current density, separated into two ranges: current rates  $< 600 \text{ mA min}^{-1}$  on the left, and  $> 1000 \text{ mA min}^{-1}$  on the

right. At the higher rates the collection is shifted slightly to the right because the onset of flash occurs at slightly over  $20 \text{ mA min}^{-1}$  versus just below  $20 \text{ mA min}^{-1}$  on the left.

### 5.3. Methods

Tungsten powder with a particle size of  $12 \mu\text{m}$  was purchased from Alfa Aesar. The powder was cold pressed into dogbone shapes. The specimens for furnace-on experiments had a gage length of 16 mm, width of 3.5 mm and a thickness of 1.45-1.5 mm. Specimens for the furnace-off experiment had a gage length of 20 mm, were 3.3 to 3.5 mm wide and 0.55 to 0.65 mm thick. The powders were pressed without a binder, since the presence of the binder hindered sintering under flash. The pressure of 172 to 200 MPa under a Carver hydraulic press was deployed. The green density of these samples, measured by the Archimedes method ranged from approximately 77 - 80%.

Electrical current to the specimens was supplied by a KEPCO KLN30-100 Power Supply rated for 30 V and 100 A. Small holes, 1.1 mm in diameter were drilled into the ends of the dogbones. Tungsten wire, threaded through these holes served as the electrodes. The flash experiments were done in a glove box, the Genesis model, manufactured by Vacuum Atmosphere Company, USA. Argon gas (99.9% purity) was procured from Airgas, USA. The oxygen level in the Glovebox was kept below 20 ppm.

Current was injected into the specimen from a Kepco power supply. The voltage was measured in a four-point configuration across the two inner electrodes. Since the voltmeter does not draw a current (its internal resistance is designed to be nearly infinite) the measured voltage negates any influence of the interface resistance at the outer electrodes that supply the current through the gage section of the specimen. The ratio of the voltage measured at the inner electrodes and the current injected through the outer electrodes are plotted as an I-V curve, the slope of which gives the resistance in  $\Omega$ . Multiplying by the cross section of the specimen and dividing by the gage length between the inner electrodes yields the specific resistivity of the metal in units of  $\Omega \text{ cm}$ .

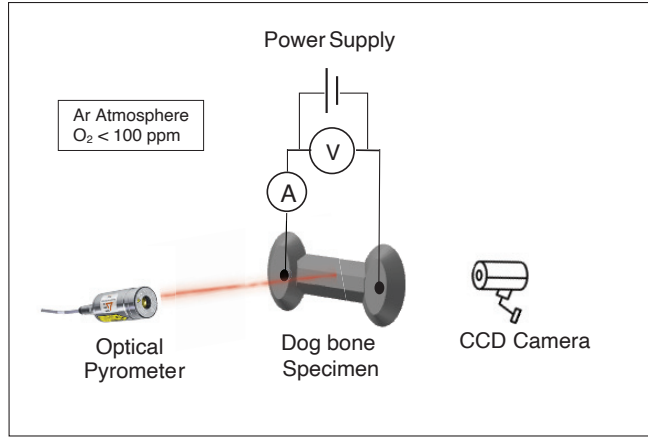


Figure 5-2: Illustration of Flash Sintering setup for tungsten

Two types of experiments were performed, one with furnace heating and the other without. A schematic of the furnace-off experiment is shown in Figure 5-2. The furnace can be added to this schematic for the furnace-on experiments. The furnace was set at 800°C for all furnace-ON experiments.

The specimen was imaged in real time with a CCD camera manufactured by Imaging Source (Germany) at a rate of 10 frames per second. The optical emission spectrum was measured with a spectrometer (USB4000-UV-VIS) manufactured by Ocean Optics (USA). The spectrometer was focused on the specimen through a collimating lens connected to an optical fiber which was interfaced with the Ocean Optics hardware and read into the computer.

The specimen temperature was measured with a CTLM-1HCF4-C3 pyrometer manufactured by Micro-Epsilon (USA) (CT-SF22-C8). The emissivity was set at 0.35<sup>81</sup>. The data collected from the pyrometer were converted to temperature using our data acquisition software. The pyrometer readings were calibrated against the furnace temperature with a dummy specimen for different values of the emissivity, from 0.25 to 0.35. They gave a 50 °C range for the difference between the furnace temperature measured with a thermocouple and the pyrometer reading for this range of emissivity. Thus, the data presented below may contain an error-bar of 50°C.

Home built software<sup>63</sup> was used to control the rate of current injection (which was varied from 0.1 to 10 A per sec). The data were interfaced to the computer software with a National Instrument Data Acquisition (NI DAQ) card. The current from the power source was recorded as a function of time. The sintering strain (contraction) was measured from images acquired with the CCD camera, using Fiji, an Image software. The shrinkage,  $\epsilon$  was obtained from:

$$\epsilon = \ln\left(\frac{L}{L_o}\right) \quad (5-1)$$

where  $L$  is the length measured as a function of time during sintering,  $L_o$ , the initial length is set equal to the holes drilled to carry the current from the electrodes.

The volumetric shrinkage,  $\epsilon_a$ , which is related to the green density,  $\rho_g$ , and the live density,  $\rho$ , is described by the following equation:

$$\epsilon_a = 3\epsilon = \ln\left(\frac{\rho_g}{\rho}\right) \quad (5-2)$$

The theoretical density of tungsten was set equal to, 19.3 g/cm<sup>3</sup>, for the purpose of calculating the relative density.

The tungsten powder used in the present study was analyzed using a LECO oxygen analyzer to obtain the oxygen composition of the powder. The experiment was performed in the NASA Marshall Space Flight Center facility in Alabama. The result showed low oxygen composition with an average value of 0.07725 wt %. The full result obtained is given in Table 5-1.

Table 5-1: W unaltered oxygen composition in %wt.

Test	Oxygen Composition (wt. %)
Test 1	0.07801
Test 2	0.07721
Test 3	0.07654

Average Result	0.07725

## 5.4. Results

The results are presented in terms of the current density, or time. They are equivalent parameters since the current rate was held constant. Five current rates ranging from  $0.1 \text{ A s}^{-1}$  to  $10 \text{ A s}^{-1}$  were employed. Sintering occurred at about 200 s at  $0.1 \text{ A s}^{-1}$ , and in just 2 s at  $10 \text{ A s}^{-1}$ .

Three types of results are presented: (i)) sintering as a function of time or current density, (ii) the change in resistance, (iii) the change in temperature with time as the specimen flashes and sinters, and (iv) the estimate of the endothermic enthalpy estimated from the difference between the input electrical energy and the energy dissipated by radiation and convection and stored as specific heat.

After the first sintering cycle, Cycle-1, the specimen becomes a dense polycrystal. The flash cycle was repeated twice on this specimen, called Cycles-2 and Cycle-3. The flash in powders involves an abrupt removal of particle-particle interface resistance which is not present in Cycles-2 & 3. These latter cycles were highly reproducible pointing towards removal of defects when the current is turned off, and reintroduction of defects when the cycle is repeated. It is these cycles with dense specimens that are used to draw conclusions about the nature of the flash behavior.

### 5.4.1. Sintering

We measured the linear strain according to Eq. (5-1), which can be translated into relative density with Eq. (5-2), using the green density to be approximately  $\rho_g \approx 0.77$ . The results for experiments carried out at current rates ranging from  $0.1 \text{ A s}^{-1}$  to  $10 \text{ A s}^{-1}$ , are shown in Figure 5-3. The maximum sintering strain is approximately 8.0 to 8.5%. The application of Eq. (5-2) then yields finish density of ~98% to 100%.

The sintering data from furnace-ON experiments are given in Figure 5-3. All samples sintered to full density, as is evident from the saturation of the sintering strain. The time for sintering was as short at 2 s at  $10 \text{ A s}^{-1}$ , lengthening to about 250 s at  $0.1 \text{ A s}^{-1}$ . Full sintering was achieved at a current density of  $6 - 8 \text{ A mm}^{-2}$ . The coalescence of the data when plotted against the current density shows that densification is independent of the current rate, and that the current density is the key parameter in flash sintering. This result is similar to the behavior in 3YSZ presented in Figure 5-1 with one difference. In the case of the ceramic, densification occurred continuously with current, whereas, here, all densification takes place abruptly at a certain value of the current density.

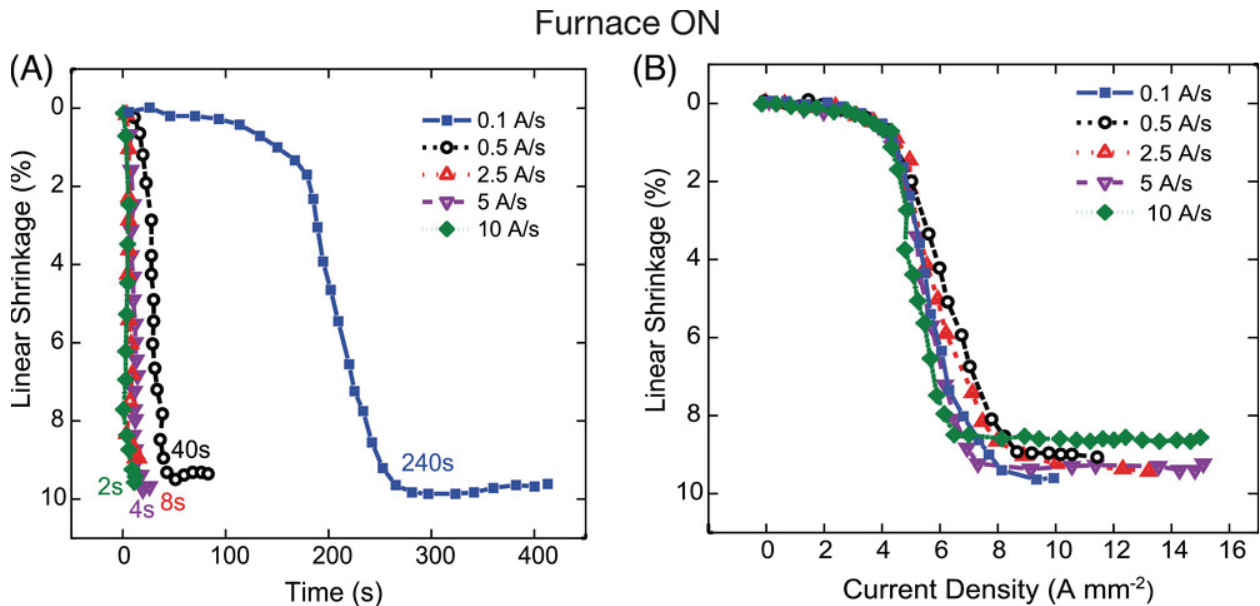


Figure 5-3: (a) Linear shrinkage measured as a function of time while the current is increased at constant rates, ranging from  $0.1 \text{ A s}^{-1}$  to  $10 \text{ A s}^{-1}$ . (b) When the strain is plotted against the current density then the data for all current rates merge into a master curve, suggesting current density as the fundamental sintering parameter.

A similar behavior is seen in the furnace-OFF experiment, carried out at  $0.1 \text{ A s}^{-1}$ , given in Figure 5-4. The experiment was repeated twice to check reproducibility. The difference between the furnace-off and furnace-on experiments is the current density for the onset of sintering, which is  $20 \text{ A mm}^{-2}$  without, and  $6 - 8 \text{ A mm}^{-2}$  with the furnace. The higher current density for the furnace-

off case means that both the temperature of the specimen, as well as the current density, play a role. The furnace temperature of 800°C partly compensates for the Joule heating provided by the current density, that is, less current is needed to reach the desired temperature for the onset of sintering.

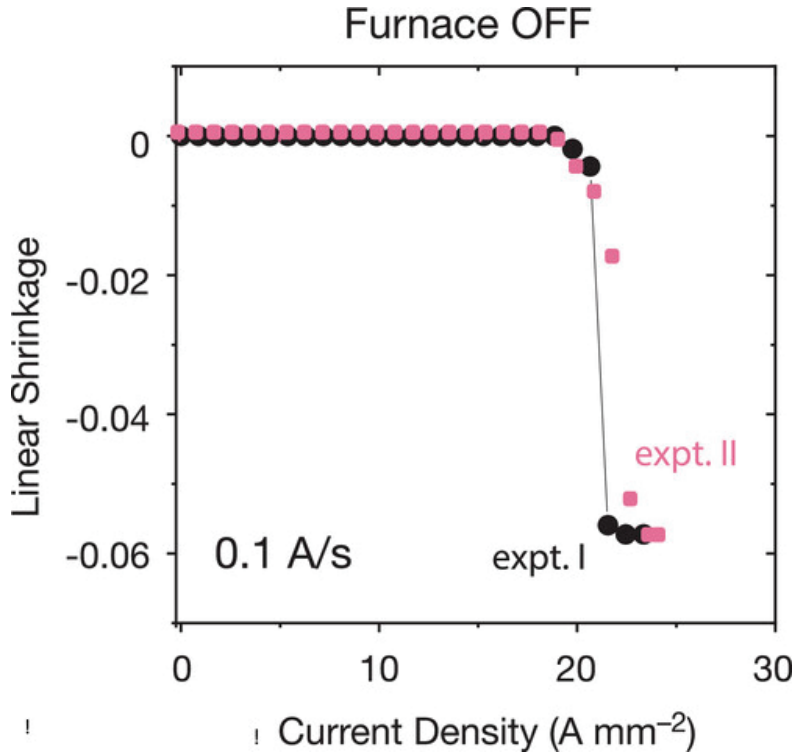


Figure 5-4: Sintering behavior at 0.1 A/s, repeated twice.

#### 5.4.2. Measurement of Resistivity

The specific resistivity of tungsten was measured by the four-point method. The experiments were done not only in the initial sintering cycle (Cycle 1) with the powder-pressed dogbone sample, but again after sintering, which was repeated in Cycles 2 and 3. These data for the furnace-OFF experiments are given in Figure 5-5. The resistance shows a transient peak (at 1200 mW) in the first cycle presumably from the abrupt breakdown of the resistance at particle interfaces, which was likely due to thin oxide films. The decline in resistance past the peak is attributed to the sintering of pores. Once sintered the resistance is seen to rise with temperature. The sample is fully sintered after the first cycle. This sintered specimen when flashed again in Cycles 2 and 3 shows

consistent behavior. However, the shape of the curve is different, and also higher relative to the literature data<sup>82</sup>. These differences are attributed to flash-generated defects such as vacancy-interstitial pairs. (The current density was converted to specimen temperature from pyrometer data, which is described in the next section.)

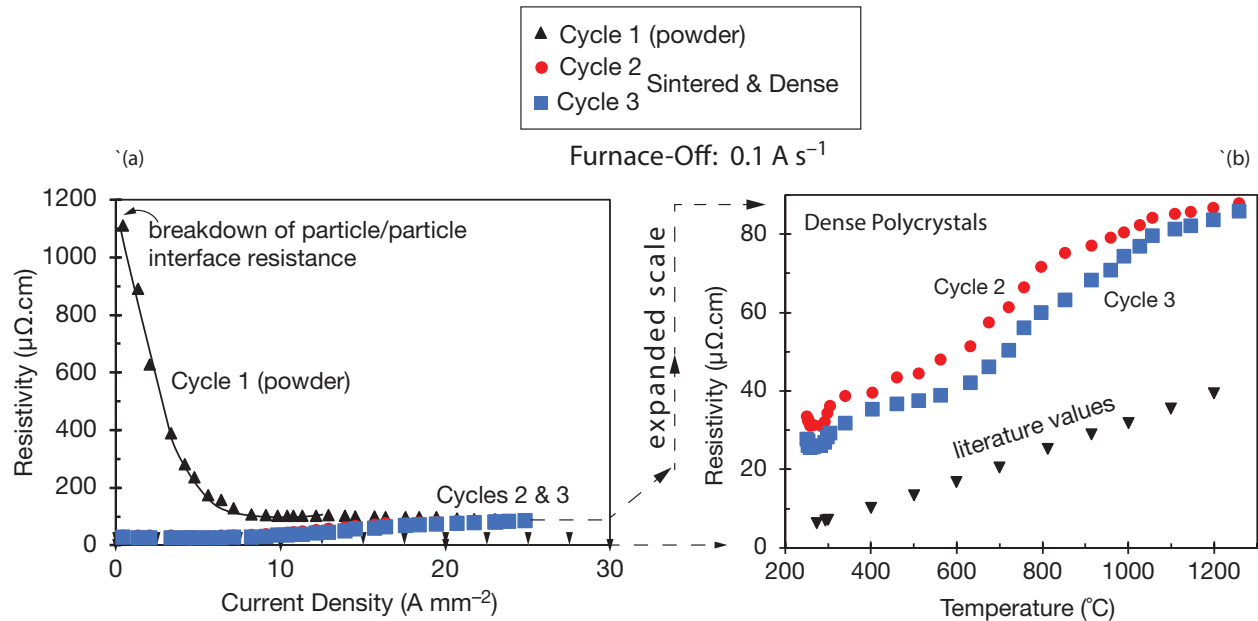


Figure 5-5: (a) Change in resistivity with current density during flash sintering of green tungsten compact, and two cycles of flash of dense tungsten compact with flash history. (b) Comparison of resistivity vs temperature during the two cycles of re-flash with the handbook reference values.

#### 5.4.3. Measurement of Temperature

The temperature was measured with the pyrometer. The literature value for the emissivity of tungsten is 0.35. The pyrometer was calibrated with respect to the furnace temperature by focusing it on a tungsten specimen (without current) placed within the furnace. The pyrometer measurement, with the emissivity set at three values, 0.25, 0.30 and 0.35 were compared. Programming the pyrometer with a lower emissivity yielded a slightly higher temperature. The spread between the high and the low emissivity ranged from 10 to 25°C. The data are presented graphically in Figure 5-6. Accordingly, the specimen temperature was about 50°C higher than the furnace temperature, presumably because the

furnace thermocouple was placed near the outer body of the furnace. Therefore, the temperature measured with the pyrometer is assigned an error bar of  $\sim 50^\circ\text{C}$ .

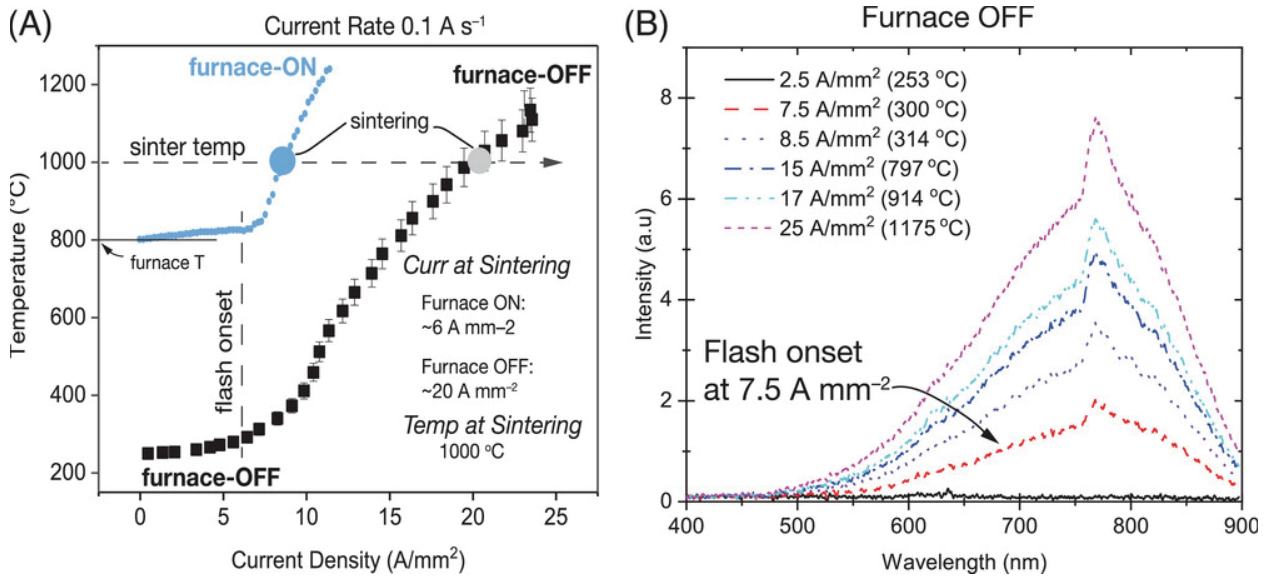


Figure 5-6: (a) Plot of Temperature vs Current Density for both furnace-ON and furnace-OFF experiments (b) Optical emission spectra for furnace-OFF experiment

The temperature of the specimen was measured continuously during the process of flash sintering. The results for furnace-off and furnace-on experiments are shown together in Figure 5-6 (a). A comparison between these two sets of data is highlighted by the following features:

- (i) The first inflection in the curves for both cases occur at approximately  $\sim 7 \text{ A mm}^{-2}$ , after which the temperature remains at a slightly elevated plateau, even though electrical energy is being injected at a steadily increasing rate. It seems reasonable to infer that the energy imparted by the increasing current density without an increase in the specimen, is used up in the endothermic reaction of defect formation.
- (ii) The onset of electroluminescence, given in Figure 5-6(b), also starts at the above point of inflection (at  $\sim 7 \text{ A mm}^{-2}$ ).
- (iii) A third feature of Figure 5-6 (a) is the temperature for the onset of full sintering. The current density at sintering was shown in Figs 3 and 4. It occurs at  $6 - 8 \text{ A mm}^{-2}$  for the furnace-

on condition, and at  $20 \text{ A mm}^{-2}$  for the furnace-of condition. However, in both cases the specimen temperature is  $\sim 1000^\circ\text{C}$ .

The above discussion leads to a pattern for the progression of flash sintering in metals during current rate experiments. The phenomenology may be separated into three steps: at first there is an incubation time, which is followed by the temperature rising towards a plateau, and finally an upward trajectory of the temperature when the sample sinters. The first transition, which occurs near  $7 \text{ A mm}^{-2}$ , is accompanied by electroluminescence. During the plateau defects continue to form, consistent with an increasing intensity of luminescence, seen in Figure 5-6 (b). At some point, it seems that the defect density reaches a saturation point and the temperature begins to rise with the current density. Why sintering occurs at this saturation point is not clear. It is also not understood why sintering occurs at the same temperature ( $\sim 1000^\circ\text{C}$ ) with or without the furnace. The current density at sintering is lower with the furnace since less current is needed to reach this critical temperature.

#### **5.4.4. Calorimetry: Endothermic Enthalpy**

In our experience in flash experiments with both metals and ceramics, we have discovered a discrepancy between the input electrical energy and the temperature dependent losses in the form of radiation, convection and specific heat<sup>63,83</sup>. This difference, the energy deficit, is attributed to the endothermic generation of defects. The analysis allows an estimate of the concentration of defects being generated from the ratio of the energy deficit and the heat of formation of the defects. We apply this analysis to the present experiments.

We write the equation for the energy deficit,  $\Delta H^*(t)$ , in Joules, as:

$$\Delta H^*(t) = \int_0^t (W(t) - W^*(t)) dt \quad (5-3)$$

where  $W(t)$  is the electrical work expended (in Watts) into the sample, and  $W^*(t)$  is the energy lost to radiation, convection and specific heat. The electrical work is obtained from the electrical measurements of voltage and current.

The energy loss is the sum of three terms: black body radiation, convection loss and the energy stored as specific heat:

$$W^*(t) = W_{BBR}^*(t) + W_{conv}^*(t) + W_{spht}^*(t) \quad (5-4)$$

Each of the above terms are given by the following expressions:

$$W_{BBR}^*(t) = \epsilon_m S \sigma (T_K^4 - 298^4), \quad (5-5)$$

$$W_{conv}^*(t) = hS(T_K - 298), \quad (5-6)$$

$$W_{spht}^*(t) = mC_p \frac{dT_K}{dt} \quad (5-7)$$

Note that the terms in (5-5 to 5-7) are in units of Watts, that is  $J s^{-1}$ . Here,  $S$  is the surface area of the specimen,  $\epsilon_m$  is the emissivity of tungsten (equals to 0.35),  $\sigma$  is the Stefan-Boltzmann's constant ( $5.6704 \times 10^{-8} \text{ W/m}^2\text{K}$ ). 298 K is the ambient temperature (since the experiment was carried out without the furnace. "m" is the mass of the specimen (equals to 0.000326 kg), and the specific heat,  $C_p$  is equal to 133 J/kgK.  $T_K$  is the specimen temperature in Kelvin measured with the pyrometer. Substituting Eqns (5-4) and (5-5, 5-6, 5-7) into (5-3) gives the estimate of the energy deficit in Joules after the right-hand side in Eq. (5-4) is integrated with respect to time.

The value for  $h$ , the convective heat transfer coefficient in Eq. (5-6) needs further attention. Its value in air can range from 10 to 100  $\text{W m}^{-2} \text{ K}^{-1}$ . It varies with the chemistry and morphology of the surface, the relative velocity of gas at the interface, and the heat carrying capacity of the gas which depends on its pressure and specific heat. For example, Ar has a much lower heat capacity than N<sub>2</sub>; therefore, in Ar (used in present experiments) the heat transfer coefficient will be lower than in air.

The convective loss increases linearly with T while BBR increases as  $T^4$ . Therefore, convection dominates at low temperatures but crosses over to BBR at higher temperature. The value for  $h$  was assigned by assigning the generally accepted cross-over temperature to be about 600°C. It is when the emission color is of mildly red heat, nominally considered the point where the loss transitions from convection to BBR. Such a plot for our data is given in Figure 5-7, which shows that the transition occurs near 600°C when  $h = 20 \text{ W m}^{-2} \text{ K}^{-1}$ .

The next step is to reduce  $\Delta H^*$  in Eq. (5-3) to a molar quantity, which is done by first by calculating the number of moles of tungsten in the specimen, as given by:

$$N_W = \frac{V_{\text{specimen}}}{V_{\text{molar}}} \quad (5-8)$$

Therefore, the enthalpy in Eq. (5-3) as a molar quantity is given by:

$$\Delta H_{\text{mol}}^* = \frac{\Delta H^*}{N_W} \quad (5-9)$$

The mole fraction of defects formed in the specimen is obtained by dividing Eq. (5-9) by the energy of formation of the defects,

$$x_F = \frac{1}{E_F N_W} \frac{\Delta H^*}{\Delta H_{\text{mol}}^*} \quad (5-10)$$

where  $E_F$  is the energy of formation of Frenkels in Joules  $\text{mol}^{-1}$ .

By substituting  $V_{\text{specimen}} = 20.65 \times 10^{-3} \text{ cm}^3$ ,  $V_{\text{molar}} = 9.5 \text{ cm}^3 \text{ mol}^{-1}$  and  $E_F = 13.04 \text{ eV}$  for the energy of formation of Frenkel pairs in W, converted into  $\text{J mol}^{-1}$  by multiplying eVs by 96,500, we obtain the results shown in Table 5-2. The following method for used to calculate the results given by Eq. (5-9) and (5-10). The experimental inputs were the temperature (measured with the pyrometer) and the electrical input watts, both as a function of time. The temperature was translated into the parameters on the left-hand side of Eq. (5-5 – 5-7); the watts were converted into Joules by integrating with time.

The Joules stored as specific heat were added to the sum of the BBR and convection, to obtain the total energy loss. The input energy was calculated from the integrating the input power with respect to time. The former subtracted from the latter gave the magnitude of  $\Delta H^*$  which was inserted into Eq. (5-10) to obtain the mol fraction of Frenkel defects. The results from the above analysis are given in Table 5-2.

Table 5-2: Analysis of time, temperature, electrical power input for obtaining the energy deficit, and from that the mole fraction of Frenkel defects.

Time	Pyrometer Temp	Watts	BBR	BBR	Convec	Convec	Spec	Total IN	total loss	Deficit	Frenkel
sec	°C	W	total J	W	total J	total J	J	J	kJ/mol	mol fraction	
217	341	1.81	0.2	26	0.44	77	14	229	117	52	0.032
234	403	2.07	0.3	5	0.53	86	16	265	107	72	0.045
247	460	2.28	0.4	10	0.61	94	19	295	123	79	0.049
256	511	2.47	0.5	14	0.68	100	21	317	136	83	0.052
269	562	2.72	0.7	23	0.75	110	23	353	157	90	0.056
289	632	3.17	0.9	41	0.85	127	26	415	195	101	0.063
306	674	3.56	1.1	61	0.91	143	28	477	231	113	0.070
331	722	4.11	1.3	94	0.97	166	30	578	290	132	0.082
346	757	4.40	1.5	117	1.02	182	32	643	330	144	0.089
373	797	5.03	1.8	165	1.08	211	33	779	410	169	0.105
389	852	5.38	2.2	201	1.16	229	36	865	466	183	0.114
418	914	6.24	2.7	282	1.24	266	39	1049	586	212	0.132
438	958	6.84	3.2	344	1.31	292	40	1183	677	232	0.145
462	990	7.62	3.5	431	1.35	325	42	1371	798	263	0.164
492	1026	8.20	3.9	548	1.40	366	43	1613	957	301	0.187
517	1056	8.93	4.3	654	1.44	402	45	1833	1100	336	0.209
546	1109	9.80	5.1	803	1.52	446	47	2122	1296	379	0.236
548	1132	9.81	5.4	816	1.55	450	48	2146	1314	381	0.238
567	1175	10.34	6.1	927	1.61	480	50	2334	1457	402	0.251
590	1209	11.07	6.7	1085	1.66	519	51	2596	1655	432	0.269

Plots for the energy deficit in  $\text{kJ mol}^{-1}$  and the corresponding mol fraction of Frenkels pairs are shown in Figure 5-7(b)&(c). It is rather remarkable (even incomprehensible) that the defect concentration

reaches as high as 26% mol fraction. The value calculated from thermal equilibrium is many orders of magnitude smaller. We have checked our experiments and number crunching to be sure. These numbers are perhaps okay since we measure a volume expansion of >5% during flash: interstitial vacancy pairs carry a small volume expansion. The defect generation also appears to be different for nickel: as reported in a subsequent manuscript we report a mol fraction of 3% (which is still very large).

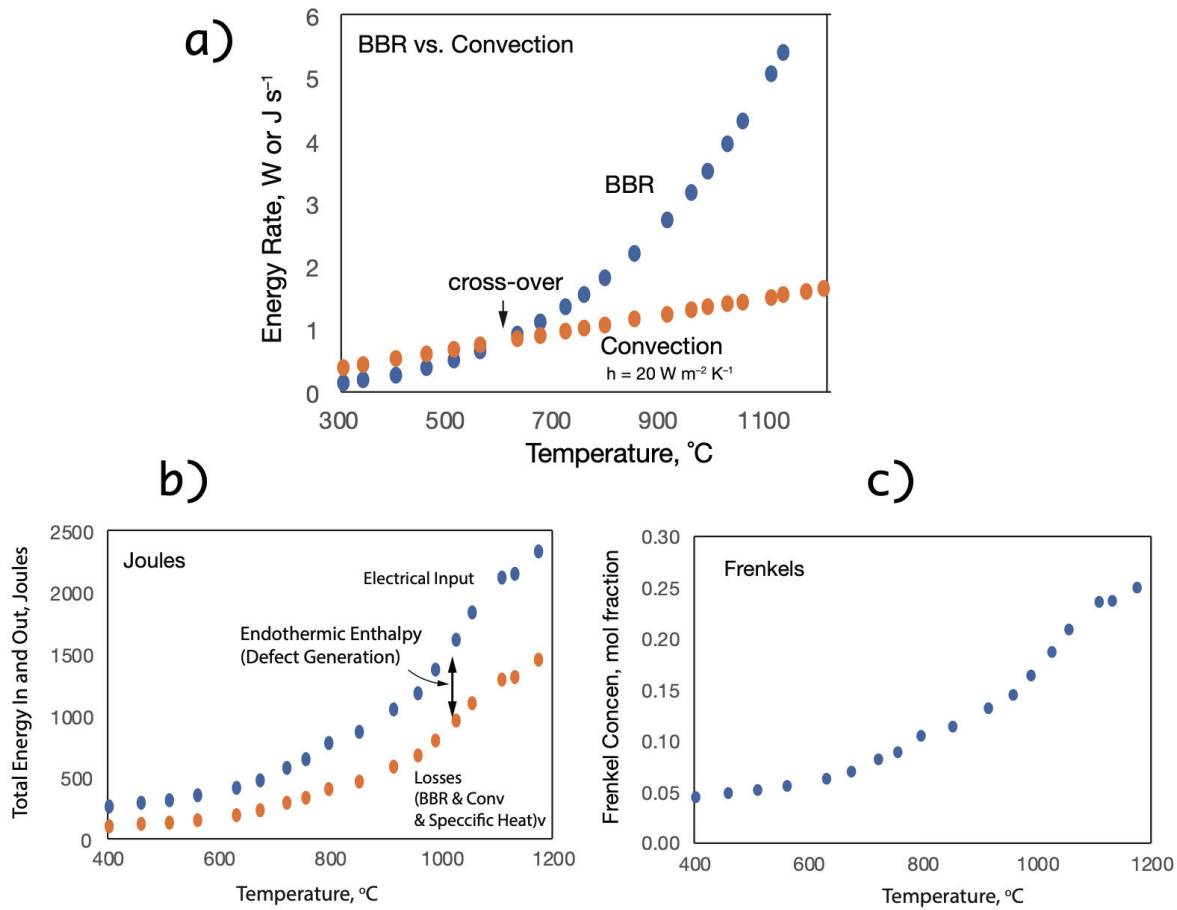


Figure 5-7: (a) Plot of BBR and Convection losses as a function of temperature. (b) Energy deficit calculated as a difference between the input power and the power predicted from the BBR, Convection and specific heat. (c) Mol fraction of Frenkel pairs generated during flash sintering of tungsten without furnace

The large mole fraction of defects reflects a new paradigm in the “flash-ecosystem”, which is emerging as a far from equilibrium phenomenon, which with chemical reactions and mass transport by diffusion occur at astronomical rates.

### 5.4.5. Molecular Dynamics Simulation

The athermal generation of Frenkel pairs has been thought to arise from non-linear lattice vibrations, which are possible only if the phonon wavelengths are less than or equal to the lattice parameter, that is at the edge of the Brillouin Zone, with the practical implication that the defects can form only above the Debye temperature. This hypothesis was validated by experiments where three oxides were shown to flash only when above Debye<sup>84, 85</sup>. Molecular dynamics simulations with single crystals aluminum also proved that Frenkel pairs could be generated by proliferation of such phonons<sup>86</sup>. These results are described in Figure 5-8.

Figure 5-8(a) shows the influence of continuous injection of current density on the change in the temperature of the crystal. The temperature rises up to the Debye temperature but then plateaus since the energy is consumed by the generation of defects as shown in Figure 5-8(b). It is interesting that the Frenkel concentration does not increase smoothly but in abrupt steps.

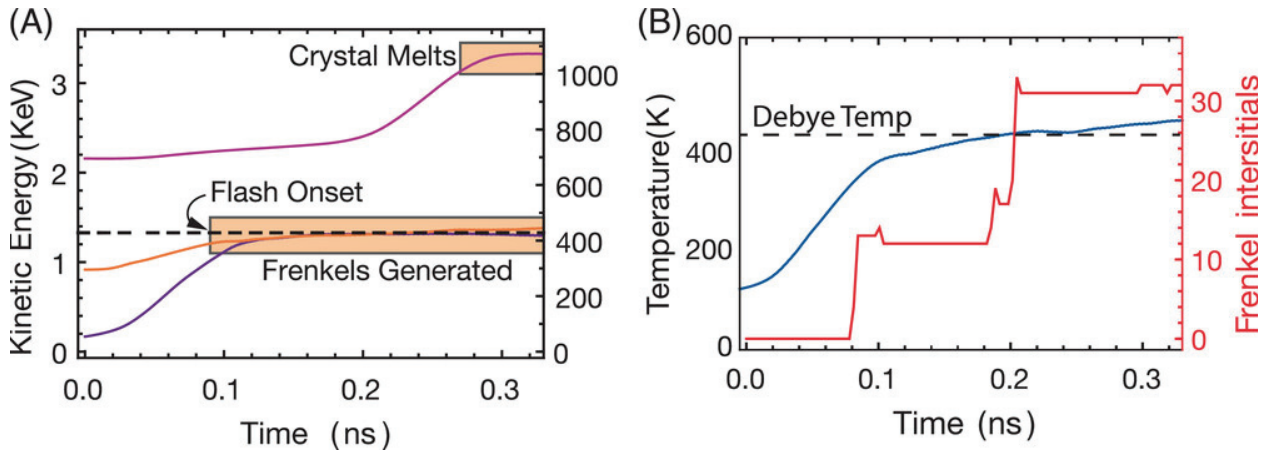


Figure 5-8: (a) Kinetic energy of phonons injected into an aluminum single crystal at first raises the temperature but then plateaus above the Debye Temperature. Thereafter, as shown in (b) the energy is consumed in the generation of Frenkel pairs. This behavior is similar to the data in Figure

5-4 where the temperature of the specimen does not increase as the current density is increases (up to  $7.5 \text{ A mm}^{-2}$ ).

#### 5.4.6. Phenomenological Description of Flash in Metals

The pattern of flash sintering behavior in the present work is similar to experiments of flash sintering of Ni (Section 7 of this thesis). The behavior when plotted as a function of temperature show similar behavior. One interesting observation is that, in both Ni and in W, the change in resistance differs significantly from the literature values, most likely reflecting the influence of defects that are generated during the flash process.

As shown in Figure 5-9 the general features are reflected similarly in the change of resistance as well as the estimate of the Frenkel pairs described in Section 5.3.4. They consist of an incubation time up to the onset of luminescence, which is followed by a shallow plateau in temperature and generation of defects. Finally, the temperature turns upwards, and sintering occurs abruptly. Similar behavior was observed in Ni.

Sintering in flash is quite different than conventional sintering. For example, let us compare Ni and W, with melting points of  $1455^\circ\text{C}$  and  $3383^\circ\text{C}$ . Normally diffusion rates that occur at  $0.75T_M$  are needed for sintering within a few hours. Therefore, conventional sintering of tungsten requires much higher temperatures ( $\sim 2450^\circ\text{C}$ ) than nickel ( $\sim 1023^\circ\text{C}$ ). In flash both metals sinter at a temperature of  $1000^\circ\text{C}$  (for specimens of similar geometry) they sinter at a similar current density. Furthermore both sinter at a current density of  $\sim 20 \text{ A mm}^{-2}$ .

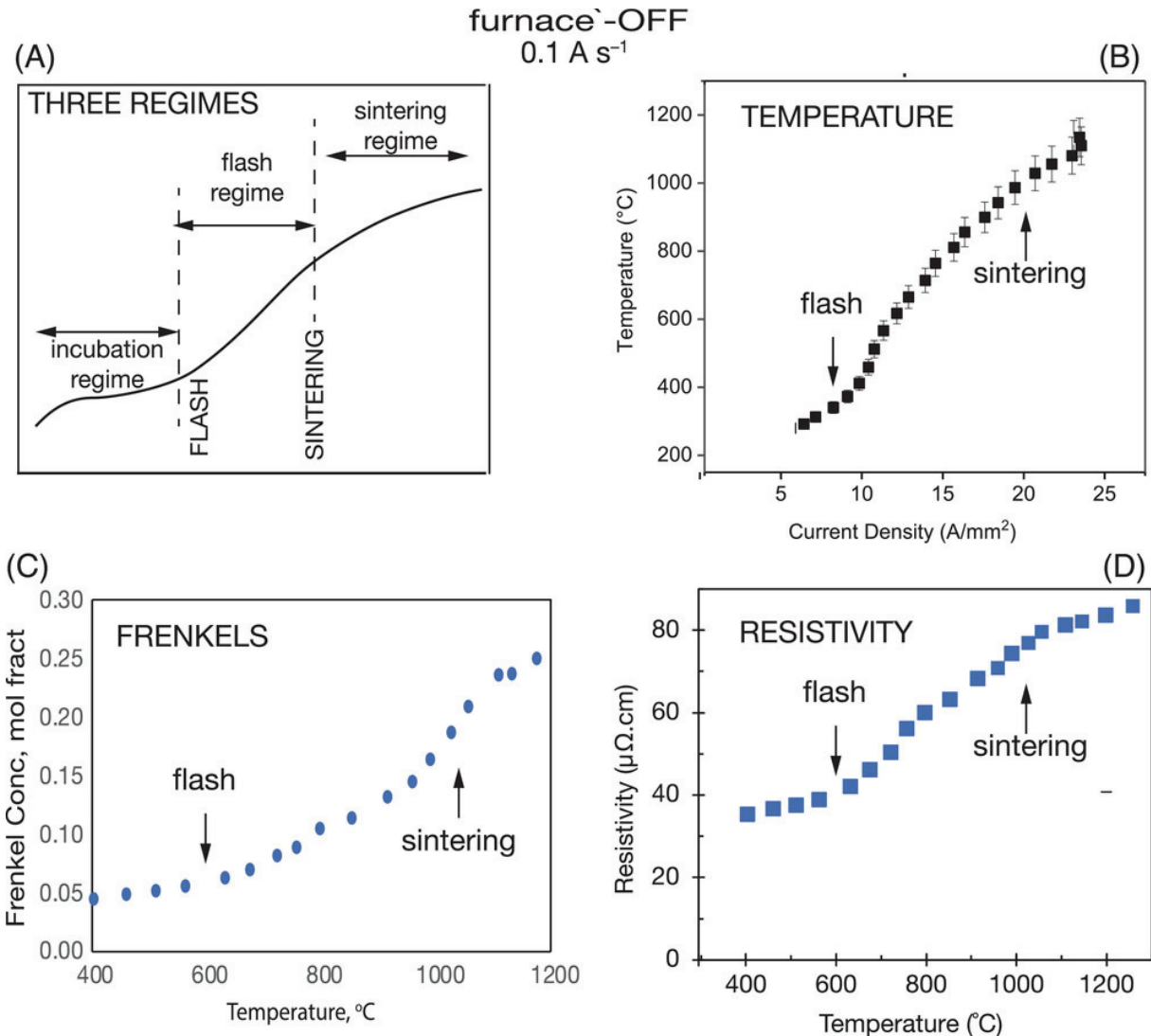


Figure 5-9: (a) The three regimes characterizing the phenomenological behavior in flash sintering of metals; the transitions are prescribed by three regimes: the incubation regime, followed by the flash regime, followed by the sintering to full density. The measurement of (b) temperature, (c) the estimate of defect generation, and (d) the resistivity, consistently show this three-regimes pattern.

#### 5.4.7. Microstructure and Hardness

The microstructure of the specimens was obtained from cut and polished cross sections. The specimens were mounted using Allied QuickCure powder and liquid, then cured at room temperature for 5 minutes. The mounted specimens were polished using a LECO VP-160 polishing machine using polishing papers ranging from  $240 \mu m$  to  $1 \mu m$ . The specimens were then rinsed,

dried, and etched using a 30% hydrogen peroxide for 60s. The etched specimens were immediately rinsed in water.

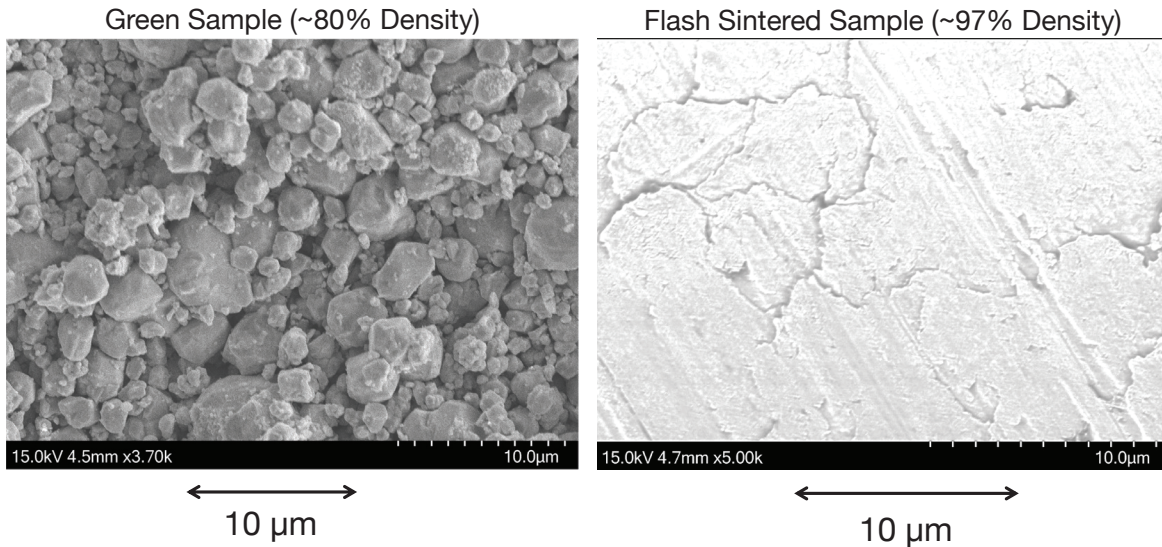


Figure 5-10: The microstructure of the sample before and after sintering. The grain size of the sintered sample was nearly the same as the size of the particles in the powder, approximately 12  $\mu\text{m}$ .

A Hitachi SU3500 SEM (Colorado Shared Instrumentation in Nanofabrication and Characterization - COSINC) was used to observe the microstructure of the specimens. The micrographs were obtained in the back scattering mode at 15 kV. The micrographs of the unsintered and sintered samples are shown in Figure 5-10. The grain size in the sintered samples is about three to four times the size of the powder particles, about 12 mm. Therefore, significant grain growth took place during sintering.

Vickers Hardness was measured using the standard ISO 6507-12018 via the Rockwell Hardness tester situated in Idea Forge, University of Colorado Boulder with a diamond indenter. The hardness value was obtained using:

$$H_v = \frac{2F \sin \frac{136^\circ}{2}}{d^2} = 1.854 \frac{F}{d^2} \quad (5-11)$$

where  $d$  is the average diagonal length of the indentation in mm and  $F$  is the load applied in kgf.

Twelve measurements were made with 12 kgf, and one with 45 kgf. The image of the indentation was captured using optical microscope and the diagonal was measured using Fiji software. The HV for 12 kgf ranged from 393 to 596. The measurement with 45 kgf gave HV 438. The average of all these values, 467 is given in Table 5-3. The data from other methods was obtained from Tan et. al.<sup>87</sup> The flash sintered specimens gave hardness values that are quite comparable with literature values.

Table 5-3: A comparison of the hardness values for the current specimens and those processing in different ways from the literature<sup>88</sup>.

<b>Fabrication Method</b>	<b>Relative Density (%)</b>	<b>HV</b>
Selective Laser Melting	97 – 98	445 – 467
Chemical Vapor Deposition	$\leq 99.79$	419
Powder Metallurgy	$\leq 98$	320 – 400
Hot Isostatic Pressing	$\leq 98.20$	344
Spark Plasma Sintering	$\leq 96.30$	372
<b>Flash Sintering</b>	<b><math>&gt; 98</math></b>	<b>467</b>

## 5.5. Discussion

The present work is the first conclusive example of the application of flash to metals. The earliest evidence of possible flash in metals were experiments by McWilliams et al.<sup>89</sup> with aluminum powder, where an abrupt increase in densification was attributed to the breakdown of the oxide films. More recently Mazo et al.<sup>90</sup> have shown sintering of tungsten carbide with electrical activation. Graphitization of amorphous carbon under flash was demonstrated by Ingraci and Raj<sup>91</sup>.

While ceramics require furnace heating to initiate flash sintering, metals do not. They can be sintered at room temperature by direct injection of current. Nevertheless, we have presented results with and without a furnace. Interestingly, in both cases sintering occurs when the specimen reaches 1000°C.

The current density to reach this temperature is of course lower ( $7.5 \text{ A mm}^{-2}$ ) with furnace heating, than without the furnace ( $20 \text{ A mm}^{-2}$ ) because heating with the furnace lowers the requirement on current density for reaching  $1000^\circ\text{C}$ .

The measurements of the change in specific resistivity with temperature differ from those reported in literature. Whereas nominally the resistance increases monotonically with temperature, the in-operando flash data show inflexions. At first the resistance exhibits a shallow plateau, rising slowly with temperature. It transitions into rising value with a high slope at higher temperature, and then bends over to a lower slope similar to the literature values.

The unusual shape of the resistance vs. temperature curve as described above may contain information regarding the generation of defects during flash. Indeed, the estimate of defect concentrations from energy deficit calculations, shown in Figure 5-7b shows a shape that is similar to shape of the resistance curve. Such concentrations of Frenkel defects are many orders of magnitude greater than expected from thermal equilibrium.

The result in Figure 5-3, where the sintering strain is shown to be independent of the current rate is intriguing. We rationalize this unusual result by recognizing that the rate of mass transport by diffusion depends on the product of the defect concentration and the mobility of defects. If the defect concentration is very large, then it may weaken the influence of mobility on the rate of mass transport. Since the defect concentration depends on the current density, it can be postulated that sintering will also predominantly depend on the current density.

In closing, it must be said that sintering of tungsten powder with electrical currents was practiced more than a century ago<sup>92</sup> in the quest of fabricating fine ductile tungsten wire for incandescent lamps. Eventually this process succeeded in trapping bubbles of potassium which having a high vapor pressure could be retained only if the sintering was accomplished in split seconds. These bubbles stretch out

into a string of bubbles during hot extrusion. Thus, they restrain grain growth in the transverse direction of the wire, yielding pseudo-single crystal structure which is highly creep resistant<sup>93</sup>. RR still retains vivid memory of a visit to Westinghouse Electric in Broomfield NJ to visit Dr. G. W. King, in the late seventies, where he saw a powder ingot of W anchored at one end to a high current electrode with the other end immersed in liquid mercury which literally sintered almost instantaneously with a bright glow when the current was energized. It must have been what is going on here.

## 5.6. Conclusion

The present experiments on W confirmed that metals can be flash sintered just like ceramics. Metals are unique in that they can be sintered without a furnace by injecting current and increasing it at a constant rate. However, sintering depends only on the instantaneous value of the current density: it is independent of the current rate.

In conventional sintering temperature and time control the rate of sintering, which requires a furnace. In flash sintering consolidation is achieved, without a furnace, by injecting “energy” directly into the specimen. Thus, electrical energy is immediately transferred into the chemical work required for sintering. Thus, flash carries a huge benefit in energy efficiency. Simple estimates show that flash uses <1% of the energy used in conventional processing.

The energy efficiency of flash sintering can be compared to the electrification of cars where electrical power is injected directly into motors that drive the wheels, thereby sidestepping energy inefficient internal combustion engines. Here, electrical energy is injected directly into the work piece for doing the work of sintering, obviating the need for large furnaces that waste heat. The electrification of manufacturing of metals and ceramics, suddenly seems a possibility.

The present experiments are quite different from electro-discharge-sintering where a large quantum of energy stored in a capacitor is dumped into the metal in few tens of milliseconds to achieve sintering.

Here, sintering is controlled by a measured rate of current injection which can stretch the sintering time from a few seconds to several minutes.

Finally, we see an application of flash sintering of metals in the manner shown here in additive manufacturing for producing ready to use, dense workpieces.

## 6.0. Flash Sintering of Rhenium at Ambient Temperature in < 1 Minute with Electrical Current<sup>2</sup>

### 6.1. Summary

We show that rhenium can be sintered from powders to nearly full density (99.96%) by the direct injection of current (without a furnace) into dogbone shaped specimens in Ar atmosphere (< 100 ppm O<sub>2</sub>). The current was increased at a rate of 1 A/s. The specimen sintered at a current density of 24 A mm<sup>-2</sup>, at when the specimen reached a temperature of 900°C. The following in-operando measurements are reported, (i) shrinkage strain with a rapid rate camera, (ii) resistivity measured by in-situ voltage and current, (iii) temperature measured with a pyrometer, and (iv) electroluminescence characterized with a spectrometer. The sintering cycle, during which the sample sintered to full density, was followed by two more flash cycles with dense specimens. In the first cycle the change in resistance exhibited a peak arising from the elimination of the high resistance of interparticle interfaces; the peak was absent in subsequent cycles. Plot of resistance with respect to temperature shows that resistivity of flashed rhenium is higher than literature values. The very rapid sintering and electroluminescence are attributed to the generation of defects in the form of vacancy-interstitial (Frenkel) pairs. The concentration of the Frenkels was estimated from in-situ calorimetry, where the difference between the electrical input energy and the enthalpy spent in black body radiation, convection and the energy stored as specific heat was ascribed to the endothermic reaction of defect generation; dividing by enthalpy of formation of the defects yielded concentrations of up to 14 mol % of Frenkels.

---

<sup>2</sup> This work has been submitted to the International Journal of Refractory and Hard Materials. The manuscript was directed by Prof Rishi Raj. The abstract is available on SSRN and is also available for download on SSRN.

## 6.2. Introduction

Flash sintering of ceramics was first reported in 2010<sup>13</sup>, but its application to metals has remained unexplored. Various classes of ceramics, ranging from ionic conductors and semiconductors to ferroelectrics and insulators, have been processed using flash sintering approach<sup>94</sup>.

Recent studies in our lab has shown tungsten, a highly refractory metal, can be “flash sintered” within seconds at a temperature of 1000°C<sup>95</sup>. Unlike ceramics, which typically require furnace heating, metals can be sintered at ambient conditions. This is achieved by directly injecting current into the specimens and continuously increasing it until sintering occurs.

The flash sintering method of processing metals through current rate shares similarities with electro-discharge-sintering<sup>80</sup>. In the latter, a significant amount of energy is stored in a capacitor and is rapidly discharged into a powder-pressed metal sample, causing it to sinter. The flash sintering approach, however, offers better control: the duration of sintering can be varied from a few seconds to several minutes by adjusting the current rate. The flexibility allows for continuous, in-operando measurements of various parameters, including temperature, electroluminescence, and resistivity, offering a deeper understanding of the role of these parameters and defects in the process.

The findings in present flash sintering of rhenium, another refractory metal. Like tungsten, Re is shown to be successfully flash sintered. Dogbone shaped specimens pressed from powders are sintered by direct injection of current, without the use of a furnace. Sintering occurs when the current density reaches 24 A mm<sup>-2</sup> and specimen reaches 900°C. Full density, greater than 98% is achieved. The specimen luminesces brightly during the flash experiment starting at a current density of 5.2 A/mm<sup>-2</sup>.

The very low temperature and the ultrafast rate of sintering are remarkably different from conventional sintering of Re where several hours at 2386°C. The mechanism of ultrafast sintering with electrical currents is apparently radically different. It is increasingly apparent that colossal generation of defects,

most likely vacancy-interstitial pairs are the underlying cause of flash sintering. Sintering is related to the rate of mass transport by diffusion. Since the diffusion coefficient is the product of defect concentration and the mobility of atoms, such a large increase in defects may indeed cause a very high rate of diffusion.

We report calorimetric measurements of the endothermic enthalpy during the flash process, which is ascribed to defect generation. It is obtained from the difference between the input electrical energy and the energy lost to black body radiation (BBR), convection and specific heat. When divided by the enthalpy of formation of Frenkel defects we obtain their concentration to be equal to  $\sim 14$  mol %, which is several orders of magnitude higher than the concentration expected from thermal equilibrium.

The results of current rate flash sintering of Re and other metals may have application in additive manufacturing. In conventional AM a part is built up digitally and then, separately, sintered. With current rate flash sintering it may be possible to build workpieces by integrating current rate sintering with conventional AM, thereby creating end-user ready parts.

Flash sintering is a highly energy efficient process since energy is directly injected into the workpiece to produce sintering without the use of large furnaces that must operate at very high temperatures for many hours where much of the heat is wasted.

### **6.3. Methods**

Rhenium powders with a purity of 99.99% and a particle size of -325 mesh, supplied by Fisher, served as the primary material for this study. We used less than 1g of this rhenium powder, without binders, and compacted it in a dogbone-shaped die using a hydraulic press from Dake Corporation, achieving a pressure of 140 MPa. The resulting specimen measures 16mm x 3.12mm x 0.44mm (gage length x width x thickness). Using the Archimedes method, we determined the green density,  $\rho_g$  to be  $\sim 74\%$ .

For direct-current injection, we used a Hewlett Packard 6261B power supply (0-20V, 0-50A output capacity). Tungsten electrodes, 1mm in diameter, were attached through the 1.1mm diameter holes located at the dogbone specimen's ears. We continuously injected electric current into the specimen at a rate of 1 A/s using a method adapted from Kumar et al.<sup>54</sup> A self-authored software interfaced to the hardware with a National Instrument data acquisition device (NI DAQ) was used to acquire voltage, temperature and time data. All experiments were conducted at room temperature inside an argon-filled glovebox made by Vacuum Atmosphere Company, USA. The argon gas, boasting 99.9% purity, was provided by Airgas, USA, and maintained an oxygen level between 5 and 14 ppm within the glovebox.

Electrical measurements involved injecting the current from the power source to the specimen while monitoring the voltage through a Keithley digital multimeter connected via a four-probe setup. With a voltage probe distance of 6.9 mm, the specimen's resistance (in  $\Omega$ ) was determined as the voltage-to-current ratio. Subsequently, resistivity (in  $\Omega \cdot \text{cm}$ ) was derived by scaling the resistance with the specimen's cross-sectional area and adjusting for probe distance. The experiment's layout is depicted in Figure 6-1.

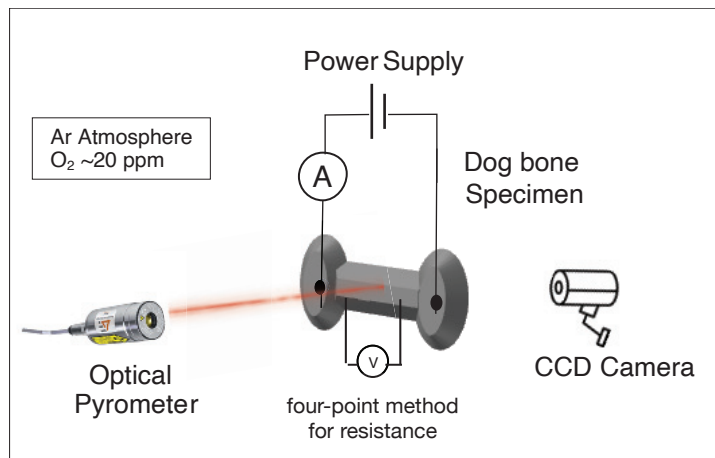


Figure 6-1: Illustration of flash sintering of metals without a furnace

We monitored the specimen in real-time using a CCD camera from Imaging Source (Germany) set to capture at 10 frames per second. Concurrently, temperature readings were taken with a CLTM-1HCF4-C3 pyrometer, manufactured by Micro-Epsilon (USA). This pyrometer operates within a temperature range of 250°C to 1200°C. Emissivity was configured at 0.3<sup>96</sup>, incorporating an error margin of 5% to account for possible emissivity fluctuations, notably shifting values between 0.24 to 0.28 at elevated temperatures<sup>97</sup>.

## 6.4. Results

### 6.4.1. Sintering

Sintering was conducted at a current rate of 1 A/s. The corresponding shrinkage curve is presented in Figure 6-2. The duration required for full sintering was 34 s. The sintered density can be calculated from the formula  $\rho_g = \rho \exp(3\epsilon_1)$ <sup>98</sup>. Here,  $\rho_g$  stands for the initial (green) density,  $\rho$  represents the concluding density, and  $\epsilon_1$  denotes the linear shrinkage strain (as recorded). Therefore, with a shrinkage strain of 0.091 and an initial density of 74%, the resulting density surpasses 97%. This value agrees with values obtained from Archimedes density measurement where 97.69% of theoretical density of rhenium was obtained.

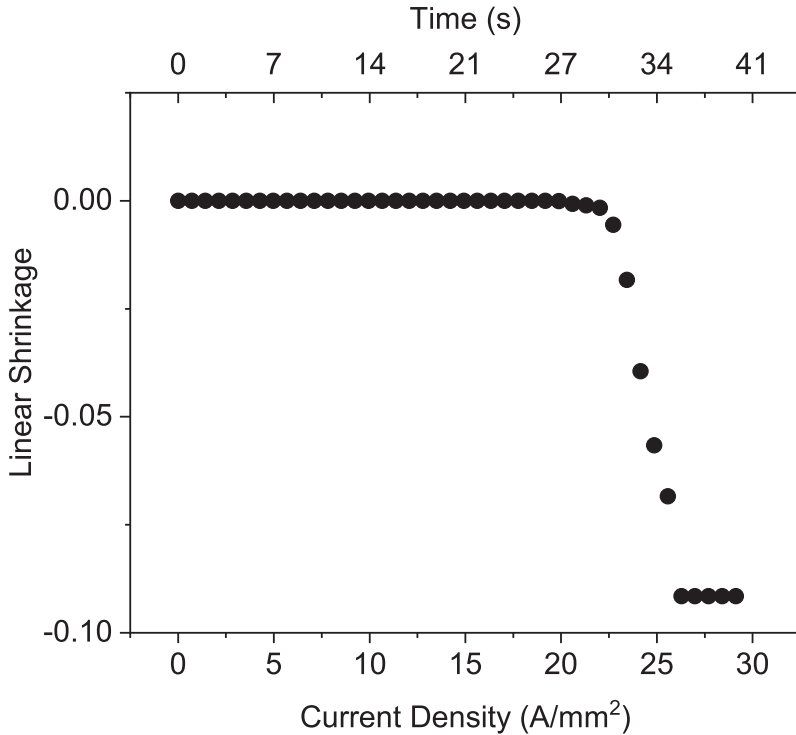


Figure 6-2: This figure depicts the linear shrinkage as recorded by a CCD Camera across three current rates. The visual data from the video was processed and analyzed using Fiji software to determine the shrinkage. Linear shrinkage is plotted against current density and time, providing insight into the rate of compaction over the given durations and role of current density in the sintering process.

#### 6.4.2. Three Cycles

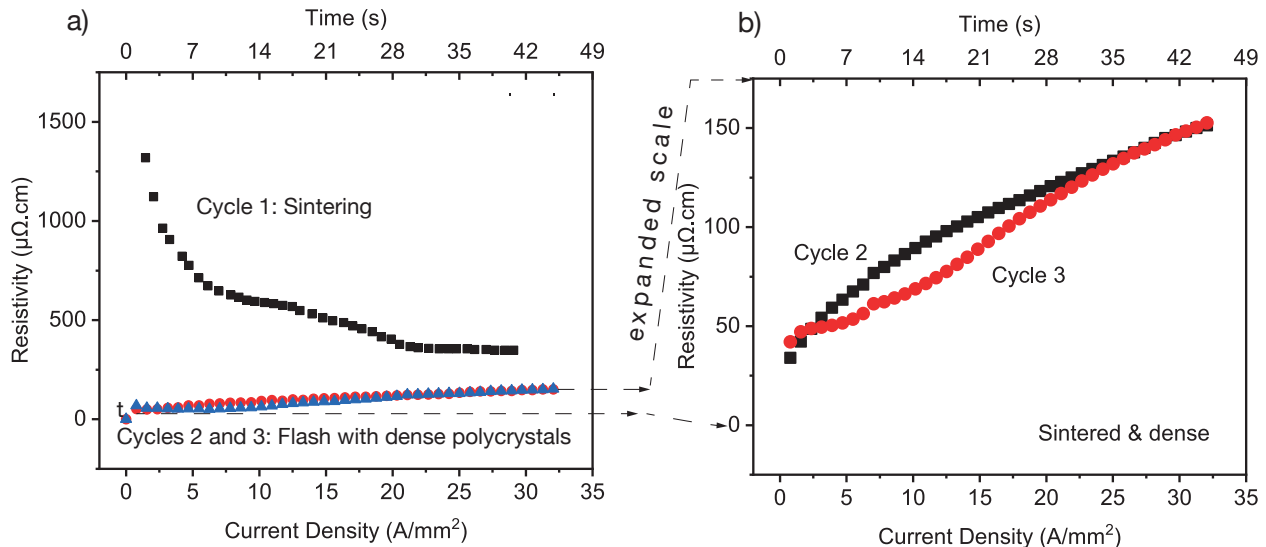


Figure 6-3: The change in resistance with current density. The first cycle refers to the sintering of the powder pressed sample. Cycles 2 and 3 were repeated on this sintered specimen. Sintering

lowers the resistance and gives reproducible results. Note the expanded resistivity scale on the right.

The change in resistivity with current density is plotted in Figure 6-3. The experiment was carried out with three cycles, with the same specimen. The first cycle represents sintering of the powder-pressed dog-bone specimen. After this cycle the specimen has sintered. The following two cycles were carried out on this sintered specimen. Note that the transient peak in the resistance in the first cycle is absent in later cycles. It is attributed to the breakdown of the oxide-layer on the powder particles. A similar phenomenon was seen experiments with aluminum powders<sup>89</sup>." The continued reduction in resistance is ascribed to sintering of pores.

#### 6.4.3. Temperature and Luminescence

The change in temperature and the progression of electroluminescence with the current density, measured during cycle 2 are shown in Figure 6-4. The temperature was measured with the pyrometer and the luminescence with the spectrometer (in the same experiment).

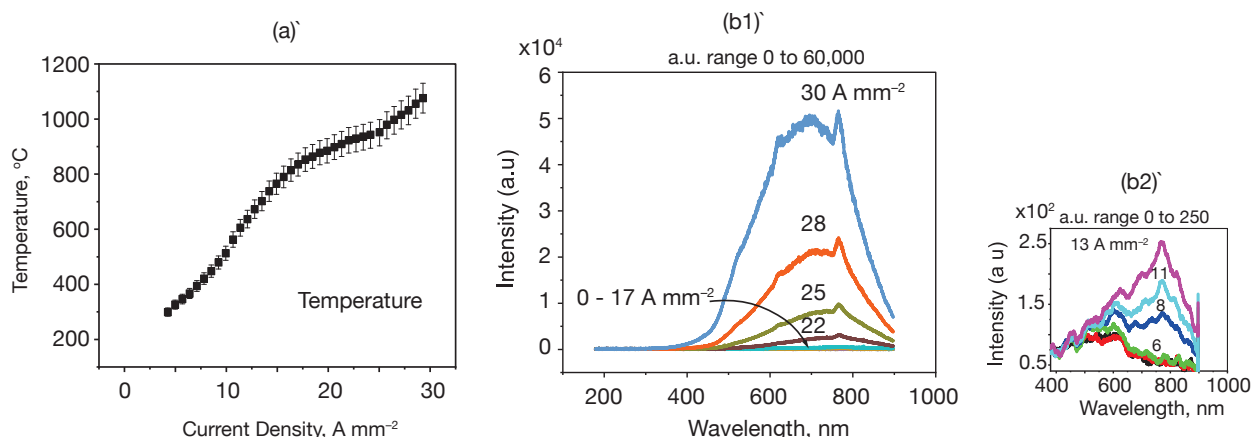


Figure 6-4: The change in the specimen temperature with current density, (a) and with it the intensity of optical emission, (b). Figure (b) is shown with a wide range of intensity units at high current densities ( $22 - 30 \text{ A mm}^{-2}$ ), and then with a high resolution scale which shows the emission at low current densities ( $6 - 13 \text{ A mm}^{-2}$ ).

The optical emission is attributed to electroluminescence, as opposed to black body radiation, for a couple of reasons: (i) the temperatures measured are too low for optical emission from Joule heating, and (ii) the emission peak's intensity increases with rising specimen temperature but its

position remains unchanged with respect to wavelength. In black body radiation the emission peak shifts towards shorter wavelengths as temperature rises.

#### 6.4.4. Resistivity

The in-operando resistance was measured using the four-point technique, detailed in Section 2. The measurement from cycle 2 is compared with the literature values obtained for temperature-dependent resistivity of rhenium, which are represented in black in Figure 6-5<sup>99</sup>.

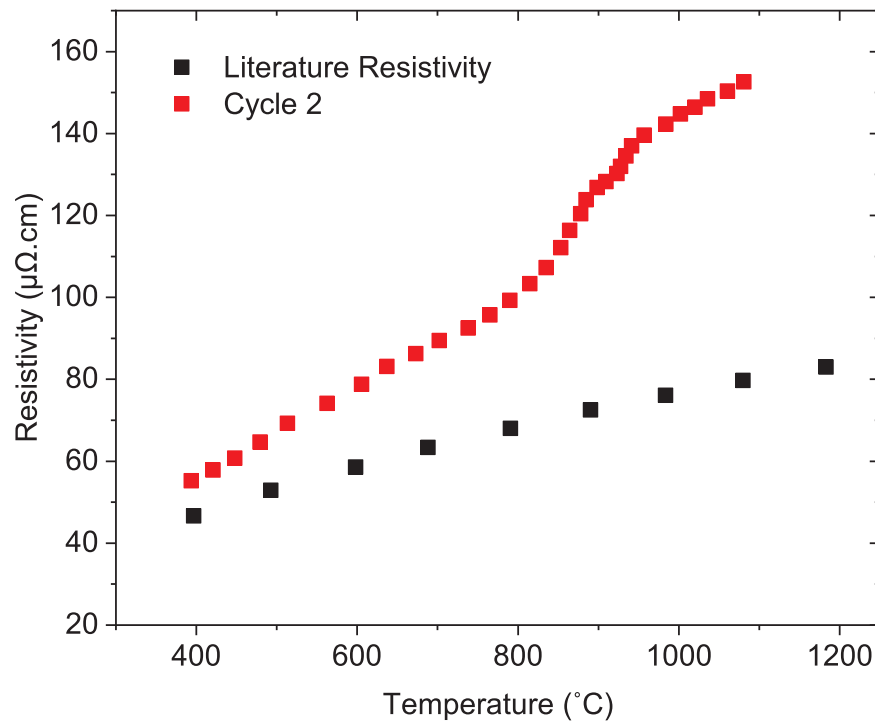


Figure 6-5: Resistivity behavior during cycle 2 flash compared with literature resistivity of rhenium.

The resistivity data from the flash experiment are higher than the data from the literature. This difference is residual defects that are generated with increasing current density. The effect is stronger at higher temperature which further supports this interpretation. It also seems that the defects recombine, at least to a great extent, when the current is turned off; thus the starting resistance in Figure 6-5 which represents the resistance at the end of Cycle 1 is low.

#### 6.4.5. Energy Deficit Analysis

A consistent observation in flash experiments is the presence of a deficit between the input electrical energy and the energy calculated from losses attributed to radiation, convection, and specific heat considerations. This disparity, known as the "energy deficit," provides a valuable method for determining endothermic defect concentrations. This can be accomplished by dividing the energy deficit by the defect formation enthalpy<sup>100</sup>.

The energy deficit, denoted as  $\Delta H^*(t)$  in Joules, can be represented through the following expression:

$$\Delta H^*(t) = \int_0^t (W(t) - W^*(t)) dt \quad (1)$$

where  $W(t)$  signifies the electrical energy (measured in Watts) introduced to the specimen, while  $W^*(t)$  captures the energy dissipated through radiation, convection, and specific heat. The direct input of electrical energy was calculated by multiplying the injected current with its corresponding voltage. On the other hand, the energy losses attributed to radiation, convection, and specific heat are derived using the following expressions<sup>54</sup>:

$$W^*(t) = W_{BBR}^*(t) + W_{conv}^*(t) + W_{spht}^*(t) \quad (2)$$

$$W_{BBR}^*(t) = \epsilon_m S \sigma (T_K^4 - 298^4), \quad (3)$$

$$W_{conv}^*(t) = h S (T_K - 298), \quad (4)$$

$$W_{spht}^*(t) = m C_p \frac{dT_K}{dt} \quad (5)$$

Eqns. (3 to 5) are in units of Watts, or J s<sup>-1</sup>. In this context,  $S$  denotes the specimen's surface area,  $\epsilon_m$  refers to rhenium's emissivity (valued at 0.3), and  $\sigma$  represents Stefan-Boltzmann's constant ( $5.6704 \times 10^{-8}$  W/m<sup>2</sup>·K). The ambient temperature, 298 K, is used since the procedure was

executed without furnace. The symbol “ $m$ ” indicates the specimen's mass (valued at 0.00035 kg), and the specific heat,  $C_p$ , equals 137 J/kgK.  $T_K$  represents the specimen temperature in Kelvin, measured using the pyrometer. Implementing Eqns. (2) and (3, 4 and 5) into Eqn. (1) provides an approximation of the energy deficit in Joules after the right-hand component in Eqn. (2) undergoes time integration.

The convective heat transfer coefficient,  $h$ , in Eqn. (4) demands further attention. Its value in air oscillates between 10 to 100 W m<sup>-2</sup> K<sup>-1</sup>, contingent upon factors such as surface chemistry and morphology, gas velocity at the interface, and the gas's heat-carrying ability, which is influenced by its pressure and specific heat. For instance, Argon possesses a significantly reduced heat capacity compared to Nitrogen. Consequently, in Argon-based tests (like the current ones), the heat transfer coefficient will be less than in air.

Convection-driven losses progress linearly with temperature  $T$ , while BBR losses amplify with  $T^4$ . This means convection is higher at lower temperatures but gives way to BBR as temperatures rise. The commonly accepted cross-over temperature, where energy loss transitions from convection to BBR, is approximately 600°C. This point is typically when the emitted light exhibits a faint red hue. A corresponding graph using our data is presented in Figure 6-6, which pinpoints the transition near 600°C when  $h$  equals 15 W m<sup>-2</sup> K<sup>-1</sup>.

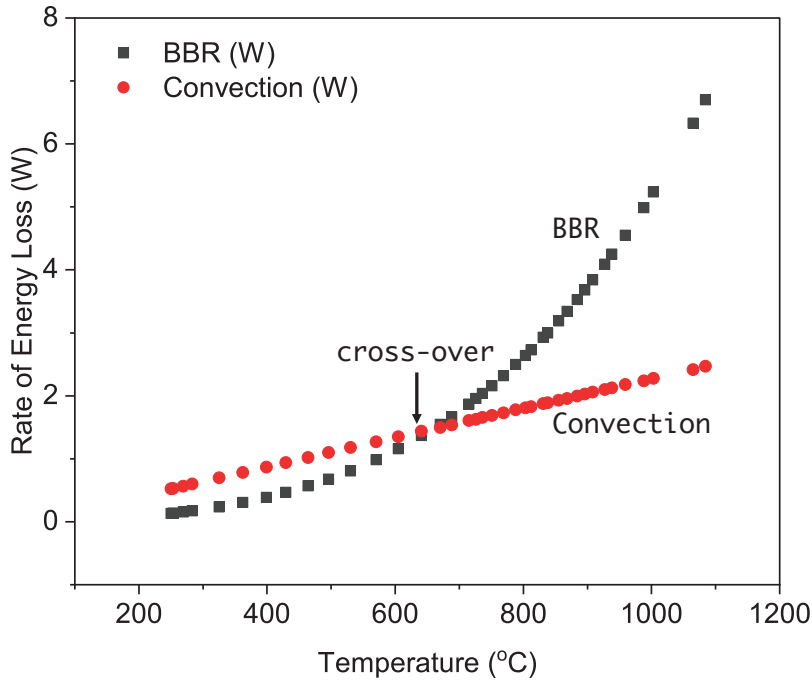


Figure 6-6: A plot of BBR loss and Convective loss assuming  $h = 15 \text{ Wm}^{-2}\text{K}^{-1}$

To continue, it's crucial to express  $\Delta H^*$  from Eqn. (3) in molar terms. This conversion begins by determining the number of rhenium moles present in the specimen, expressed as:

$$N_W = \frac{V_{\text{specimen}}}{V_{\text{molar}}} \quad (6)$$

Thus, to express the enthalpy from Eqn. (3) in molar terms, we use:

$$\Delta H_{\text{mol}}^* = \frac{\Delta H^*}{N_W} \quad (7)$$

To calculate the mole fraction of defects generated in the specimen, the enthalpy in molar terms (from Eqn. (7)) is divided by the formation energy of the defects, resulting in:

$$x_F = \frac{1}{E_F N_W} \frac{\Delta H^*}{\Delta H_{\text{mol}}^*} \quad (8)$$

Here,  $E_F$  signifies the formation energy of Frenkel defects, expressed in Joules mol<sup>-1</sup>.

When integrating the given values,  $V_{specimen} = 22.5 \times 10^{-3} \text{ cm}^3$ ,  $V_{molar} = 8.67 \text{ cm}^3 \text{ mol}^{-1}$ , and  $E_F = 11.96 \text{ eV}$  (representing the energy required for Frenkel pair formation in Re as obtained from embedded atom potential in molecular dynamics simulation<sup>101</sup>) into our equations, we first need to convert  $E_F$  from eV to J mol<sup>-1</sup>. This is achieved by multiplying the eV values by 96,500. Implementing these equations produces the outcomes presented in Table I.

1. The input data is the temperature and electrical power input as a function of time.
2. The left-hand side of Eqn. (6-5 to 6-7) are obtained by inserting the temperature data into the right-hand side.
3. The watt measurements are converted to Joules through time integration.
4. Energy loss is calculated by combining BBR, convection and specific heat data.
5. The total energy loss subtracted from the input energy gives the magnitude for  $\Delta H^*$ .
6. Next Eqn. (8) gives the mole fraction of Frenkel defects. They are given in the right hand most column in Table I.

Table IV: Frenkel Defect Analysis Based on Energy Deficit

Time	Pyrometer Temp	Power Input	BBR	BBR	Convec	Convec	Spec Heat	Total IN	Total LOSS	Deficit	Frenkel
sec	°C		W	J	W	J	J	J	J	kJ/mol	mol fraction
10	399	3.21	0.39	0.39	0.65	4.61	1.77	14.16	6.78	7.38	0.002
11	429	3.88	0.47	0.47	0.71	5.32	1.44	18.04	7.22	10.82	0.004
12	464	4.61	0.57	0.57	0.77	6.09	1.68	22.65	8.33	14.32	0.005
13	496	5.24	0.68	0.68	0.82	6.91	1.53	27.89	9.12	18.77	0.006
14	530	6.12	0.81	0.81	0.88	7.79	1.63	34.01	10.23	23.78	0.008
15	570	7.04	0.98	0.98	0.95	8.74	1.92	41.04	11.65	29.40	0.010
16	605	7.94	1.16	1.16	1.01	9.76	1.68	48.98	12.60	36.38	0.012
17	641	8.38	1.37	1.37	1.08	10.83	1.73	57.36	13.93	43.43	0.014

18	670	9.20	1.55	1.55	1.13	11.96	1.39	66.56	14.90	51.66	0.017
19	688	9.80	1.67	1.67	1.16	13.12	0.86	76.36	15.66	60.71	0.020
20	715	10.38	1.87	1.87	1.21	14.33	1.29	86.74	17.49	69.25	0.023
21	726	10.94	1.96	1.96	1.22	15.55	0.53	97.68	18.04	79.65	0.027
22	736	11.86	2.04	2.04	1.24	16.79	0.48	109.54	19.31	90.23	0.030
23	751	12.58	2.16	2.16	1.27	18.06	0.72	122.12	20.94	101.18	0.034
24	769	13.15	2.32	2.32	1.30	19.36	0.86	135.27	22.54	112.73	0.038
25	788	14.08	2.50	2.50	1.33	20.69	0.91	149.35	24.10	125.25	0.042
26	803	14.90	2.64	2.64	1.36	22.05	0.72	164.25	25.41	138.84	0.046
27	812	15.44	2.73	2.73	1.38	23.43	0.43	179.69	26.59	153.10	0.051
28	831	15.01	2.93	2.93	1.41	24.84	0.91	194.70	28.68	166.02	0.055
29	838	15.72	3.00	3.00	1.42	26.26	0.34	210.42	29.60	180.82	0.060
30	855	16.41	3.19	3.19	1.45	27.71	0.82	226.83	31.71	195.11	0.065
31	868	17.05	3.34	3.34	1.47	29.18	0.62	243.88	33.15	210.73	0.070
32	884	17.92	3.53	3.53	1.50	30.68	0.77	261.80	34.98	226.81	0.076
33	896	18.81	3.68	3.68	1.52	32.20	0.58	280.61	36.46	244.15	0.081
34	908	19.72	3.84	3.84	1.54	33.75	0.58	300.33	38.16	262.17	0.087
35	927	22.05	4.09	4.09	1.58	35.32	0.91	322.38	40.33	282.05	0.094
36	938	24.48	4.25	4.25	1.60	36.92	0.53	346.86	41.69	305.17	0.102
37	959	26.27	4.55	4.55	1.63	38.55	1.01	373.13	44.10	329.02	0.110
38	988	26.22	4.99	4.99	1.68	40.23	1.39	399.35	46.62	352.73	0.118
39	1003	26.52	5.24	5.24	1.71	41.94	0.72	425.87	47.90	377.97	0.126
40	1065	28.00	6.33	6.33	1.82	43.76	2.97	453.87	53.06	400.80	0.134
41	1084	29.93	6.70	6.70	1.85	45.61	0.91	483.80	53.22	430.58	0.144

Plots illustrating the energy deficit in kJ mol<sup>-1</sup> and the corresponding mole fraction of Frenkel pairs are depicted in Figure 6-7 (a)&(b). The findings obtained from the data shows the defect concentration rising to 14% mole fraction. Comparatively, values from thermal equilibrium are significantly lower, spanning many orders of magnitude. We've revisited our experiments and calculations to ensure their accuracy. Moreover, defect generation in rhenium appears distinct to that in tungsten. As detailed in section 5.0 on flash sintering of tungsten and section 7.0 on nickel, we've recorded a mole fraction of 0.3% for nickel, and 26% for tungsten.

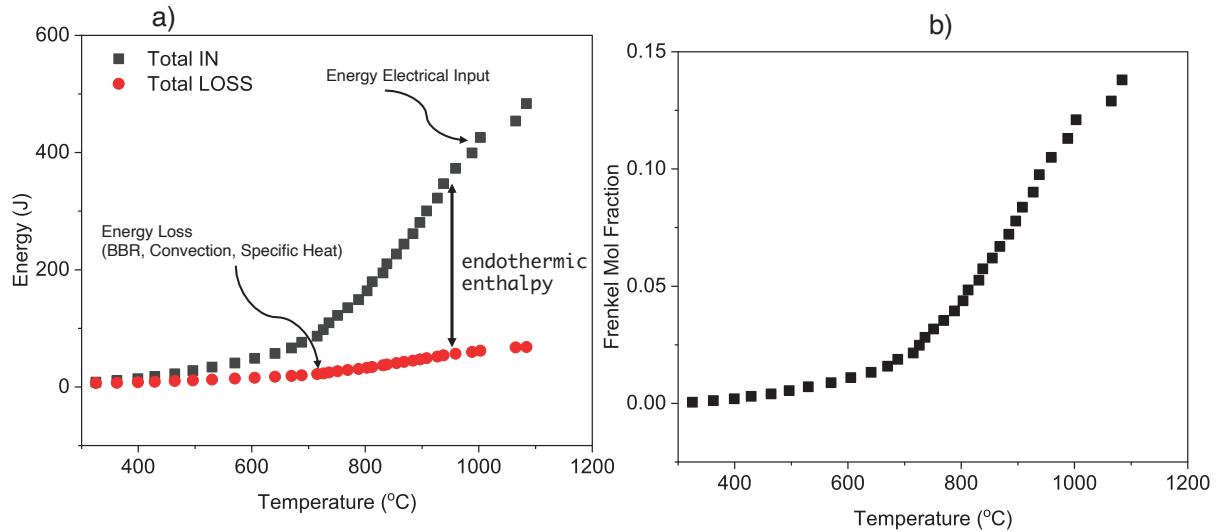


Figure 6-7: (a) Plots of the energy deficit, and (b) the corresponding concentration (in units of mol %) calculated from the endothermic enthalpy divided by the energy of formation of Frenkel pairs. The pattern of flash sintering observed in the present study is similar to tungsten (unpublished). A common observation is that resistance is higher than the literature values, pointing to the role of defects. The three regimes of behavior in current rate flash sintering of metals are shown in Figure 6-8. The pattern starts with incubation, followed by the onset of electroluminescence, and finally by sintering. Similar behavior was observed in W and Ni in section 7.0.

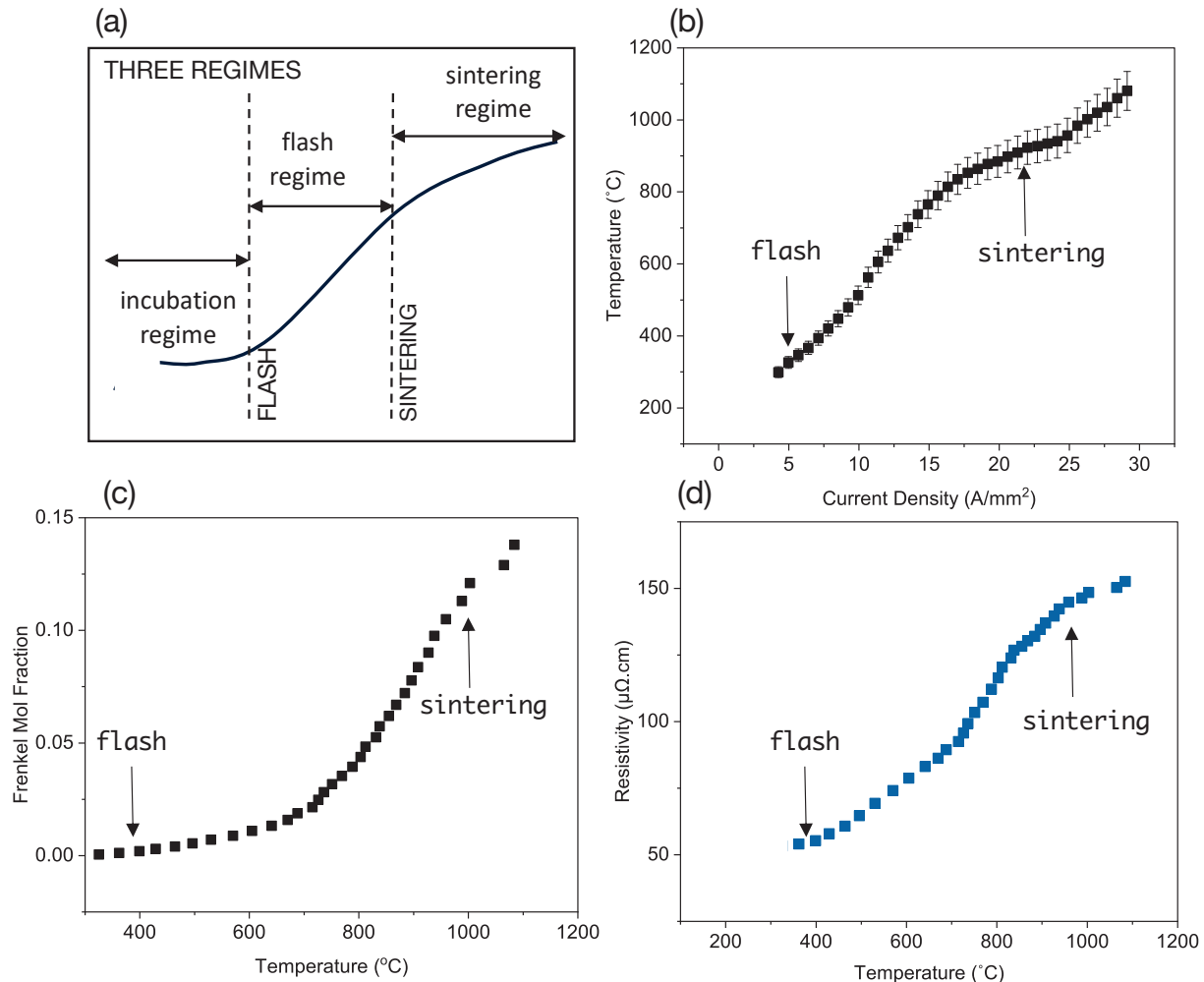


Figure 6-8: (a) The three regimes depicting the phenomenological behavior in flash sintering of metals; the transitions are prescribed by three regimes: the incubation regime, followed by the flash regime, followed by the sintering to full density. The measurement of (b) temperature, (c) the estimate of defect generation, and (d) the resistivity, consistently show this three-regimes pattern.

## 6.5. Discussion

This is the second report on flash sintering of a refractory metal following the work on tungsten.

Both are refractory metals with melting points of 3182°C for Re and 3383°C for W. Solid state diffusion theories link the diffusion coefficient with the melting point of the metal<sup>102</sup>. Generally sintering occurs at 0.75T<sub>M</sub>, held for several hours. In comparison the current rate flash sintering occurs near 1000°C in about one minute. Both metals sintered at a current density of 20 – 24 A mm<sup>-2</sup> (for similar workpiece geometry). Apparently solid-state diffusion in flash is ultrafast.

The high diffusivity may be attributed to the concentration of defects described in the Section 6.4.5. Indeed, real-time measurements of diffusion coefficients across bilayers in ceramics suggest that diffusion rates in flash are almost  $10^8$  times faster<sup>103</sup>. The activation energy for diffusion are found to be one half to a third of the values in literature (also in experiments of superplastic deformation<sup>104</sup>)

Recently the superposition of magnetic fields has been shown to drive the flash into a standalone workpiece without electrical contacts. It is likely that flash is a solid-state plasma<sup>105</sup> which responds to magnetic fields.

It is becoming increasingly evident that flash sintering has broad implications. For instance, rhenium, nickel and tungsten, despite considerably different melting points, show similar behavior for example the onset of luminescence at  $5\text{-}7 \text{ A mm}^{-2}$ , reaching full sintering between  $20\text{-}24 \text{ A mm}^{-2}$  (in specimens of similar geometry).

The current experiments on rhenium, inclusive of those on tungsten, were executed using direct current injection, eliminating the need for a furnace. However, a singular tungsten experiment employing furnace heating of the specimen during flash revealed that while the sintering temperature remained constant, the current density at which sintering occurred was lower. This was attributed to the furnace's surrounding warmth. This field of metallic flash sintering require further study.

## 6.6. Conclusion

Flash sintering of rhenium powders is a new paradigm for densification of refractory metals. The development has significance in additive manufacturing of metals, paving the way for in-situ densification while the workpiece is built up digitally.

The common behavior manifested by various materials under flash conditions suggests a far from equilibrium phenomenon. For example creation of novel phases that do not fit classical thermodynamic behavior have been reported<sup>106</sup>. Such findings hold the possibility of new solid-state electrolytes for Li<sup>+</sup> batteries, with high ionic conductivities<sup>107</sup>.

## 7.0. Current rate flash sintering of nickel at ambient temperature in < 1 minute<sup>3</sup>

### 7.1. Summary

We show that powder pressed specimens of nickel can be sintered to 99.96% density by injecting electrical current, without the use of a furnace. Full sintering was achieved in within 10 to 52s by changing the current rate from 5 A/s to 1 A/s. In all instances, the samples sintered abruptly at a current density of ~20 A mm<sup>-2</sup>. The grain size of the sintered samples was somewhat larger than the nickel powder particle size (~60 µm versus 40µm). Tensile testing yielded a yield strength of 98 MPa, ultimate tensile stress of 323 MPa and ductility of ~17%. Four in-operando measurements are reported: (i) sintering as a function of time, (ii) the change in resistance with current density, (iii) the temperature and (iv) electroluminescence. The change in resistance during flash sintering of the powder-pressed sample exhibited a high peak followed by a steep decline in resistance; the transient is attributed to the breakdown of particle-particle interface resistance. The same cycle repeated with the flash-sintered, dense sample, did not show the spike, and gave reproducible results for the resistivity. The resistance data when viewed as a function of temperature at first had a lower, and subsequently a higher resistance than the literature values. The difference reflects the influence of defects generated during flash on resistivity. We have also measured the endothermic enthalpy, expressed by the difference between the in-situ input electrical energy and the radiation and convection losses. Dividing by the formation energy of Frenkel pairs yields the concentration of defects; estimated to be 0.4 mol %. The present experiments may be equivalent to electro-discharge-sintering where a large amount of energy is dumped into a metal to produce sintering in a few milliseconds. Remarkably, the energy expended during this experiment was a mere 4.55

---

<sup>3</sup> This work has been submitted to the Journal of American Ceramic Society and is currently under consideration. This work has the input of Dr. Morsi Mohammed. This manuscript was directed by Prof Rishi Raj.

J/mm<sup>3</sup>, substantially lower than the 5-10 kW typical of traditional sintering and electric field-assisted techniques. The findings from this study make a case for the application of flash sintering technique to metal powder processing, offering speed, energy efficiency and simplicity of set up.

## 7.2. Introduction

While flash sintering of ceramics has received considerable attention since it was first discovered<sup>13</sup>, almost none has been given to the sintering of metals. It was shown that many ceramics, ionic conductors, semiconductors, ferroelectrics and insulators, could be sintered by flash<sup>94</sup>.

Recently we have shown that a highly refractory metal, tungsten, can be sintered in a few seconds at 1000 °C<sup>95</sup>. While ceramics required auxiliary heating with a furnace, metals were sintered at room temperature by injecting current directly into the dogbone specimens and increasing it at a constant rate until the specimen flashed and sintered.

The current rate flash sintering of metals bears similarity to electro-discharge-sintering<sup>80</sup> where a large amount of energy stored in a capacitor is dumped within a few milliseconds into a powder-pressed sample of a metal, causing it to sinter. The present experiments offer much greater control; the duration of the experiments can be stretched from a few seconds to several minutes by slowing down the current rate, which allows time for in-operando measurements of the flash behavior; we report continuous measurements of sintering, temperature, electroluminescence, and resistivity. These data provide insights into the role of defects in flash sintering of metals.

The flash sintering of metals is an important development in the science and technology of sintering. The simplicity of the point defects, vacancies, and interstitials, in metals may lead to an easier path for understanding the fundamental mechanism(s) of the flash phenomenon. The method

may also be developed for in-situ additive manufacturing of metals where digital build up can be integrated with flash sintering, thereby producing parts that are end-user ready.

Flash is immensely more energy efficient than conventional sintering. Instead of large inefficient furnaces, flash can be carried out within tabletop system with a small footprint. The injection of energy directly into the workpiece for sintering sidesteps the energy-wasting inefficiency of conventional sintering, possibly revolutionizing the way materials will be sintered in the future.

### 7.3. Methods

The flash-sintering experiments were carried out within a glove box ( $<100$  ppm O<sub>2</sub>), at room temperature, by injecting DC electrical current directly into dogbones, similar to recent experiments with tungsten. The current was raised at a constant rate until the workpiece sintered. The open nature of the experiment allowed full access to the specimen: with a camera to measure sintering, a pyrometer for temperature and a spectrometer to characterize the optical emission spectrum.

The dogbone specimens were pressed into shape from nickel powder, obtained from Alfa Aesar. They were specified to be 99.8% pure with an average particle size of 44 $\mu$ m. The die was filled with about 1.5 g of powder and pressed with 150 and 180 MPa, yielding specimens with a gage length of 20 mm, a width of 3.55 mm, and a thickness of 0.71 mm. The green density of these samples was 85-87%.

One millimeter holes were drilled into the ends of the dogbone specimen. Electrodes made from tungsten were inserted into them to supply electrical current, from a KEPCO KLN 30-100 power supply. Two more holes at the outer edges of the gage length, just inside from current carrying electrodes were drilled to measure the voltage. This voltage measurement, which does not draw any current, and the current injected from the power supply were used to measure the four-point resistance.

The unprocessed (green) state of the dogbone specimen is showcased in Figure 7-1a, while a schematic representation of the entire experimental setup can be seen in Figure 7-1b.

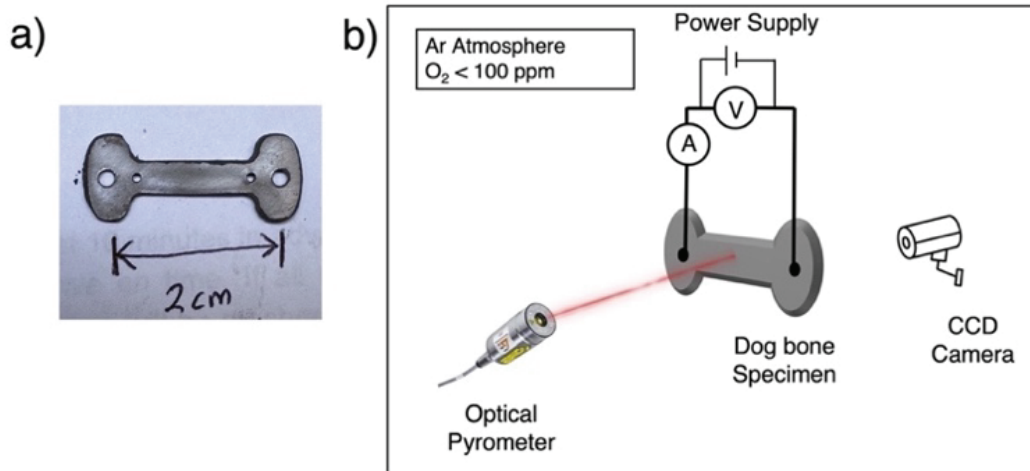


Figure 7-1: (a) As-pressed nickel specimen before flash sintering (b) Illustration of flash sintering setup for metals in an inert atmosphere of less than 100 ppm oxygen

The specimen temperature was measured with a CTLM-1HCF4-C3 pyrometer from Micro Epsilon (USA); the emissivity was set to  $0.12^{108}$ . The optical emission spectra were recorded with an Ocean Optics spectrometer (model USB4000-UV-VIS) which was connected to a Spectra Suite. The outputs from the power source (i.e. the current), the voltmeter, the pyrometer, the spectrometer, and the software for controlling the current rate were interfaced to a computer via a NI DAQ card. A video camera recorded images which were analyzed for shrinkage.

## 7.4. Results

### 7.4.1. Sintering

Sintering was carried out at three current rates: 1 A/s, 2 A/s and 5 A/s. The shrinkage curves are shown in Figure 7-2a. The samples sintered in 52 s, 26 s and 10 s respectively. The sintering data merged into a common curve when plotted against the instantaneous values of the current density, as shown in Figure 7-2b. Similar behavior was seen in flash sintering of W, and earlier in flash sintering of yttria stabilized zirconia<sup>54</sup>. Collectively these results prove that current density is the critical parameter that controls the shrinkage in flash experiments. The fundamental mechanism for this behavior is not understood, although these results resemble earlier experiments with a

ceramic, where it was shown that the extent of sintering was related simply to the current density limit placed on the power supply<sup>109</sup>.

The sintered density estimated from the equation  $\rho_g = \rho \exp(3\epsilon_1)^{98}$ , where  $\rho_g$  is the green density,  $\rho$  is the final density, and  $\epsilon_1$ , is the linear shrinkage strain (as measured). Thus, shrinkage strain of 0.045 and a green density of 86% yields >99% for the final density. Archimedes measurements yielded 99.6% relative density.

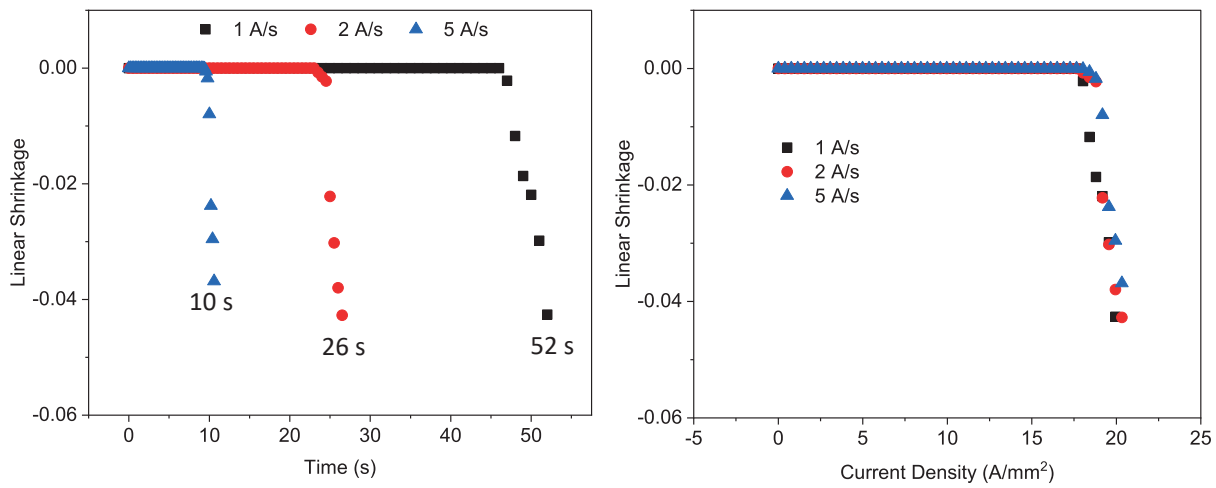


Figure 7-2: Linear shrinkage measured from the video captured using a CCD Camera. The insitu video captured at all rates were analyzed for shrinkage using Fiji software.

#### 7.4.2. Resistivity during flash

Resistivity was determined based on the injected current, voltage measured using the four-point method, and specimen dimensions. The resistance measured as a function of the current density is shown in Figure 7-3. The measurements were made in three cycles. In the first cycle the specimen was the initial powder pressed dog-bone. During the second and third cycles the sample that had been sintered to full density during the first cycle was subjected again to two more flash cycles. These latter cycles show the influence of the flash effect on the resistance of a dense sample: the resistance is low at first but then rises to catch up with the resistance measured during the first cycle.

The peak in the transient in the first cycle was also seen in tungsten. Even earlier it had been observed in field assisted experiments with aluminum powders<sup>89</sup> - although those experiments were not ascribed to “flash”. The transient is attributed to the breakdown of the surface oxide on the powder particles leading to an abrupt drop in the contact resistance at particle interfaces. Further decline in resistance most likely arises from the removal of the pores by sintering.

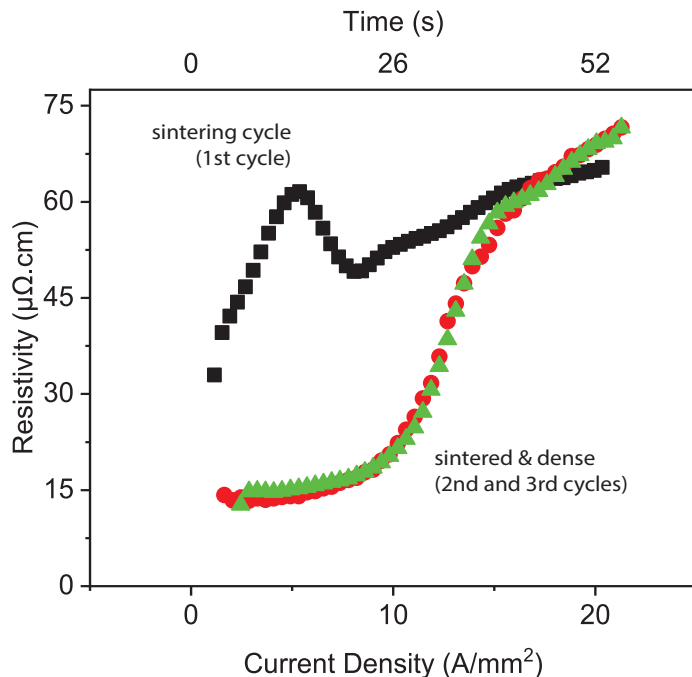


Figure 7-3: Resistivity curve of nickel as a function of current density and time during the flash sintering of green specimen (black). The other two data sets were obtained by re-flashing the specimen after the first cycle. The first cycle data are for powder specimen (black) and the latter two for dense sample (red and green).

#### 7.4.3. Temperature and Electroluminescence

The temperature of the specimen measured with a pyrometer, as well as the luminescence spectrum are shown in Figure 7-4(a) and (b).

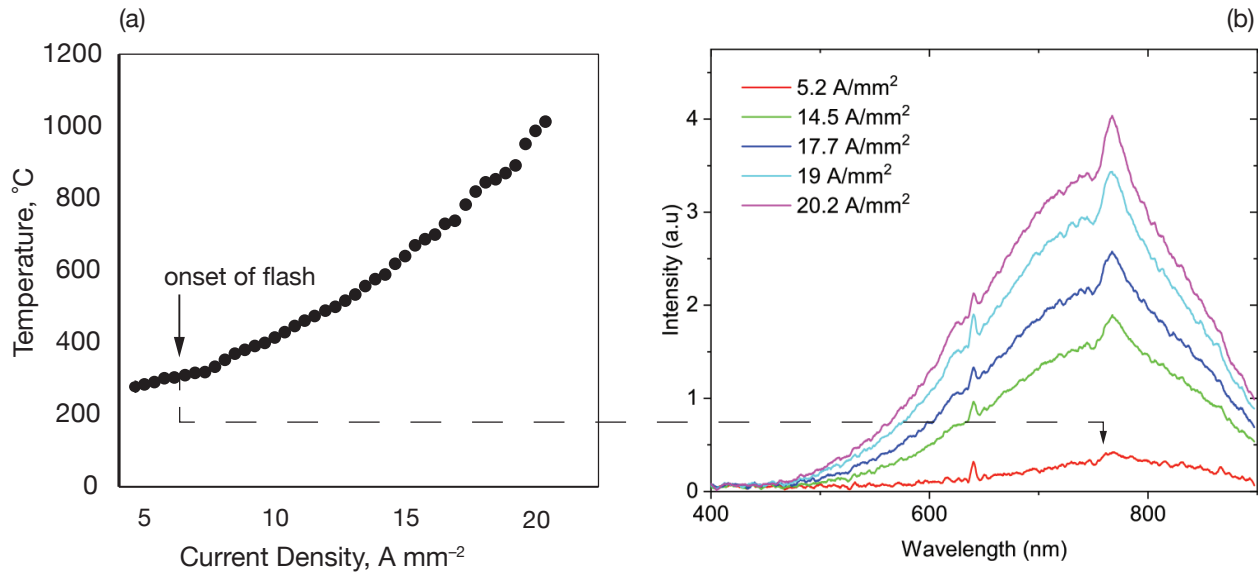


Figure 7-4: (a) Measurement of the specimen temperature as a function of the current density. (b) The luminescence spectra at different current densities. The emission is ascribed to electroluminescence.

Electroluminescence, a frequently observed phenomenon during flash sintering in ceramics, acts as an evident marker of defect generation during the flash sintering process. Notably, this characteristic luminescence was evident during the flash sintering of nickel as reported in Figure 7-4b. Here, the onset of electroluminescence prominently demarcated the transition from the incubation phase to the actual flash regime, a transition that occurred at an intensity of 5.2 A/mm<sup>2</sup>.

The luminescence is ascribed to electroluminescence, rather than to black body radiation (BBR), for two reasons. (i) The temperatures are too low for strong optical emission just from Joule heating, and (ii) The emission peak increases in intensity but remains at the same position when the specimen temperature increases. In BBR the emission peak moves to shorter wavelengths as temperature rises.

Curiously the emission spectra are similar to the emission from ceramics<sup>110</sup>. It is likely that the flash induced plasma ionizes the atmospheric gas, which dominates the emission spectrum.

#### 7.4.4. Resistivity Comparison for Insitu flash, post flash and handbook reference.

The in-operando resistance was measured by the four-point method as described in Section 7.4.2.

These measurements are compared with the literature values of the temperature dependent resistivity of nickel (shown in green)<sup>111</sup>. Furthermore, the flashed specimen was heated with a furnace (without electrical current) and the resistance measured as a function of the furnace temperature (shown in red). Figure 7-5 compares the in-operando resistivity with literature and the furnace measurements.

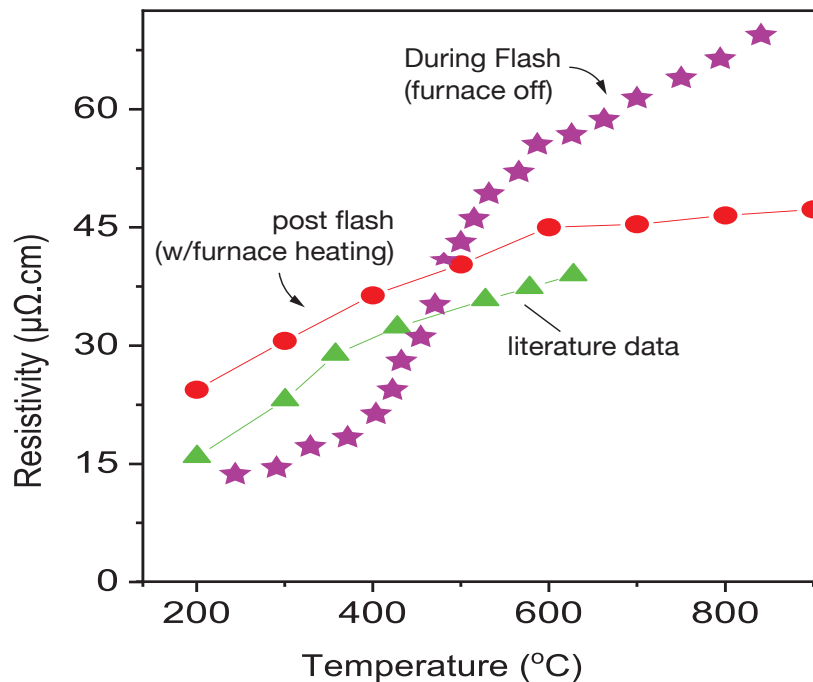


Figure 7-5: Resistivity behavior during flash, and with furnace heating of the flash sintered specimen. The temperature dependent resistivity data from literature are shown in green color.

The following features of Figure 7-5 are notable:

1. The resistivity data of flashed samples is comparable to the literature data. The magnitude is a bit higher (which can be ascribed to residual defects left behind after the flash experiment), but the trend is consistent.
2. The data obtained during the flash cycle is remarkably different from post flash behavior, which reflects the influence of the defects generated during flash. Presumably majority of

the defects are removed by recombination when the current is turned off. The electroluminescence spectra given in Figure 7-4 also reflect the infusion of electrons and holes, which recombine to produce photons. This generation of electronic defects presumably lowers the resistivity. Eventually the resistance begins to rise again, presumably when the defect concentration has reached a “saturation” limit.

#### 7.4.5. Energy Deficit

Current rate flash experiments with ceramics have consistently shown that the energy lost to For radiation and stored as specific heat falls short of the input electrical energy. The difference is attributed to the endothermic generation of point defects, e.g. Frenkel pairs. Here we apply the same methodology to current rate sintering experiments with nickel, estimating the defects to be approximately 0.3% mol fraction.

To perform this analysis, We write the equation for the energy deficit,  $\Delta H^*(t)$ , in Joules, as:

$$\Delta H^*(t) = \int_0^t (W(t) - W^*(t)) dt \quad 7-1$$

where  $W(t)$  is the electrical work expended (in Watts) into the sample, and  $W^*(t)$  is the energy lost to radiation, convection, and specific heat.

$$W^*(t) = \epsilon_m S \sigma \left( [T^P_K]^4 - T^4_F \right) + hS(T^P_K - T_F) + mC_p \frac{dT^p}{dt} \quad 7-2$$

The first term represents black body radiation, the second term represents the energy loss to convection, and the last one is the energy absorbed in specific heat.

The mole fraction of defects is then obtained from the total moles of Ni,  $N_W$ , in the specimen,

$$N_W = \frac{V_{specimen}}{V_{molar}} \quad 7-3$$

which leads to the following expression for the mole fraction of defects,  $x_F$ , assumed here to be Frenkels (vacancy-interstitial pairs)

$$x_F = \frac{1}{N_W} \frac{\Delta H^*}{E_F} \quad 7-4$$

The parameters for calculating  $x_F$  are given in Table 7-1:

Table 7-1: The parameters used to estimate the energy deficit in Eq. (7-1).

Parameters	Symbol	Values	Units
Stefan-Boltzmann Constant	$\sigma$	5.67x10^-8	W m^-2 K^-4
Emissivity	$\epsilon_m$	0.12	
Specimen Volume	$V_{specimen}$	52.128	mm^3
Surface Area	$S$	173.6	mm^2
Molar Volume	$V_{molar}$	0.6596	cm^3/mol
Initial Temperature ( $T_F$ )	$T_F$	298	K
Specimen mass	$m$	0.0004	kg
Specific Heat	$C_p$	445	J/ kg.K
Formation energy	$E_F$	5.48 523	eV kJ mol^-1
Heat transfer coefficient	$h$	7*	W/m^2K

---

\*The heat transfer coefficient was estimated by comparing convective losses according to Eq. (7-4) with the BBR losses from Eq. (3), using the criterion that BBR losses dominate at temperatures above ~600 °C (mild red optical emission). The usual value for  $h$ , for convective losses in air is in the 5 to 100 W m^-2 K^-1. However, Argon used in the current experiment has a much lower heat capacity than nitrogen, and therefore  $h$  may be lower for the present experiments. A good fit to the transition was obtained for  $h = 7 \text{ W m}^{-2}\text{K}^{-1}$ , as shown in Figure 7-6. (The literature values for  $h$  for Ni<sup>112</sup> range from 5 to 10 W m^-2K^-1).

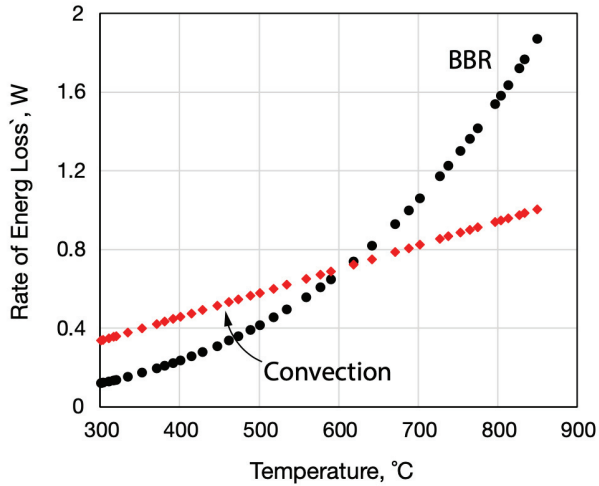


Figure 7-6: A plot for the BBR loss and the convective loss assuming  $h = 7 \text{ W m}^{-2} \text{ K}^{-1}$ . The data for the energy deficit and the estimated concentration corresponding to the endothermic energy deficit is plotted in Figure 7-7.

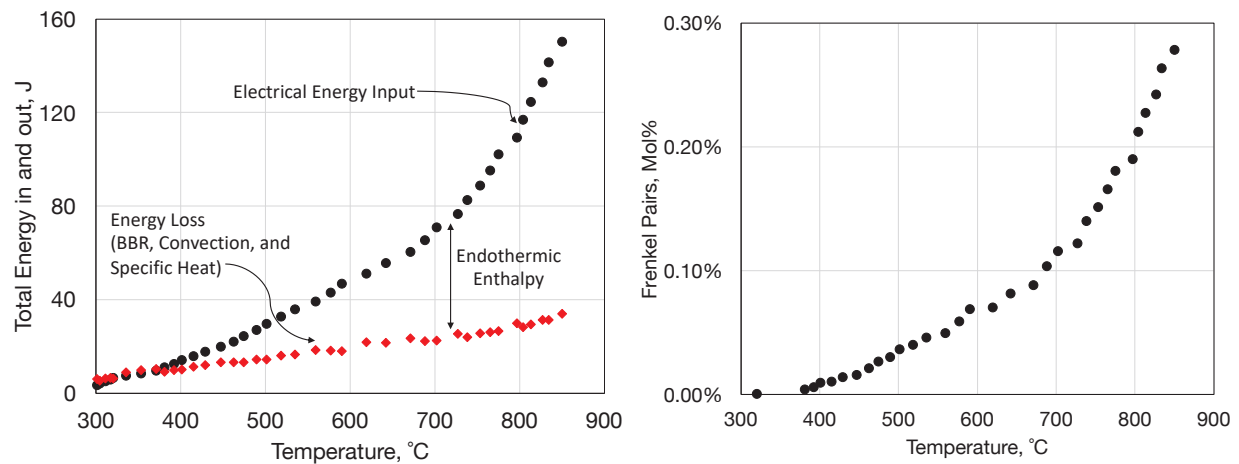


Figure 7-7: (a) Plots of the energy deficit, and (b) the corresponding concentration (in units of mol %) calculated from the endothermic enthalpy divided by the energy of Formation of Frenkel pairs. The slight step in the Frenkels in Figure 7-7(b) most likely arises at the onset of flash. Note the very high values for the mol% of Frenkels generated from the endothermic nature of the flash experiments. It reaches up to 0.26 % or a mole fraction of  $2.6 \times 10^{-3}$ . These numbers are many orders of magnitude higher than the value expected from thermal equilibrium given by  $\exp(-$

$523000/(RT)$ ) where  $T = 1173$  K, which gives  $5*10^{-24}$ . Clearly the formation of defects under flash is a new, far-from-equilibrium paradigm.

#### 7.4.6. Microstructure and Mechanical Behavior

The tensile stress strain curve is given in Figure 7-8 (a). It gives a yield stress of about 98 MPa, an ultimate tensile stress of 323 MPa and ductility of ~17%.

The fracture micrograph is given in Figure 7-8. Curiously it shows a dimpled fracture surface which is typical of dispersion strengthened metals<sup>113</sup>. In copper, the dispersed particles produce a dimpled fracture surface very similar to Figure 7-8<sup>113</sup>; indeed the oxide particles can be seen within each crevice of the dimpled surface<sup>114</sup>. In this dispersion strengthened alloys the particles concentrate the plastic strain, which nucleates voids that grow to cause ductile fracture. The surprising result in present experiments is that the dimples form without a dispersion.

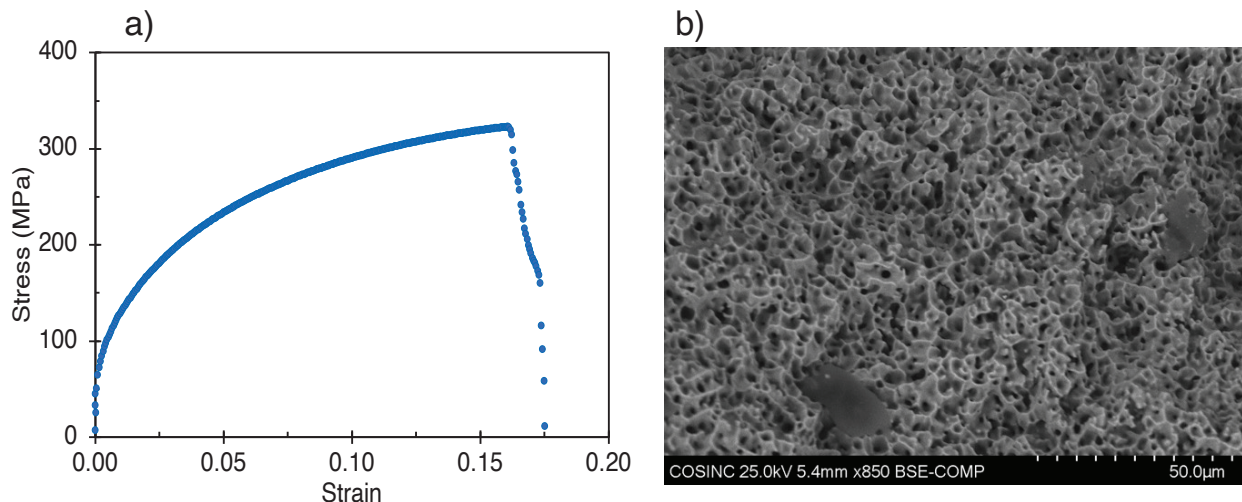


Figure 7-8: (a) Tensile stress-strain curve for the flash sintered nickel specimen (b) The SEM fractography showing dimples fracture surface morphology.

The fracture micrograph is given in Figure 7-8 (b). Curiously it shows a dimpled fracture surface which is typical of dispersion strengthened metals<sup>113</sup>. In copper, the dispersed particles produce a dimpled fracture surface very similar to Figure 7-8 (b)<sup>113</sup>; indeed the oxide particles can be seen within each crevice of the dimpled surface<sup>114</sup>. In this dispersion strengthened alloys the particles

concentrate the plastic strain, which nucleates voids that grow to cause ductile fracture. The surprising result in present experiments is that the dimples form without a dispersion.

In supplementary materials we describe the measurement of endothermic enthalpy during flash sintering by measuring the difference between the input electrical energy and the energy lost to black body and convective losses, and the enthalpy stored as specific heat. The difference when converted into the concentration of defects (Frenkels: vacancy-interstitial pairs) gives a value of 0.3 - 0.4% mole fraction of Frenkel pairs at specimen temperature of  $\sim 900^\circ\text{C}$ . This value is several orders of magnitude greater than the concentrations expected from thermal equilibrium. It is proposed that the defects form clusters that resist deformation and thus become the source of void nucleation. Indeed, in the case of copper, dispersed with nanoscale dispersion of alumina particles, a similar behavior was observed<sup>113</sup>.

## 7.5. Discussion

This is the third report on flash sintering of metals, viz., nickel. The first was on tungsten powders (shown in Section 5.0), a highly refractory metal. Nickel melts at  $1455^\circ\text{C}$  while the melting point of W is  $3383^\circ\text{C}$ . In classical solid state diffusion the diffusion coefficient scales with the melting point of the metal<sup>102</sup>. Normally, diffusion rates that occur at  $0.75T_M$  are needed for sintering within a few hours. Therefore, conventional sintering of tungsten requires much higher temperatures ( $\sim 2450^\circ\text{C}$ ) than nickel ( $\sim 1023^\circ\text{C}$ ).

Sintering of nickel and tungsten by flash is radically different than conventional as described above. Both metals have been shown to flash sinter at a temperature of approximately  $1000^\circ\text{C}$  at a similar current density ( $20 \text{ A mm}^{-2}$  – for workpieces of similar geometry). Clearly diffusion kinetics in flash sintering invokes a new paradigm. The ultrahigh concentration of defects is also consistent with a radically different behavior. Measurement of diffusion coefficients of cations

across bilayers, in real time, suggest the diffusion to be nearly  $10^8$  faster in flash<sup>103</sup>. The activation energy for diffusion is one half to one third of the literature values not only in these diffusion measurements but also in superplastic deformation<sup>104</sup>. Recent experiments where superimposition of magnetic fields was shown to migrate the flash from a dogbone sample into a free standing workpiece without electrical contacts<sup>105</sup>, suggests that flash is akin to a solid state plasma. In-operando experiments at Synchrotrons have shown that the crystal structure of the solid remains intact during flash, suggesting that the plasmas consist of ions, electrons, and holes. Much remains to be explored in this exciting new development.

It is gradually emerging that flash sintering is just one aspect of an ecosystem of “a complex network of happenings that relate to one another like a system”. The name also is consistent with the emerging universality of flash behavior observed in many different materials. For example, Ni and W, of very different melting points, show the onset of flash at the same current density (about  $5 \text{ A mm}^{-2}$ ) and full sintering near  $20 \text{ A mm}^{-2}$ , for specimens of the same geometry. In ceramics the onset of flash in ceramics has been shown to occur within a narrow band of power density (about  $30\text{-}50 \text{ mWmm}^{-3}$ ). The future is mysterious but promising for new scientific revelations.

The present experiments and the experiments with tungsten were carried out by direct current injection without the use of a furnace. One experiment on W with the furnace showed that flash sintering occurred at the same temperature but with a lower current density in the case of furnace heating because of the ambient heat from the furnace. This aspect of flash in metal needs to be explored further.

Additive manufacturing of metals is drawing technological interest. AM is mostly used to create “green” objects of various shapes which are subsequently sintered in the conventional way. The current rate flash sintering opens the gate for producing end-user ready parts, by in-situ AM.

## 7.6. Conclusion

Flash sintering of nickel powders follows earlier work on flash sintering of tungsten and rhenium powders. Thus, a new field of metal powder processing emerges. It has technological implications in additive manufacturing of metals, but even more significantly it opens the gate for revolutionary new science that touches plasma physics. The diffusion kinetics in flash is estimated to be several orders of magnitude greater than conventional literature values; the activation energies are one half to one third.

The emerging universal behavior of materials in the state of flash also points towards a radical departure from conventional thermodynamics, kinetics, and physics. The formation of new phases, far from equilibrium has already been demonstrated<sup>106</sup>. Much more work is needed which may lead to solid state electrolytes for Li+ batteries with unusually high ionic conductivities<sup>107</sup>.

The scientific community is rightly skeptical of unusual claims. However, the work on flash has developed significant depth and breadth, as shown by the long list of references from this laboratory. It is time for all of us to accept at least some of the unusual features of this phenomena and contribute to physics of the flash effect.

## CHAPTER FIVE: COMPARISON OF ENERGY CONSUMPTION FOR FLASH SINTERING AND OTHER METHODS

### **8.0. Comparative Analysis of Energy Consumption in Flash Sintering and other Metal Sintering Techniques**

#### **8.1. Summary**

Metals are traditionally sintered at 75% or higher of their melting point. Advancements in the field of metallic sintering have emphasized the need to lower furnace temperatures, reduce holding times, and consequently enhance energy efficiency. Besides faster processing time, another major benefit of these advancement is the reduction in the energy footprint of the process. The International Energy Agency (IEA) has highlighted that improving energy efficiency in manufacturing is pivotal to address the increasing energy demands. The IEA has emphasized the potential to diminish CO<sub>2</sub> emissions—directly correlated to energy consumption—by enhancing energy recovery in production processes and adopting innovative methods with superior energy efficiency compared to prevalent sintering techniques<sup>115</sup>.

Several field assisted sintering technologies (FAST) have emerged including spark plasma sintering (SPS), microwave sintering and more recently, flash sintering. While SPS and microwave sintering has significantly improved the processing time, reduced furnace temperature and lower the energy requirements, flash sintering has proven to be the fastest and have significantly seen reduction in processing temperature. For instance, the studies reported in Sections 5 to 7 of this thesis on rhenium, tungsten and nickel were carried out without furnace, achieving full sintering in less than a minute.

This chapter builds upon the pioneering investigation of flash sintering in metals reported in this thesis. We quantified the energy consumption in flash sintering of metals such as nickel, tungsten, titanium, and rhenium, and contrast them with other sintering methods including spark plasma

sintering, selective laser sintering, microwave sintering, electro discharge sintering, and hot pressing.

## 8.2. Introduction

Sintering has evolved into an important part of metal manufacturing, its significance have been amplified by its recent integration into metal additive manufacturing processes<sup>116</sup>. Conventional method of sintering typically involves heating the specimen to approximately 75-90% of its melting point at a specified rate and sustaining that temperature for several hours. Furnaces suitable for this process span a range from small, laboratory-scale units to expansive industrial models, with conventional sintering predominantly executed in electrical resistance furnaces. In these furnaces, heat generation results from electric current encountering resistance in a conductive material. Resistivity is temperature-dependent and varies across materials. For most metals, an increase in temperature leads to increased resistivity, a trend inversely observed in many nonmetals. In furnaces, the elements which conduct the electric current, generate heat due to their inherent resistance. This heat is then transmitted to the specimen via conduction, radiation, and convection.

Specific metal alloys, including nickel and iron-based variants, are employed in crafting furnace elements for low-temperature units (those with maximum temperatures below 1200°C). In contrast, refractory metals like molybdenum, tantalum, platinum, and tungsten are reserved for furnaces with a higher temperature threshold. The desired temperature and its rate of change are modulated by a temperature controller, with many laboratories experiments effectively conducted using a lab-scale tube furnace.

However, this method's energy consumption is intensive, a consequence of the elevated temperatures and prolonged hold times it necessitates. Benedikt et al.<sup>117</sup> illustrated that the majority

of the energy consumption in sintering arises from the initial furnace heating phase. In Figure 8-1, we see the correlation between furnace temperature and power usage. Taking a working temperature of 960°C as a reference point, the study found that the peak power consumption (160 kW) occurs while ramping up the furnace to the desired temperature. Maintaining this 960°C temperature demands 40 kW, but this requirement lowers to 18 kW when the furnace is kept at 600°C. Notably, no energy is expended during furnace cooling.

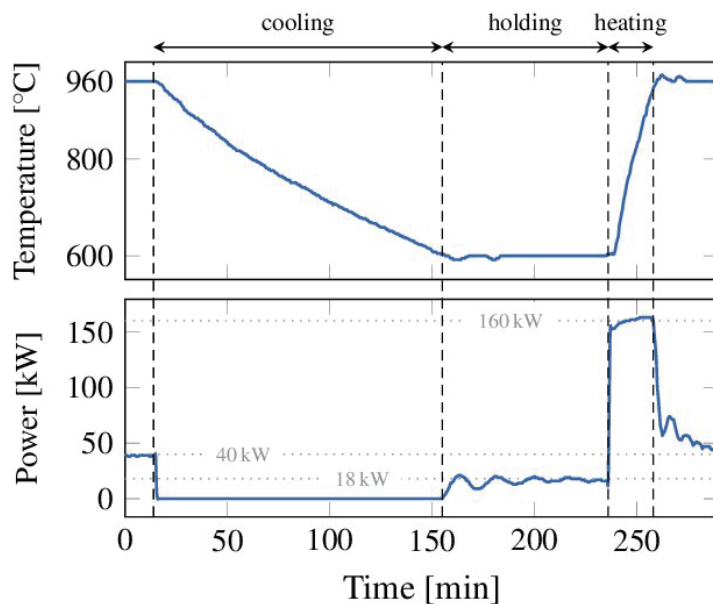


Figure 8-1: Power and Temperature relationship during laboratory scale furnace heating

Although many alternative sintering methods, especially FAST, have made notable improvement by reducing both the sintering temperature and the holding time, most of them still predominantly rely on furnaces or dies through which electrical energy is channeled. This thesis introduced the first demonstration of flash sintering on metals, viz., tungsten. The process was repeated on nickel and rhenium. Findings from those studies have shown that metals can be sintered rapidly at room temperature. Huge defect generation have been found to be a major driving mechanism of the flash sintering of metals. The aim of this chapter is to show that the consequence of the ultra-fast nature

of flash sintering and the room temperature requirement is that less energy is required when compared to existing methods.

### **8.3. Methods**

Metal powders of nickel, tungsten, titanium, and rhenium were compacted in a die to shape a dogbone specimen, applying pressures between 170 and 200 MPa. Once formed, the specimen was connected to a power source and subjected to flash sintering in a constant current mode, where a steady current rate was maintained. The Archimedes method was employed for density measurements.

A custom software, interfaced with a National Instrument data acquisition device, logged the power source's output current, input voltages, and associated timestamps. Power was deduced using the formula: Power (W) = Current (I) x Voltage (V). To ascertain the total energy utilized throughout each experiment, the power (in Watts or Joule/seconds) was integrated over time (in seconds) to determine the area under the curve (J). Subsequently, this value was normalized by the specimen's volume to deduce the energy consumption per cubic volume.

### **8.4. Results**

Energy consumption during various sintering methods including flash sintering, spark plasma sintering, microwave sintering, selective laser sintering and electro-discharge-sintering are compared in this section. Starting with flash sintering, data from flash sintering experiment on nickel, titanium, tungsten and rhenium were analyzed. The power curve was plotted against time and integrated to obtain the energy consumed. The total energy consumed per cubic volume was determined. In other methods, data from literature were extracted and compared to result obtained from the flash sintering technique.

### 8.4.1. Flash Sintering

#### a) Nickel

Nickel powders of 99.8% purity and an average particle size of approximately 44  $\mu\text{m}$  sourced from Alfa Aesar were molded into a dogbone specimen. The dogbone specimen's volume is 32.06  $\text{mm}^3$ . The experiment was performed using different current rates such as 1, 2 and 5 A/s. Previous studies (Section 5 and 7) have confirmed that sintering depends on current density and not current rate, so this offers us the flexibility of control the rate of sintering. The sintered specimen achieved a final density exceeding 99%.

The resistivity profile presented in Figure 8-2a shows the progression of resistivity with current density in three cycles at a current injection rate of 1 A/s. The first cycle termed the flash sintering cycle showed an initial peak resistance followed by decline after inter-particle contact have been established. The following two cycles were the repeat of the flash process on the specimen sintered in cycle 1.

In Figure 8-2b, we show the power curve against time at 1, 2 and 5 A/s. The summary of the energy consumption after integrating the power with time is given in Table 8-1. The results show that increasing the current injection rate leads to a decrease in energy consumption. Specifically, at a rate of 2 A/s, energy consumption is reduced to 1.64 J/ $\text{mm}^3$  from the 4.45 J/ $\text{mm}^3$  observed at 1 A/s. A further increase to 5 A/s diminishes the consumption to 1.08 J/ $\text{mm}^3$ .

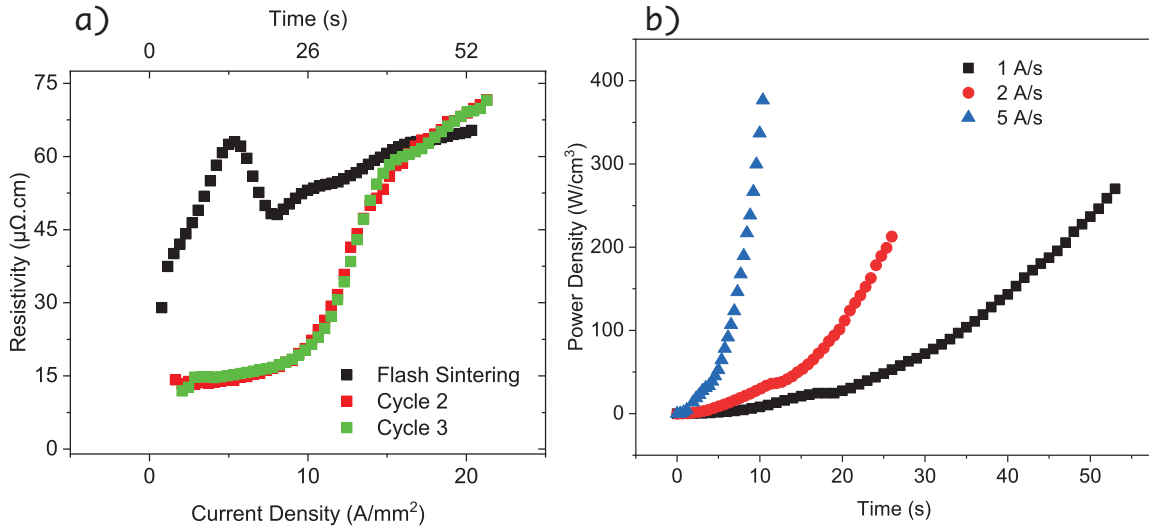


Figure 8-2: (a) Resistivity as a function of current density during the flash sintering of nickel. Cycle 1 depicts a first repeat of the flash of an already flashed specimen while another repeat was depicted by cycle 2. (b) Power density as a function of time during the flash sintering of nickel.

Table 8-1: Summary of energy consumption at different rates for flash sintered nickel at various rates

Rate (A/s)	Area Under Curve (J)	Volume ( $\text{mm}^3$ )	Energy Consumed ( $\text{J/mm}^3$ )
1	145.91	32.06	4.45
2	50.62	30.96	1.64
5	32.96	30.52	1.08

## b) Titanium

A dogbone specimen was prepared by compressing titanium powder (sourced from Alfa Aesar) with 99.5% purity and a particle size of -325 mesh, under pressures ranging from 170 to 200 MPa. The volume of the resulting specimen is  $62.37 \text{ mm}^3$ . This specimen was subjected to flash sintering with a current injection rate of 1 A/s. The final density of the flash sintered titanium determined by the Archimedes method, is 98.6% of titanium's theoretical density.

The resistivity behavior presented in Figure 8-3a shows similar behaviors seen in tungsten and rhenium. The initial resistance is high, then followed by a continuous decline – depicting the

establishment of inter-particle contacts. Upon re-flashing the flash sintered titanium, the resistivity started from lower resistance than that seen in the green specimen.

The power-time curve, as depicted in Figure 8-3b, indicates a consistent uptrend in power consumption over time. The specimen's volume measures  $62.37 \text{ mm}^3$ . The integrated area under the power curve calculates to 271.6 J, resulting in an energy consumption of  $4.35 \text{ J/mm}^3$  at the 1 A/s current rate.

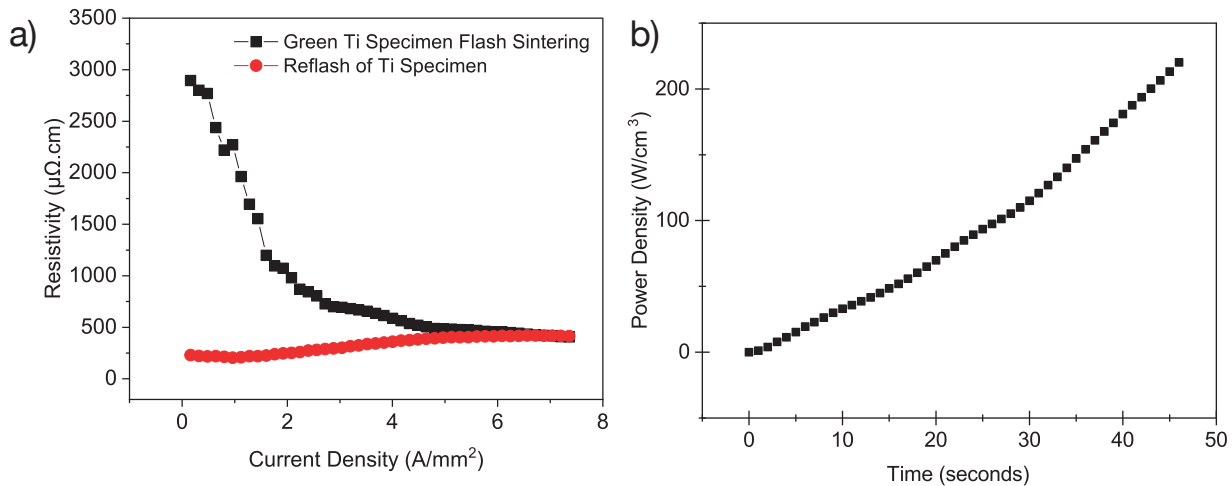


Figure 8-3: (a) Curve of resistivity vs current density for flash sintering of green titanium compact (black) and flash of a dense titanium specimen with flash history (red). (b) Power vs time during the flash sintering of green titanium compact.

### c) Tungsten

Tungsten powder, sourced from Alfa Aesar, with a purity of 99.9% and a particle size of  $12 \mu\text{m}$ , was compressed into a dogbone specimen using a pressure of 200 MPa. The specimen's volume, derived from its dimensions (length, breadth, and thickness), is  $20.65 \text{ mm}^3$ . The rate of current injection for this experiment is 0.5 A/s.

Figure 8-4a presents the resistivity curve plotted against current density for both flash sintering and two subsequent reflash cycles of the sintered specimens (designated as cycle1 and cycle2). An

initial peak was observed and immediately followed by a continuous decline. This behavior reflects the breakdown of resistive layer and the formation of contacts between particles. Notably, this effect was absent in the subsequent cycles.

The power-time curve, essential for energy consumption computation, is illustrated in Figure 8-4b. The total energy utilized during the process is 263 J, translating to a volumetric energy consumption of 12.74 J/mm<sup>3</sup>.

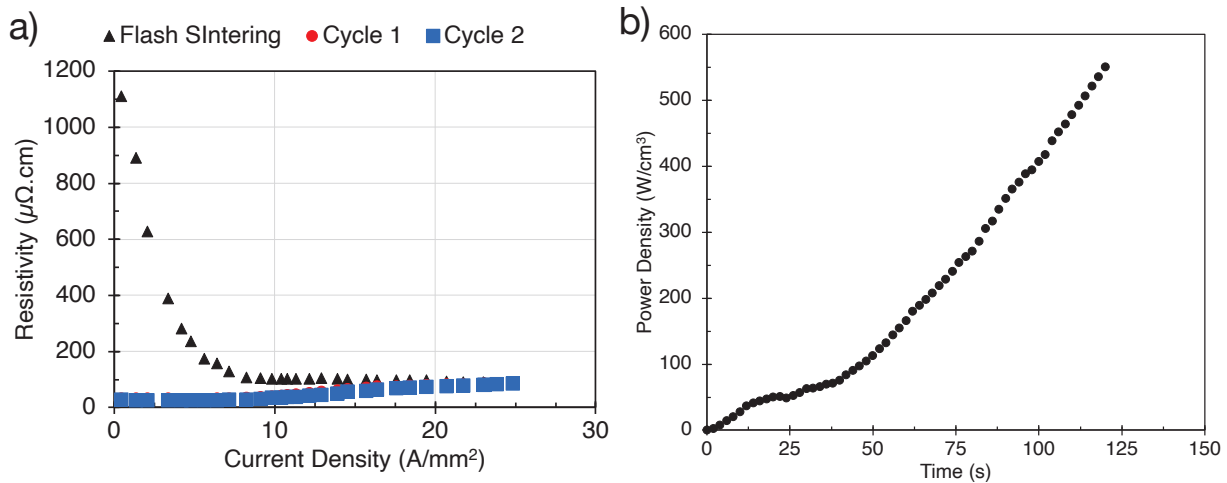


Figure 8-4: (a) Curve of resistivity vs current density for flash sintering of green tungsten compact (black) and flash of a dense tungsten specimen with flash history (red and blue). (b) Power vs time during the flash sintering of green tungsten compact.

#### d) Rhenium

Using 99.99% pure rhenium powders with a size of -325 mesh provided by Fisher, a dogbone specimen was produced under a 140 MPa pressure via a hydraulic press from Dake Corporation. Flash sintering of the dogbone was conducted at room temperature using a Hewlett Packard 6261B (0-20V 0-50A) power source, with a current injection rate of 1 A/s. The green density of the rhenium dogbone was 74% of the metal's theoretical density. Post-sintering, the final relative density ranges from 96% to 97%.

As depicted in the resistivity curve in Figure 8-5, a decrease in resistance was evident, indicative of the establishment of particle-to-particle contacts and the disintegration of resistive layers. Notably, this sharp decline was absent in the subsequent flashes, labeled as cycle 1 and cycle 2, signifying the transition to the sintering phase following the flash onset.

The specimen's volume is  $9.72 \text{ mm}^3$ . The overall energy spent during the procedure was 241.9 J, translating to a volumetric energy consumption of  $24.9 \text{ J/mm}^3$ .

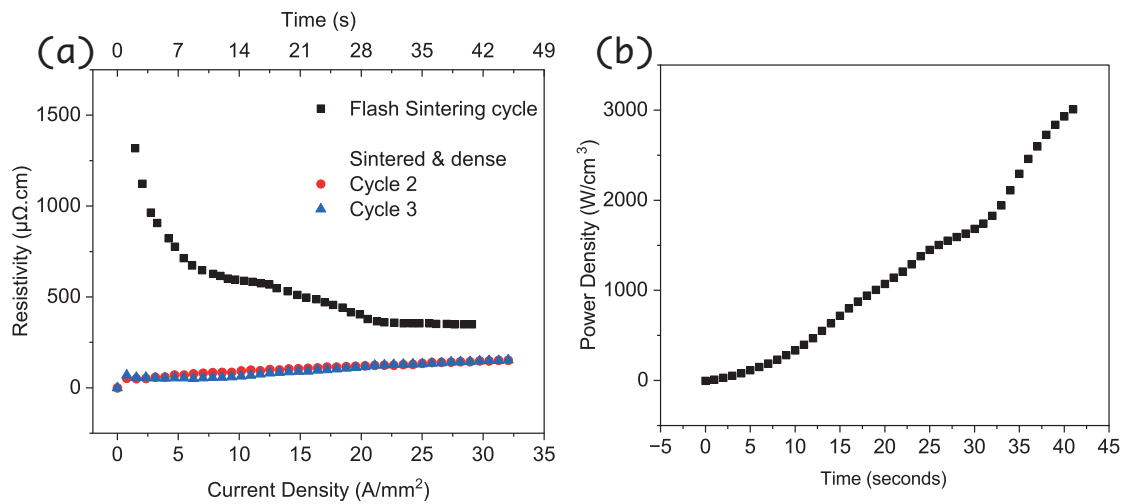


Figure 8-5: : (a) Curve of resistivity vs current density for flash sintering of green rhenium compact (black) and flash of a dense rhenium specimen with flash history (red and blue). (b) Power density. vs time during the flash sintering of green rhenium compact

#### 8.4.2. Other Sintering Methods

##### a) Conventional Sintering by Furnace Heating

Conventional sintering is known to be energy-intensive, particularly because of the significant energy needed to heat the furnace to the required temperature. As highlighted by Benedikt et al.,<sup>117</sup> and shown in Figure 8-1, a laboratory-scale furnace can demand up to 160 kW to attain  $960^\circ\text{C}$ , plus an additional 40 kW to maintain a stable temperature of  $960^\circ\text{C}$ . Given the long holding time

required of conventional sintering of metals, the cumulative energy consumption can be significant.

### b) Microwave Sintering

Unlike conventional sintering which relies on external heat sources - such as furnace elements - to transfer heat to the material through conduction, convection, and radiation; microwave sintering introduces a different approach. In microwave sintering, electromagnetic energy directly converts into heat within the material being processed. This intrinsic heating mechanism not only prevent potential thermal losses but also brings about other advantageous attributes. For instance, microwave heating can process materials in notably less time compared to conventional methods. This efficiency can be attributed to its ability to achieve exceptional heating rates, often exceeding 400°C per minute. In a study examining the microwave sintering of a tungsten, nickel, and iron alloy, there was a significant 75% reduction in process time compared to that required by traditional sintering<sup>118</sup>.

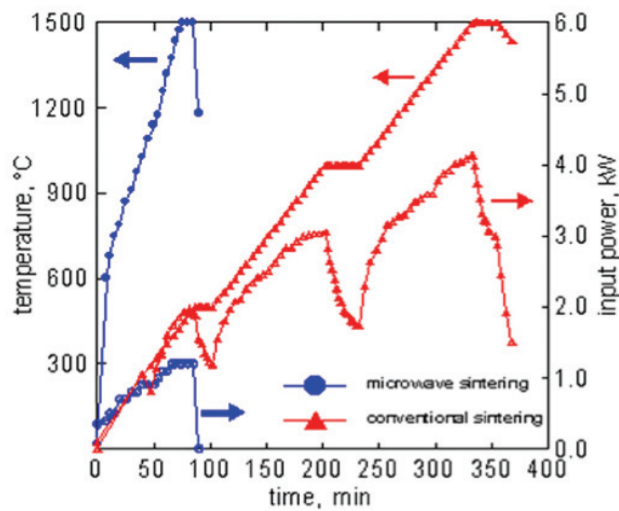


Figure 8-6: Comparison of power consumption and heating profile of microwave and conventional sintering of 92.5W-6.4Ni-1.1Fe alloy.

Referring to Figure 8-6, a comparison of the energy consumptions of microwave sintering and conventional sintering is shown. For microwave sintering, the energy used amounted to 75.9 kJ, whereas conventional sintering consumed a significantly larger 860.6 kJ. Calculating the volumetric energy consumption using the specimen dimension (12.7 mm diameter and 10 mm height), the total energy consumption was 59.9 J/mm<sup>3</sup> for microwave sintering and 679 J/mm<sup>3</sup> for the conventional method. Another comparative study between microwave sintering and conventional sintering highlighted the energy savings achieved with microwave sintering. Specifically, when sintering magnesium and Mg/Al<sub>2</sub>O<sub>3</sub> nanocomposites, 96% less energy was used in microwave sintering compared to traditional furnace sintering. In practical terms, sintering 40mm x 35mm (diameter x height) billets made from these materials via microwave sintering took only 0.7 kWh over 25 minutes. In contrast, the tube furnace method required a staggering 17 kWh over a duration of 170 minutes<sup>119</sup>.

A study using microwave sintering to sinter tungsten achieved 93% from an 85% green density at a furnace temperature of 1800°C. The process had a peak power usage of 20 kW and spanned 6 to 7 hours<sup>22</sup>. The energy consumption of microwave sintering of metals and metal alloys are well above the range obtained using the flash sintering approach as shown in section 8.4.1.

### c) Spark Plasma Sintering

Spark Plasma Sintering employs a pulsed DC current that flows through graphite dies which encapsulate the conductive powder material. This technique is characterized by its rapid heating capabilities, allowing materials to achieve sintering within a minimal timeframe.

The dimension of the graphite dies, especially their height and diameter, are crucial variables that influence the energy consumption during the SPS process. The energy must first navigate through these dies before it reaches and affects the specimen inside. As the dimensions of these dies

increase, so does the energy required to complete the sintering process. Specifically, enlarging the die diameter has been observed to have a more significant impact on energy consumption than just increasing its height<sup>120</sup>.

A study on nickel showcased this correlation between die size and energy use. In this research, nickel was subjected to spark plasma sintering using graphite dies of 27.8 mm and 30 mm diameters, both maintaining a thickness of 10 mm. Findings from this experiment reiterated the essential consideration of die dimensions in optimizing and regulating energy use during the sintering process<sup>120</sup>.

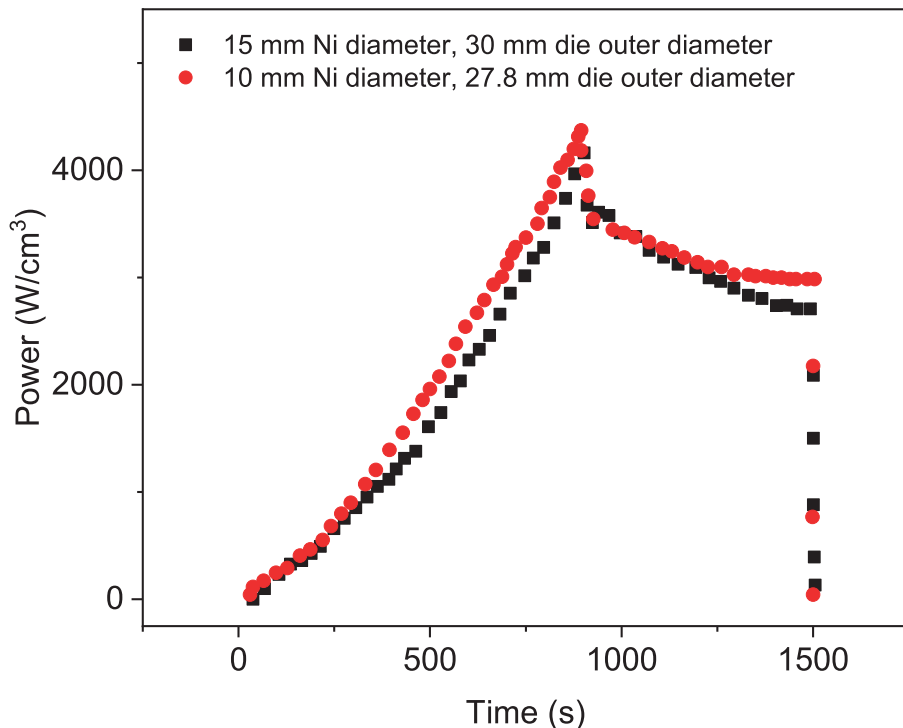


Figure 8-7: Power consumption for (10/28.7) and (15/30) dies as a function of time at 750 °C, 70 MPa and 50°C min<sup>-1</sup> heating rate.

Using data from Figure 1a of the article<sup>120</sup>, the area under the curve was calculated by integrating the power curve over time, yielding values of 842.98 kJ and 346.84 kJ for the 30 mm and 27.8 mm diameter dies, respectively. In Figure 8-7, the relationship between power density and time is

presented. The SPS process lasted for 1500 seconds, and the calculated energy consumption was  $238.5 \text{ J/mm}^3$  for the 30 mm diameter die and  $114.3 \text{ J/mm}^3$  for the 27.8 mm diameter die.

In contrast, the flash sintering of nickel exhibited an energy consumption of only  $4.55 \text{ J/mm}^3$  using a current rate of 1 A/s, lower consumption was recorded by increasing the rate of current injection. The difference in energy consumption between these methods underscores the significant role of eliminating dies from the process and directly injecting current into the specimen in the flash sintering technique.

#### d) Electro Discharge Sintering

Electro discharge sintering deploys a method wherein current flows through conductive dies containing a metallic powder compact. This induces joule heating, which combines with external mechanical pressure to densify the metallic powder compact. Factors such as die geometry, size, and the conductivity of the enclosed metallic powder significantly influence densification. This sintering technique harnesses a capacitor bank to discharge electrical energy. Despite the high electrical energy requirement due to the dies, the process's rapid nature - completing in mere microseconds - results in relatively low energy consumption.

A study conducted by Ganesh et al.<sup>32</sup> explored sintering of tungsten, steel, and tungsten-steel composites using this method. Utilizing 80 kJ of discharge energy through a 19 mm diameter die to a 3 mm thick specimen resulted in an energy consumption of  $94.1 \text{ J/mm}^3$  per unit volume. This method proved unsuccessful for tungsten sintering, presumably due to the restricted discharge capacity. Consequently, sintering tungsten would necessitate higher discharge energy. The consumed energy in this method, although insufficient for tungsten full sintering, still surpassed the  $12.74 \text{ J/mm}^3$  expended in the 0.5 A/s current rate flash sintering approach.

Another study focused on titanium metal used the electro discharge sintering method<sup>121</sup>. They applied a discharge of 5 kJ/g to a titanium compact comprised of 1g of titanium powder. Given the specimen's dimensions—6.2 mm diameter and 8.7 mm height—the consumption totaled 19.04 J/mm<sup>3</sup>. If we consider the entire energy requirement of the process using a 10 mm diameter stainless-steel die, 8.7 mm height, and a discharge energy of 10 kJ (derived from the 200 µF discharge at 10 kV using the formula  $E = \frac{1}{2}C \cdot V^2$  where  $E$  is the electrical energy,  $C$  is the capacitance and  $V$  is the voltage), the consumption equals 14.64 J/mm<sup>3</sup>. The compact's final density was 90%. In comparison, the 1 A/s current rate flash sintering of titanium consumed a mere 4.35 J/mm<sup>3</sup> but achieved a density exceeding 98.6%.

Another instance of electro discharge sintering was documented for nickel.<sup>122</sup> The study used a die with a 3.7 mm inner diameter and 8.5 mm height containing nickel powder, which had a 0.3 µm oxide layer. A total energy of 4.3 kJ was discharged to sinter the specimen to a density of 60%, without prior compaction. This resulted in an energy consumption of 32.8 J/mm<sup>3</sup>. If the outer die diameter, presumed to be 6 mm (2.3 mm more than the inner diameter), is considered, this figure decreases to 17.9 J/mm<sup>3</sup>. Nonetheless, both values exceed the 4.55 J/mm<sup>3</sup> obtained through the 1 A/s flash sintering of nickel.

### e) Laser Sintering

Laser sintering techniques, such as selective laser sintering (SLS) and selective laser melting (SLM), have gained prominence in the additive manufacturing of metals due to their precision and efficacy. These techniques leverage high energy densities to facilitate the fusion of particles.

For example, Yap et al.<sup>123</sup> reported achieving a  $98.9 \pm 0.1\%$  relative density of nickel using a laser power of 350 Watts at a scan speed of 700 mm/s. This process consumed 180 J/mm<sup>3</sup>, notably

higher than the 4.55 J/mm<sup>3</sup> consumed during 1 A/s flash sintering of nickel to achieve a comparable relative density. In another study, selective laser melting of tungsten yielded a 98.4% relative density by applying a 300 Watts laser power at scan speeds ranging from 200 to 400 mm/s.<sup>124</sup> The process demanded an energy of 1000 J/mm<sup>3</sup>, significantly surpassing the 12.74 J/mm<sup>3</sup> used in the 0.5 A/s flash sintering approach. A subsequent study on titanium using SLM consumed 120 J/mm<sup>3</sup> to attain a 99.5% relative density by harnessing laser powers of 165 and 135 Watts at scan speeds of 138 and 112 mm/s, respectively<sup>125</sup>. In contrast, flash sintering of titanium at 1 A/s required only 4.35 J/mm<sup>3</sup>.

Many studies on the selective laser melting of alloys have reported energy densities exceeding 100 J/mm<sup>3</sup> to achieve full density. For instance, the SLM of AlSi10Mg and CoCrMo alloys consumed volumetric energy densities of 208.3 J/mm<sup>3</sup> and 151 J/mm<sup>3</sup>, respectively<sup>126,127</sup>. An analysis of 316L stainless steel using selective laser melting determined that a minimum of 100 J/mm<sup>3</sup> volumetric energy density is essential for melting the alloy<sup>128</sup>. This study applied parameters presented in Table 8-2, concluding that the alloy achieves full melting at an energy density of 121 J/mm<sup>3</sup>. It cited a previous work<sup>129</sup> which melted the same alloy at 100 J/mm<sup>3</sup>, implying that over 100 J/mm<sup>3</sup> is at least required for melting 316L stainless steel via the SLM technique.

Table 8-2: Selective laser melting of 316L stainless steel deposition parameters and energy density at a constant beam diameter of 55 µm. Obtained from Bertoli et al.<sup>128</sup>. VED is Volumetric Energy Density.

<b>Laser Power</b>	<b>100</b>	<b>200</b>	<b>300</b>	<b>400</b>	<b>500</b>	<b>VED</b>
	W	W	W	W	W	J/mm <sup>3</sup>
<b>Scan Speed (mm/s)</b>	100	200	300	400	500	242
	150	300	450	600	750	162
	200	500	750	1000	1250	121
	250	600	900	1200	1500	97
	300	600	900	1200	1500	81

	500	1000	1500	2000	2500	48
--	-----	------	------	------	------	----

## 8.5. Discussion

Flash sintering, with its current density-dependent densification process, emerges as the most ecofriendly among all existing sintering methods of metals. Its major advantages lies in its ability to channel electrical energy directly into the specimen at a controllable rate. When compared to traditional techniques such as microwave sintering, spark plasma sintering, selective laser sintering, conventional sintering, and electro-discharge-sintering, flash sintering achieved comparable, sometimes superior, densification levels at significantly reduced volumetric energy consumption.

Electro discharge sintering and spark plasma sintering, despite being rapid also tend to consume more energy per unit volume than flash sintering. The influence of die geometry and size, particularly in spark plasma sintering, adds complexity to the process and can lead to increased energy consumption, especially with larger die diameters. The inclusion of die in the experimental setup of these methods often culminate in higher total energy consumption compared to flash sintering.

Laser sintering techniques, including selective laser sintering (SLS) and selective laser melting (SLM), although widely adopted in additive manufacturing due to their precision, exhibit considerably higher energy consumption than flash sintering. Materials like nickel, tungsten, and titanium, when sintered using laser techniques, often demand energy densities that are few orders of magnitude higher than what flash sintering would require for comparable specimen type and final densities.

In the context of the diverse sintering methodologies, flash sintering stands out due to its high energy efficiency. As sustainability and efficiency become paramount in the manufacturing sector, the energy-economical nature of flash sintering, combined with its ease of setting up, gives it a comparative advantage over other methods.

### **8.6. Conclusion**

The need to combine sustainable process with high efficiency in the manufacturing sector has necessitated the need techniques like flash sintering. Methods such as microwave sintering, spark plasma sintering, laser sintering and electro-discharge-sintering have significantly enhanced the energy efficiency in the field of sintering compared to conventional sintering. However, the present study shows that flash sintering technique is more efficient than these alternative methods.

While the laboratory successes of flash sintering are noteworthy, a significant opportunity lies in examining the scalability of flash sintering for larger-scale production. Future endeavors should target the integration of this technique into mainstream manufacturing like additive manufacturing.

## CHAPTER SIX: EXPLORATORY STUDIES FOR FUTURE RESEARCH

Most of the exploratory studies for future investigations are carried out on potential application areas of the flash sintering of metals. In the following subsections, examples of application areas where preliminary work have been done are given:

- 1) Additive Manufacturing of Metals: One of the most promising avenues for flash sintering is the additive manufacturing of metals. Additive manufacturing of metals typically requires post-processing sintering to improve final density and enhance mechanical properties of the printed parts. Integrating flash sintering into this process could drastically reduce time between components printing and product readiness. Preliminary studies on this application area showed that plasma can be transferred from one layer to another layer, thereby sintering upper layers even when current is not directly passed through it. However, a major challenge that will require further study is how to join these layers together.
- 2) Surface Modifications: Flash sintering can potentially play a key role in surface modifications of metallic materials. This method can be adopted to create continuous coating of metallic materials layer on a base metal, thereby altering properties such as mechanical hardness, electrical conductivity, corrosion resistance, and wear resistance. An example of such application is presented in Section 9.0 of this thesis where continuous coating of copper was achieved on titanium surface. The electrical conductivity of the initial specimen was improved after coating.
- 3) Composite and Alloy Manufacturing: The creation of metal composites and alloys often necessitate the infusion of a different kind of metal into another metal matrices or uniform dispersion of one metal within another metal.

## **9.0. Exploratory Study1: Surface coating of Titanium Metal with Copper**

### **9.1. Summary**

In this exploratory study, the flash sintering techniques was used to deposit a thin copper layer on a flash-sintered titanium dogbone specimen. This approach involved winding a copper wire, 250 $\mu\text{m}$  in thickness and 100mm in length, around the 16mm gauge length of the titanium dogbone. An electric current was consistently applied to the dogbone at a rate of 6 A/s until a peak current density of 16.61 A/mm<sup>2</sup> was achieved. This density was sustained for 7 seconds before discontinuing the power source. The deposition process resulted in a consistent copper layer, ranging from 50 $\mu\text{m}$  to 60 $\mu\text{m}$  in thickness, over the entirety of the titanium dogbone gauge. The process was completed in 16 seconds and led to a 10% enhancement in electrical conductivity. Microstructural analysis revealed bond between the copper layer and the titanium substrate, devoid of voids and discontinuities.

### **9.2. Introduction**

Numerous techniques exist for depositing copper on titanium, ranging from micro-arc oxidation technology (or plasma electrolytic deposition)<sup>130</sup>, electrodeposition<sup>131</sup>, and vacuum deposition<sup>132</sup> to cold spraying<sup>133</sup>, high-velocity arc spraying<sup>134</sup>, and high-velocity combustion wire spraying<sup>135</sup>. The innovative method discussed in this paper, inspired by flash sintering techniques, introduces a fast and energy-efficient method to achieve a continuous coating.

Earlier endeavors to deposit copper on titanium have been reported<sup>136–138</sup>. Rosa et al achieved a smooth, adherent copper coat on titanium wires through electrodeposition in acidic copper sulphate solutions<sup>139</sup>. They observed notable improvements in electrical conductivity, attributing them to the seamless adherence of copper to titanium without significant flaws. Maddu et al showcased

copper deposition on a Titanium alloy – Ti6Al4V using the electro discharge coating method. Utilizing the Technique for Order of Preference by Similarity to Ideal Solution (TOPSIS), they achieved a 20 $\mu\text{m}$  coating thickness<sup>140</sup>. For biomedical purposes, copper is seen as an ideal coat for titanium-based bone implants. Wang et al employed the microarc oxidation technique to produce a microporous Cu-TiO<sub>2</sub> coat on titanium. In vitro studies highlighted the coat's non-toxicity and its capacity to foster bone tissue formation and osseointegration at the titanium-bone implant interface<sup>141</sup>.

The present study use the flash sintering setup to deposit a consistent 50 $\mu\text{m}$  copper layer on titanium. We examine the in-situ electrical resistance behavior and detail the microstructure of the cross-section, copper surface, and fracture surface. Additionally, the post-coating electrical conductivity enhancements are shown.

### **9.3. Method**

#### **9.3.1. Preparation of Titanium Specimens**

Titanium powders with a purity of 99.8% and a particle size of -325 mesh, supplied by Alfa Aesar, were utilized in this research. The powder was cold pressed at a pressure of 170 MPa to produce a dogbone-shaped green compact of titanium with 86% green density. The dimensions of the dogbone specimen were 23 mm x 3.53 mm x 1.01 mm (length x width x thickness). Using the Archimedes measurement method, the specimen's green density was calculated to be 86% of titanium's theoretical density.

#### **9.3.2. Flash Sintering**

Flash sintering was carried out by injecting current into the titanium specimen, suspended on two tungsten electrodes connected to an HP 6261B power supply. The power source was regulated programmatically. This script managed the current injection rate and recorded the voltage readings

from a Keithley digital multimeter. An optical pyrometer from Micro Epsilon was employed for temperature data acquisition. A national instrument data acquisition device (NI DAQ) was used to interface the hardware components with the software.

### **9.3.3. Flash Deposition**

Following flash sintering, the titanium dogbone underwent a slight polishing (1-3 $\mu\text{m}$  thickness) to eliminate the titanium oxide layer. A pure copper wire (99.99% purity), 100mm in length and 250 $\mu\text{m}$  thick, was coiled around the titanium's gauge as depicted in Figure 9-1. The assembly, with the copper wire in place, was suspended between two tungsten electrodes and connected to the HP 6261B power source (Figure 9-1a). The software interfaced with the power supply to manage power injection at a rate of 6 A/s. An optical pyrometer, set with an emissivity of 0.3 for the titanium surface, monitored temperature.

Upon reaching a peak current density of 16.61 A mm<sup>-2</sup> at 52 Amps, the current was sustained for 7s. A CCD camera, operating at 10 frames per second, measured the flash deposition process in real-time. A snapshot from the procedure (0 A mm<sup>-2</sup>) and post-flash deposition can be seen in Figure 9-1b. Figure 9-1c provides a photo (captured on a smartphone) of the samples at different stages.

### **9.3.4. Microstructure Analysis**

Post-deposition, the cross-section and surface of the Cu-coated-Ti were mounted on acrylic using Allied QuickCure materials. Subsequent polishing employed polishing papers ranging from 240 $\mu\text{m}$  to 1 $\mu\text{m}$ . The polished surface was etched for 30 seconds in a solution containing 5ml Ammonia, 5ml water, and 3ml HNO<sub>3</sub>. After rinsing in water, specimens were air dried. Microstructural observations were carried out using a Hitachi SU3500 scanning electron

microscope at the Colorado Shared Instrumentation in Nanofabrication and Characterization (COSINC).

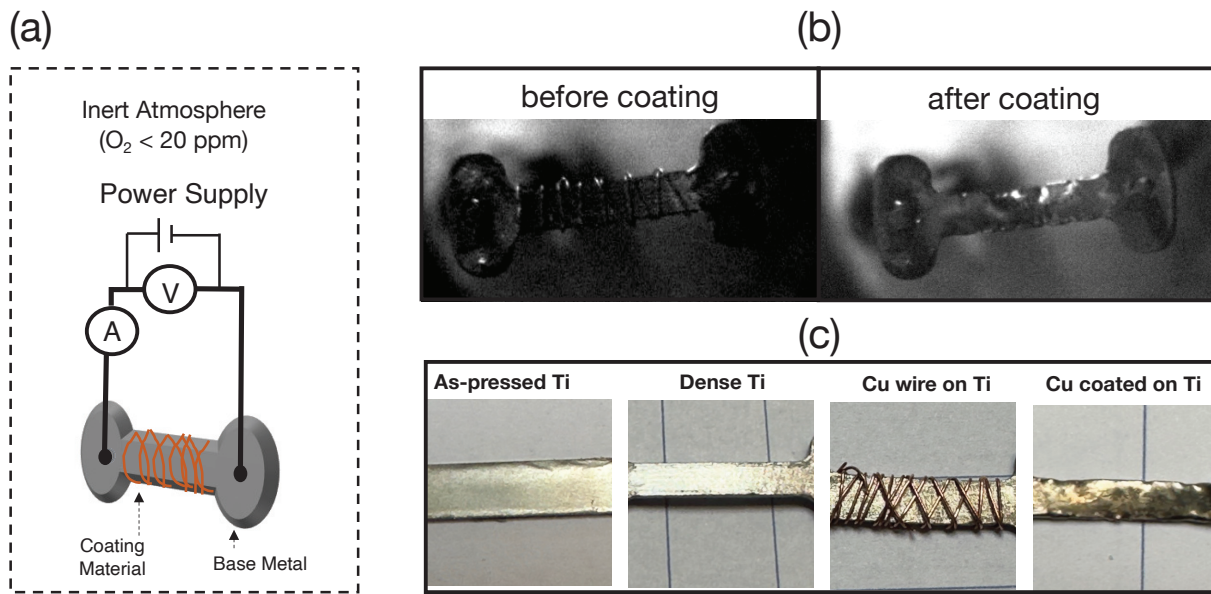


Figure 9-1: a) illustration of the flash deposition setup. (b) CCD camera images of the specimen before and after deposition. The “before coating” image shows the 0.25mm thick and 100 mm long copper wire coiled around the dense titanium dogbone. The “after coating” image shows the copper coated titanium (c) Phone captured images of the titanium dogbone after pressing, after flash sintering, after the copper wire is coiled around it and after deposition.

## 9.4. Results and Discussion

### 9.4.1. Resistance Analysis during Deposition

As illustrated in Figure 9-2a, voltage continuously increased as current is ramped up. This rise in Decrease in resistance was observed with increasing current as seen in Figure 9-2b. Initial resistance peaked at  $0.163\Omega$  and quickly dropped to an approximate  $0.1\Omega$  at a current density of  $5.9 \text{ A mm}^{-2}$ . From  $5.9 \text{ A mm}^{-2}$  to  $16.61 \text{ A mm}^{-2}$ , the resistance descended further to  $0.06\Omega$ .

This significant change in resistance is consistent with the electric breakdown voltages of oxide or resistive layers, correlating with findings from similar studies where electrical energy was introduced into metals<sup>142,143</sup>.

Utilizing an insitu temperature pyrometer, with the emissivity set to 0.3 for Ti (accounting for the shift to copper emissivity at elevated temperatures in the error bar), Figure 9-2a and 9-2b show that temperature continuously increased. The final temperature is estimated to approach the melting point of copper, as evident from the temperature profile's error bar.

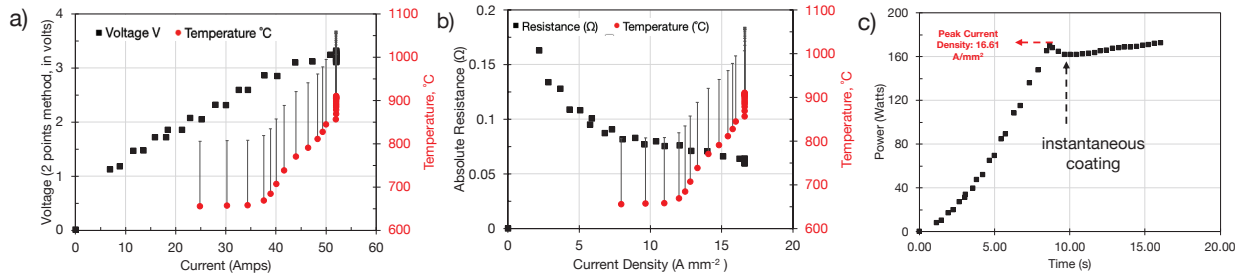


Figure 9-2: (a) Voltage vs current during flash deposition (b) Resistance vs Current Density (c) Power vs Time during flash deposition of Cu-coated-Ti

In the power curve during the holding time, a slight drop was noticeable (Figure 9-2c). At this juncture, instantaneous coating was observable in the video; molten copper was seen spreading over the titanium surface. This slight drop in power can be associated with the bond formation between the titanium surface and the copper coating, which removed the current flow barrier between the two layers. Knowing the relation  $P = I^2R$ , where power (P) is directly proportional to the square of the current (I) multiplied by resistance (R), and given that current remained constant during holding, the only factor causing the subtle power drop during coating (Figure 9-2c) would be resistance. This can be explained by the increase in the contact area between the molten copper layer and the titanium substrate.

Alternatively, another potential explanation for this power drop could be attributed to a loss of molten copper, assuming it increased in volume beyond what the titanium base could support. This might occur if energy input exceeds a certain threshold, preventing the titanium from retaining the liquid copper phase, leading to a spillage of the molten metal. The shortening of the current

pathway, resulting from molten copper loss, would decrease heat generation and, consequently, reduce temperature. In metals, a temperature decline would lower bulk resistivity since resistivity is inversely proportional to temperature. However, in this study, no temperature drop was observed, negating the theory of molten copper loss. Further evidence against this theory was the absence of any visible molten copper loss in the CCD camera footage.

#### **9.4.2. Microstructural Analysis of Cu-coated-Ti Specimen**

The SEM micrographs of the Cu-coated-Ti cross-section, as depicted in Figure 9-3a and 9-3b, clearly illustrate bonding of the copper layer and the titanium substrate. There is an absence of any noticeable gaps or discontinuities, an observation that is further supported by the surface micrograph (Figure 9-3d), which showcases a uniform layer of copper coating on the titanium.

Complementing this visual observation, the EDS (Energy Dispersive Spectroscopy) analysis (Figure 9-3c) provides a compositional breakdown. The line analysis distinctly reveals the simultaneous presence of both Cu, displayed with a brighter contrast, and Ti, with a darker hue. Quantitatively, the atomic% composition for Cu was determined to be 28.61%, while Ti comprised 71.39%.

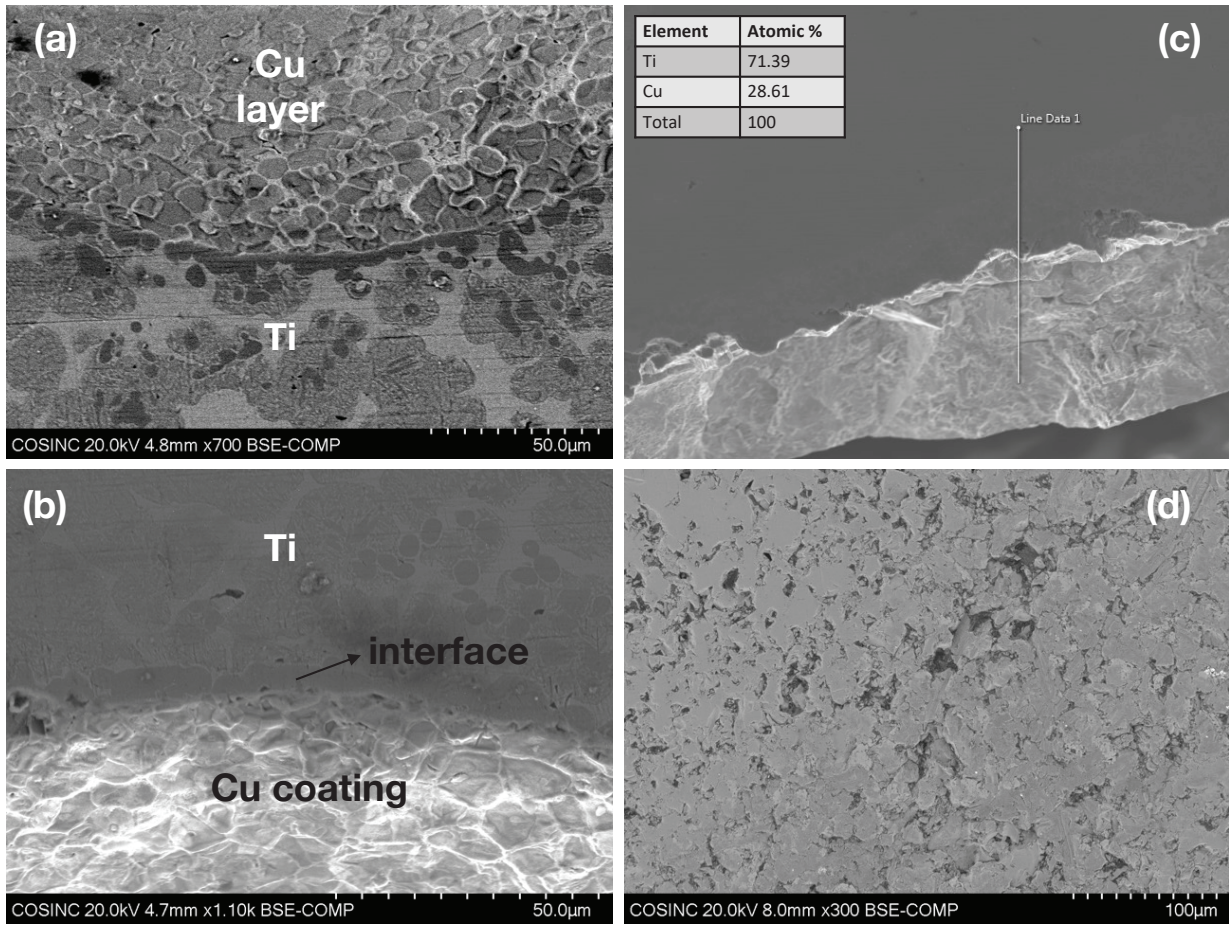


Figure 9-3: (a) & (b) Micrograph of the cross section after flash deposition showing the layer of Cu on flash sintered Ti dogbone showing excellent bonding at the interface. (c) EDS line scan analysis shows 71.39 at% and 28.61 at% of Ti

#### 9.4.3. Fracture Surface Morphological Analysis of Cu-coated-Ti

Breaking the samples intentionally by center-loaded stress allows for an in-depth analysis of their cross-sectional fracture morphology. The SEM images of the uncoated, flash-sintered titanium is shown in Figure 9-4a(1&2). The micrograph shows a brittle mode of failure. Notably, the micro pores seen in the micrographs do not display signs of either growth or merging, which, as literature suggests, is typically associated with ductile fracture mechanisms<sup>144</sup>.

On the other hand, the Cu-coated titanium exhibits a slightly different fracture morphology, as shown in Figure 9-4b(1&2). One of the features of these micrographs is the river-like patterns, or

"river markings". These are indicative of areas that underwent plastic deformation before succumbing to breakage. Their presence may also point towards the material's ability to absorb energy, followed by a tearing action leading to fracture. However, the crystallographic facets of the micrograph also show some degree of brittle failure. This combined failure mechanism offers a glimpse into the complex interactions at play between the titanium substrate and the copper coating, as well as the potential avenues for optimizing their mechanical performance in future endeavors.

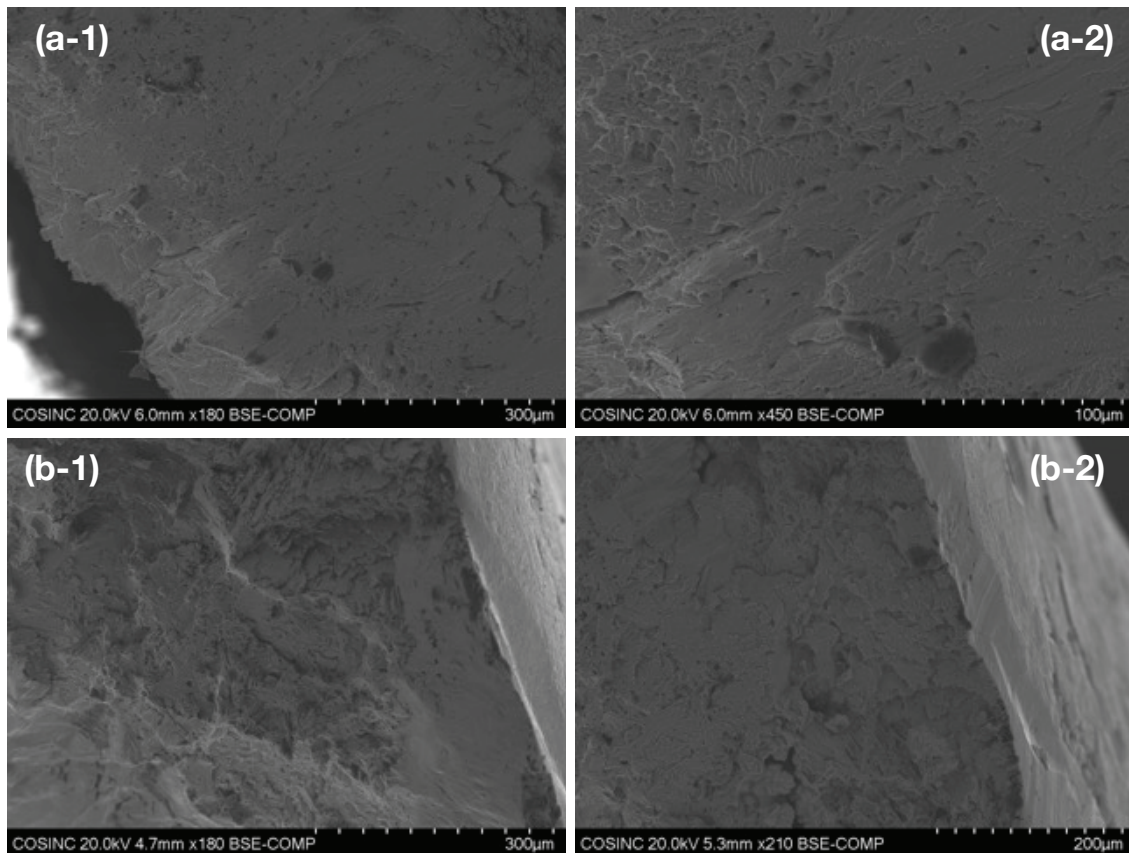


Figure 9-4: SEM images of the fracture microstructure of the (a) dense titanium after flash sintering, and (b) copper coated titanium after flash deposition

#### 9.4.4. Analysis of Coating Layer Thickness on Cu-coated-Ti

For a detailed analysis of the coating thickness, three distinct regions were chosen on the specimen as shown in Figure 9-5. The assessment approach involved taking the difference between the pre-

coating and post-coating thicknesses and then dividing this value by two. This provided an estimate of the layer thickness on each side of the dogbone gage.

A summary detailing the specimen's thickness at various stages – prior to sintering, post-sintering, and post-coating – is tabulated in Table 9-1. Our findings indicate that a majority of the regions featured a copper layer, approximately 50 $\mu\text{m}$  thick, seamlessly coated onto the titanium. However, certain areas displayed a thicker copper film on the titanium base.

Through microscopy, the computed average thickness of the coating layer is  $65 \pm 19 \mu\text{m}$ . This variance suggests that while the copper layer's deposition is continuous and devoid of voids, its thickness across the substrate isn't perfectly uniform.

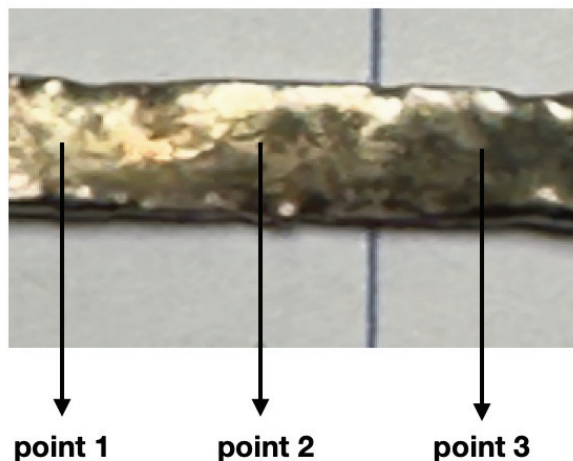


Figure 9-5: Phone capture image of copper coated titanium showing regions where copper layer thickness was measured.

Table 9-1: Summary of specimen thickness before and after coating. The points 1, 2 and 3 here in refers to the points highlighted in Figure 9-5.

	Green Ti	Dense Ti	Copper coating on Titanium		
			Point 1	Point 2	Point 3
Thickness (mm)	1.01	0.91	1.01	1.01	1.03
Cu layer Thickness ( $\mu\text{m}$ )	-	-	50	50	60

#### 9.4.5. Electrical Conductivity Enhancement of Cu-coated-Ti

Since copper is a highly conductive material, we measured its contribution to the electrical conductivity of the fabricated specimen. The evaluation process commenced by measuring the absolute resistance of the titanium specimen before copper coating. This preliminary measurement yielded a resistance of  $6.922\Omega$ , corresponding to a specific resistivity of  $61.4 \mu\Omega \text{ cm}$ . Following the flash deposition of copper, a marked enhancement in electrical conductivity was observed. The resistance dipped significantly, registering at  $6.24\mu\Omega$  when normalized to the pre-coating dimensions. This translates to a reduced specific resistivity of  $54.7 \mu\Omega \text{ cm}$ , signaling an improvement of around 10% in the specimen's electrical conductivity post copper coating. The summary of this result is given in Figure 9-6.

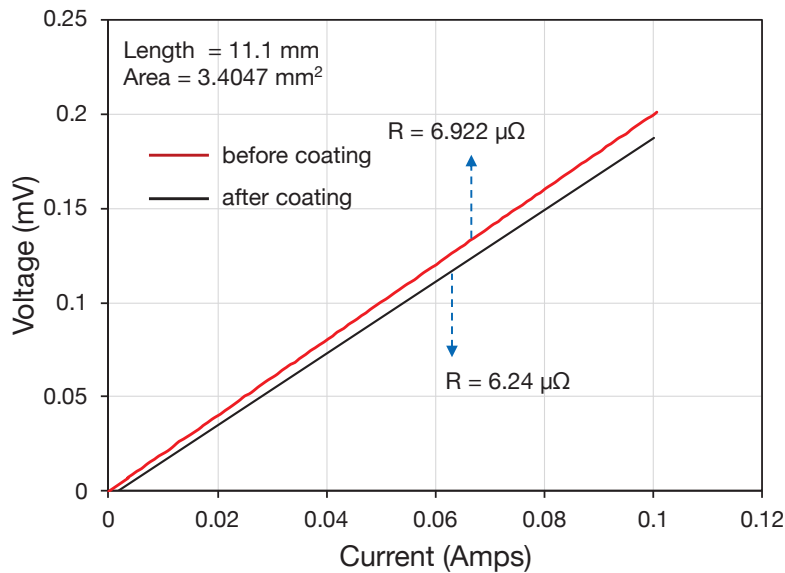


Figure 9-6: Voltage and Current relationship of the sintered titanium and Cu-coated-Ti after flash deposition. The measurement was done using a four-point probe measurement setup.

#### 9.5. Conclusion

This investigation successfully explored a new innovative procedure for achieving consistent metal coatings through direct current injection. Utilizing a 0.25 mm copper wire tightly coiled around a

16 mm gage length titanium dogbone, current was incrementally introduced until reaching a density of  $16.61 \text{ A mm}^{-2}$ , culminating in a mere 16s for the entire flash deposition process. Key insights gleaned from this exploration include:

1. SEM micrographs shows the bond between the copper and titanium layers, without any irregularities or gaps.
2. SEM insights into the copper layer revealed a consistent, unbroken coating.
3. Fracture morphological analysis discerns a mixed-mode failure mechanism in the Cu-coated-Ti specimen, as captured by the river markings and voids with no sign of growth.
4. Layer thickness evaluation via microscopy estimates it at  $65 \pm 19 \mu\text{m}$ , while 50 to 60  $\mu\text{m}$  thickness were recorded from caliper measurements.
5. A notable 10% improvement in the Ti substrate's electrical conductivity, attributed to the Cu coating introduced by flash deposition.

## Bibliography

1. Wilder, D. R. *Progress in Sintering*. (1962).
2. Kingery, W. D. Sintering from prehistoric times to the present. *Solid State Phenom.* **25**, 1–10 (1992).
3. German, R. M. History of sintering: empirical phase. *Powder Metall.* **56**, 117–123 (2013).
4. Mackenzie, J. K. & Shuttleworth, R. A phenomenological theory of sintering. *Proc. Phys. Soc. Sect. B* **62**, 833 (1949).
5. WALKER, R. F. Mechanism of material transport during sintering. *J. Am. Ceram. Soc.* **38**, 187–197 (1955).
6. Craik, R. L. *The Sintering of Metallic Powders*. (University of Glasgow (United Kingdom), 1952).
7. Jaffee, R. I. A brief review of refractory metals. (1959).
8. Johnson, J. L. 14 - Sintering of refractory metals. in *Woodhead Publishing Series in Metals and Surface Engineering* (ed. Fang, Z. Z. B. T.-S. of A. M.) 356–388 (Woodhead Publishing, 2010). doi:<https://doi.org/10.1533/9781845699949.3.356>.
9. Xin, Z. *et al.* Research development of refractory metal materials used in the field of aerospace. *Rare Met. Mater. Eng.* **10**, (2011).
10. Omole, S., Lunt, A., Kirk, S. & Shokrani, A. Advanced processing and machining of tungsten and its alloys. *J. Manuf. Mater. Process.* **6**, 15 (2022).
11. Malewar, R., Kumar, K. S., Murty, B. S., Sarma, B. & Pabi, S. K. On sinterability of nanostructured W produced by high-energy ball milling. *J. Mater. Res.* **22**, 1200–1206 (2007).
12. A. Millensifer, T., Sinclair, D., Jonasson, I. & Lipmann, A. Rhenium. *Crit. Met. Handb.* 340–360 (2014).
13. Cologna, M., Rashkova, B. & Raj, R. Flash sintering of nanograin zirconia in < 5 s at 850 C. *J. Am. Ceram. Soc.* **93**, 3556–3559 (2010).
14. Terauds, K. *et al.* Electroluminescence and the measurement of temperature during Stage III of flash sintering experiments. *J. Eur. Ceram. Soc.* **35**, 3195–3199 (2015).
15. Lebrun, J., Jha, S. K., McCormack, S. J., Kriven, W. M. & Raj, R. Broadening of diffraction peak widths and temperature nonuniformity during flash experiments. *J. Am. Ceram. Soc.* **99**, 3429–3434 (2016).
16. Bhandari, S., Mishra, T. P., Guillon, O., Yadav, D. & Bram, M. Accessing the role of Joule heating on densification during flash sintering of YSZ. *Scr. Mater.* **211**, 114508 (2022).
17. Yoon, B. *et al.* Measurement of O and Ti atom displacements in TiO<sub>2</sub> during flash sintering experiments. *J. Am. Ceram. Soc.* **101**, 1811–1817 (2018).
18. Jongmanns, M., Raj, R. & Wolf, D. E. Generation of Frenkel defects above the Debye temperature by proliferation of phonons near the Brillouin zone edge. *New J. Phys.* **20**, 093013 (2018).

19. Zapata-Solvas, E., Gómez-García, D., Domínguez-Rodríguez, A. & Todd, R. I. Ultra-fast and energy-efficient sintering of ceramics by electric current concentration. *Sci. Rep.* **5**, 8513 (2015).
20. Fang, Z. Z. *Sintering of advanced materials*. (Elsevier, 2010).
21. Mondal, A., Agrawal, D. & Upadhyaya, A. Microwave sintering of refractory metals/alloys: W, Mo, Re, W-Cu, W-Ni-Cu and W-Ni-Fe alloys. *J. Microw. Power Electromagn. Energy* **44**, 28–44 (2010).
22. Prabhu, G., Chakraborty, A. & Sarma, B. Microwave sintering of tungsten. *Int. J. Refract. Met. Hard Mater.* **27**, 545–548 (2009).
23. Byun, J. M., Lee, E. S., Heo, Y. J., Jeong, Y.-K. & Oh, S.-T. Consolidation and properties of tungsten by spark plasma sintering and hot isostatic pressing. *Int. J. Refract. Met. Hard Mater.* **99**, 105602 (2021).
24. Hu, B. *et al.* Densification behavior of tungsten alloy powders during hot isostatic pressing. *Mater. Today Commun.* **31**, 103576 (2022).
25. Martínez, C. *et al.* Effect of hot pressing and hot isostatic pressing on the microstructure, hardness, and wear behavior of nickel. *Mater. Lett.* **273**, 127944 (2020).
26. Tan, C. *et al.* Selective laser melting of high-performance pure tungsten: parameter design, densification behavior and mechanical properties. *Sci. Technol. Adv. Mater.* **19**, 370–380 (2018).
27. Iveković, A. *et al.* Selective laser melting of tungsten and tungsten alloys. *Int. J. Refract. Met. Hard Mater.* **72**, 27–32 (2018).
28. Braun, J. *et al.* Molybdenum and tungsten manufactured by selective laser melting: Analysis of defect structure and solidification mechanisms. *Int. J. Refract. Met. Hard Mater.* **84**, 104999 (2019).
29. Zhou, L. *et al.* Microstructure tailoring to enhance strength and ductility in pure tantalum processed by selective laser melting. *Mater. Sci. Eng. A* **785**, 139352 (2020).
30. Deng, S. *et al.* Spark plasma sintering of pure tungsten powder: Densification kinetics and grain growth. *Powder Technol.* **310**, 264–271 (2017).
31. Lee, G., McKittrick, J., Ivanov, E. & Olevsky, E. A. Densification mechanism and mechanical properties of tungsten powder consolidated by spark plasma sintering. *Int. J. Refract. Met. Hard Mater.* **61**, 22–29 (2016).
32. Ganesh, V. *et al.* Manufacturing of W/steel composites using electro-discharge sintering process. *Nucl. Mater. Energy* **30**, 101089 (2022).
33. Coble, R. L. A model for boundary diffusion controlled creep in polycrystalline materials. *J. Appl. Phys.* **34**, 1679–1682 (1963).
34. German, R. M. 1 - Thermodynamics of sintering. in *Woodhead Publishing Series in Metals and Surface Engineering* (ed. Fang, Z. Z. B. T.-S. of A. M.) 3–32 (Woodhead Publishing, 2010). doi:<https://doi.org/10.1533/9781845699949.1.3>.
35. Kang, S.-J. L. *Sintering: densification, grain growth and microstructure*. (Elsevier, 2004).

36. Moya, J. S., Baudín, C. & Miranzo, P. Sintering. in (ed. Meyers, R. A. B. T.-E. of P. S. and T. (Third E.) 865–878 (Academic Press, 2003). doi:<https://doi.org/10.1016/B0-12-227410-5/00694-3>.
37. German, R. M., Bourguignon, L. L. & Rabin, B. H. Critical developments in tungsten heavy alloys. *Powder Met.* **5**, (1992).
38. German, R. M. & Munir, Z. A. Enhanced low-temperature sintering of tungsten. *Metall. Trans. A* **7**, 1873–1877 (1976).
39. Mondal, A., Upadhyaya, A. & Agrawal, D. Effect of heating mode on sintering of tungsten. *Int. J. Refract. Met. Hard Mater.* **28**, 597–600 (2010).
40. Bose, A., Klotz, B. R., Kellogg, F. R., Cho, K. C. & Dowding, R. J. Nanocrystalline Tungsten Powder Synthesis Using High Energy Milling. in *Proc. 2008 Intl Conf on W, Refract & Hardmetals VII, Publ MPIF* 5–35 (2008).
41. Wang, H., Fang, Z. Z. & Siddle, D. Study of size-dependent sintering behavior of tungsten powders. in *Proc. 2008 Intl Conf on W, Refract & Hardmetals VII, Publ MPIF* 5–72 (2008).
42. Oda, E., Ameyama, K. & Yamaguchi, S. Fabrication of nano grain tungsten compact by mechanical milling process and its high temperature properties. in *Materials Science Forum* vol. 503 573–578 (Trans Tech Publ, 2006).
43. Kothari, N. C. Sintering kinetics in tungsten powder. *J. Common Met.* **5**, 140–150 (1963).
44. Vasilos, T. & Smith, J. T. Diffusion mechanism for tungsten sintering kinetics. *J. Appl. Phys.* **35**, 215–217 (1964).
45. Raj, R. Analysis of the power density at the onset of flash sintering. *J. Am. Ceram. Soc.* **99**, 3226–3232 (2016).
46. Prette, A. L. G., Cologna, M., Sglavo, V. & Raj, R. Flash-sintering of Co<sub>2</sub>MnO<sub>4</sub> spinel for solid oxide fuel cell applications. *J. Power Sources* **196**, 2061–2065 (2011).
47. Cologna, M., Prette, A. L. G. & Raj, R. Flash-sintering of cubic yttria-stabilized zirconia at 750° C for possible use in SOFC manufacturing. *J. Am. Ceram. Soc.* **94**, 316–319 (2011).
48. Jha, S. K. & Raj, R. The effect of electric field on sintering and electrical conductivity of titania. *J. Am. Ceram. Soc.* **97**, 527–534 (2014).
49. Cologna, M., Francis, J. S. C. & Raj, R. Field assisted and flash sintering of alumina and its relationship to conductivity and MgO-doping. *J. Eur. Ceram. Soc.* **31**, 2827–2837 (2011).
50. Yoshida, H., Sakka, Y., Yamamoto, T., Lebrun, J.-M. & Raj, R. Densification behaviour and microstructural development in undoped yttria prepared by flash-sintering. *J. Eur. Ceram. Soc.* **34**, 991–1000 (2014).
51. M’Peko, J.-C., Francis, J. S. C. & Raj, R. Field-assisted sintering of undoped BaTiO<sub>3</sub>: Microstructure evolution and dielectric permittivity. *J. Eur. Ceram. Soc.* **34**, 3655–3660 (2014).
52. Yoon, B., Avila, V., Raj, R. & Jesus, L. M. Reactive flash sintering of the entropy-stabilized oxide Mg<sub>0.2</sub>Ni<sub>0.2</sub>Co<sub>0.2</sub>Cu<sub>0.2</sub>Zn<sub>0.2</sub>O. *Scr. Mater.* **181**, 48–52 (2020).

53. Avila, V. & Raj, R. Reactive flash sintering of powders of four constituents into a single phase of a complex oxide in a few seconds below 700° C. *J. Am. Ceram. Soc.* **102**, 6443–6448 (2019).
54. Kumar MK, P., Yadav, D., Lebrun, J. & Raj, R. Flash sintering with current rate: A different approach. *J. Am. Ceram. Soc.* **102**, 823–835 (2019).
55. Park, J. & Chen, I. In Situ Thermometry Measuring Temperature Flashes Exceeding 1,700 C in 8 mol% Y<sub>2</sub>O<sub>3</sub>-Stabilized Zirconia Under Constant-Voltage Heating. *J. Am. Ceram. Soc.* **96**, 697–700 (2013).
56. Narayan, J. A new mechanism for field-assisted processing and flash sintering of materials. *Scr. Mater.* **69**, 107–111 (2013).
57. Holland, T. B., Anselmi-Tamburini, U., Quach, D. V., Tran, T. B. & Mukherjee, A. K. Effects of local Joule heating during the field assisted sintering of ionic ceramics. *J. Eur. Ceram. Soc.* **32**, 3667–3674 (2012).
58. Raj, R. Joule heating during flash-sintering. *J. Eur. Ceram. Soc.* **32**, 2293–2301 (2012).
59. Raj, R., Kulkarni, A., Lebrun, J.-M. & Jha, S. Flash sintering: A new frontier in defect physics and materials science. *MRS Bull.* **46**, 36–43 (2021).
60. Mishra, T. P. *et al.* On the role of Debye temperature in the onset of flash in three oxides. *Scr. Mater.* **170**, 81–84 (2019).
61. Lebrun, J. *et al.* In-situ measurements of lattice expansion related to defect generation during flash sintering. *J. Am. Ceram. Soc.* **100**, 4965–4970 (2017).
62. Shikhar, F. A study on Flash Sintering and Related Phenomena in Titania and its Composites with Alumina.
63. Kumar MK, P., Yadav, D., Lebrun, J. & Raj, R. Flash sintering with current rate: A different approach. *J. Am. Ceram. Soc.* **102**, 823–835 (2019).
64. Katz, J. D. Microwave sintering of ceramics. *Annu. Rev. Mater. Sci.* **22**, 153–170 (1992).
65. Anselmi-Tamburini, U., Gennari, S., Garay, J. E. & Munir, Z. A. Fundamental investigations on the spark plasma sintering/synthesis process: II. Modeling of current and temperature distributions. *Mater. Sci. Eng. A* **394**, 139–148 (2005).
66. Grasso, S. *et al.* Flash spark plasma sintering (FSPS) of  $\alpha$  and  $\beta$  SiC. *J. Am. Ceram. Soc.* **99**, 1534–1543 (2016).
67. Cologna, M., Rashkova, B. & Raj, R. Flash sintering of nanograin zirconia in <5 s at 850°C. *J. Am. Ceram. Soc.* **93**, 3556–3559 (2010).
68. Gil-González, E., Pérez-Maqueda, L. A., Sánchez-Jiménez, P. E. & Perejón, A. Flash Sintering Research Perspective: A Bibliometric Analysis. *Materials* **15**, 416 (2022).
69. Spark plasma sintering of silicon nitride/silicon carbide nanocomposites with reduced additive amounts - ScienceDirect. <https://www.sciencedirect.com/science/article/pii/S1359646205003349>.
70. Yu, M., Grasso, S., Mckinnon, R., Saunders, T. & Reece, M. J. Review of flash sintering: materials, mechanisms and modelling. *Adv. Appl. Ceram.* **116**, 24–60 (2017).

71. Kermani, M., Hu, C. & Grasso, S. From pit fire to Ultrafast High-temperature Sintering (UHS): A review on ultrarapid consolidation. *Ceram. Int.* (2022) doi:10.1016/j.ceramint.2022.11.091.
72. Guo, J. *et al.* Cold Sintering: A Paradigm Shift for Processing and Integration of Ceramics. *Angew. Chem. Int. Ed.* **55**, 11457–11461 (2016).
73. Raj, Rishi & Wolf, Dietrich, et al. On the confluence of ultrafast heating rate sintering and flash sintering phenomena. *J. Am. Ceram. Soc.* **in press**, (2023).
74. Terauds, K. *et al.* Electroluminescence and the measurement of temperature during Stage III of flash sintering experiments. *J. Eur. Ceram. Soc.* **35**, 3195–3199 (2015).
75. Lebrun, J. & Raj, R. A first report of photoemission in experiments related to flash sintering. *J. Am. Ceram. Soc.* **97**, 2427–2430 (2014).
76. Lebrun, J. *et al.* Emergence and extinction of a new phase during on–off experiments related to flash sintering of 3 YSZ. *J. Am. Ceram. Soc.* **98**, 1493–1497 (2015).
77. Lebrun, J. *et al.* In-situ measurements of lattice expansion related to defect generation during flash sintering. *J. Am. Ceram. Soc.* **100**, 4965–4970 (2017).
78. Clemenceau, T. & Raj, R. Higher conductivity of non-stoichiometric lithium lanthanum zirconate ceramics made by reactive flash synthesis. *MRS Commun.* **12**, 201–205 (2022).
79. Mishra, T. P., Neto, R. R. I., Raj, R., Guillou, O. & Bram, M. Current-rate flash sintering of gadolinium doped ceria: Microstructure and Defect generation. *Acta Mater.* **189**, 145–153 (2020).
80. Yurlova, M. S. *et al.* Electric pulse consolidation: an alternative to spark plasma sintering. *J. Mater. Sci.* **49**, 952–985 (2014).
81. Hiernaut, J.-P., Sakuma, F. & Ronchi, C. Determination of the melting point and the emissivity of refractory metals with a six-wavelength pyrometer. *High Temp. High Press. Print* **21**, 139–148 (1989).
82. Jones, H. A. A Temperature Scale for Tungsten. *Phys. Rev.* **28**, 202–207 (1926).
83. Mishra, T. P., Neto, R. R. I., Raj, R., Guillou, O. & Bram, M. Current-rate flash sintering of gadolinium doped ceria: Microstructure and Defect generation. *Acta Mater.* **189**, 145–153 (2020).
84. Yadav, D. & Raj, R. Two unique measurements related to flash experiments with yttria-stabilized zirconia. *J. Am. Ceram. Soc.* **100**, 5374–5378 (2017).
85. Mishra, T. P. *et al.* On the role of Debye temperature in the onset of flash in three oxides. *Scr. Mater.* **170**, 81–84 (2019).
86. Jongmanns, M., Raj, R. & Wolf, D. E. Generation of Frenkel defects above the Debye temperature by proliferation of phonons near the Brillouin zone edge. *New J. Phys.* **20**, 093013 (2018).
87. Tan, C. *et al.* Selective laser melting of high-performance pure tungsten: parameter design, densification behavior and mechanical properties. *Sci. Technol. Adv. Mater.* **19**, 370–380 (2018).

88. Mazo, I., Molinari, A. & Sglavo, V. M. Electrical resistance flash sintering of tungsten carbide. *Mater. Des.* **213**, 110330 (2022).
89. McWilliams, B., Yu, J., Kellogg, F. & Kilczewski, S. Enhanced Sintering Kinetics in Aluminum Alloy Powder Consolidated Using DC Electric Fields. *Metall. Mater. Trans. A* **48**, 919–929 (2017).
90. Mazo, I., Molinari, A. & Sglavo, V. M. Electrical resistance flash sintering of tungsten carbide. *Mater. Des.* **213**, 110330 (2022).
91. Ingraci Neto, R. R. & Raj, R. The flash effect in electronic conductors: The case of amorphous carbon fibers. *Scr. Mater.* **179**, 20–24 (2020).
92. Coolidge, W.D. TUNGSTEN AND METHOD OF MAKING THE SAME FOR USE AS FILAMENTS OF INCANDESCENT ELECTRIC AMPS AND FOR OTHER PURPOSES. (1913).
93. Raj, R. & King, G. Life prediction of tungsten filaments in incandescent lamps. *Metall. Trans. A* **9**, 941–946 (1978).
94. Raj, R. Analysis of the Power Density at the Onset of Flash Sintering. *J. Am. Ceram. Soc.* **99**, 3226–3232 (2016).
95. Bamidele, Emmanuel, Raj, Rishi, & Jalali, I. A. Syed. Flash sintering of tungsten in a few seconds at 1400 oC. (2023).
96. Köster, U. *et al.* In-pile arrangements of reactor-based RIB facilites. *Nucl. Instrum. Methods Phys. Res. Sect. B Beam Interact. Mater. At.* **126**, 253–257 (1997).
97. McClure, J., Boboridis, K. & Cezairliyan, A. Radiance temperatures (in the wavelength range 521 to 1500 nm) of rhenium and iridium at their melting points by a pulse-heating technique. *Int. J. Thermophys.* **20**, 1137–1148 (1999).
98. Separation of Cavitation-Strain and Creep-Strain During Deformation - Raj - 1982 - Journal of the American Ceramic Society - Wiley Online Library. <https://ceramics.onlinelibrary.wiley.com/doi/abs/10.1111/j.1151-2916.1982.tb10397.x>.
99. Bryskin, B. D. Evaluation of properties and special features for high-temperature applications of rhenium. in vol. 246 278–291 (American Institute of Physics, 1992).
100. Mishra, T. P., Neto, R. R. I., Raj, R., Guillou, O. & Bram, M. Current-rate flash sintering of gadolinium doped ceria: Microstructure and Defect generation. *Acta Mater.* **189**, 145–153 (2020).
101. Bonny, G., Bakaev, A., Terentyev, D. & Mastrikov, Y. A. Interatomic potential to study plastic deformation in tungsten-rhenium alloys. *J. Appl. Phys.* **121**, (2017).
102. Shewmon, P. G. *Diffusion in Solids*. (McGraw-Hill, 1963).
103. Jalali, S. I. A. & Raj, R. Reactive flash sintering in a bilayer of zirconia and lanthana: Measurement of the diffusion coefficient in real time. *J. Am. Ceram. Soc.* **n/a**,
104. Motomura, H., Tamao, D., Nambu, K., Masuda, H. & Yoshida, H. Athermal effect of flash event on high-temperature plastic deformation in Y2O3-stabilized tetragonal ZrO<sub>2</sub> polycrystal. *J. Eur. Ceram. Soc.* **42**, 5045–5052 (2022).

105. Jalali, S. I. A. & Raj, R. Touch-free flash sintering with magnetic induction within a reactor activated by the usual flash method. *J. Am. Ceram. Soc.* **n/a**, 2022;1–6 (2022).
106. Lebrun, J.-M. *et al.* Emergence and extinction of a new phase during on-off experiments related to flash sintering of 3YSZ. *J. Am. Ceram. Soc.* **98**, 1493–1497 (2015).
107. Clemenceau, T. & Raj, R. Higher conductivity of non-stoichiometric lithium lanthanum zirconate ceramics made by reactive flash synthesis. *MRS Commun.* (2022) doi:10.1557/s43579-022-00162-z.
108. Fralch, J. & Kingery, W. D. Thermal Conductivity: IX, Experimental Investigation of Effect of Porosity on Thermal Conductivity. *J. Am. Ceram. Soc.* **37**, 99–107 (1954).
109. Francis, J. S. C. & Raj, R. Influence of the Field and the Current Limit on Flash Sintering at Isothermal Furnace Temperatures. *J. Am. Ceram. Soc.* **96**, 2754–2758 (2013).
110. Terauds, K. *et al.* Electroluminescence and the measurement of temperature during Stage III of flash sintering experiments. *J. Eur. Ceram. Soc.* **35**, 3195–3199 (2015).
111. Yousuf, M., Sahu, P. C. & Rajan, K. G. High-pressure and high-temperature electrical resistivity of ferromagnetic transition metals: Nickel and iron. *Phys. Rev. B* **34**, 8086–8086 (1986).
112. Sullivan, J., Krishna, A. & Lee, J. Porous Nickel as a Selective Emitter for Surface Cooling in Various Environments. in 915–920 (IEEE, 2018).
113. Srivatsan, T. S., Narendra, N. & Troxell, J. D. Tensile deformation and fracture behavior of an oxide dispersion strengthened copper alloy. *Mater. Des.* **21**, 191–198 (2000).
114. Guo, M. X., Wang, M. P., Shen, K., Cao, L. F. & Tan, W. Tensile fracture behavior characterization of dispersion strengthened copper alloys. *J. Alloys Compd.* **469**, 488–498 (2009).
115. Taylor, P. G., d'Ortigue, O. L., Francoeur, M. & Trudeau, N. Final energy use in IEA countries: The role of energy efficiency. *Energy Policy* **38**, 6463–6474 (2010).
116. Vayre, B., Vignat, F. & Villeneuve, F. Metallic additive manufacturing: state-of-the-art review and prospects. *Mech. Ind.* **13**, 89–96 (2012).
117. Benedikt, O., Šúcha, P. & Hanzálek, Z. On Idle Energy Consumption Minimization in Production: Industrial Example and Mathematical Model. *ArXiv Prepr. ArXiv200506270* (2020).
118. Upadhyaya, A., Tiwari, S. K. & Mishra, P. Microwave sintering of W–Ni–Fe alloy. *Scr. Mater.* **56**, 5–8 (2007).
119. Wong, W. L. E. & Gupta, M. Improving overall mechanical performance of magnesium using nano-alumina reinforcement and energy efficient microwave assisted processing route. *Adv. Eng. Mater.* **9**, 902–909 (2007).
120. Minier, L., Le Gallet, S., Grin, Y. & Bernard, F. A comparative study of nickel and alumina sintering using spark plasma sintering (SPS). *Mater. Chem. Phys.* **134**, 243–253 (2012).
121. Rajagopalan, P. K., Desai, S. V., Kalghatgi, R. S., Krishnan, T. S. & Bose, D. K. Studies on the electric discharge compaction of metal powders. *Mater. Sci. Eng. A* **280**, 289–293 (2000).

122. Kim, D. K., Pak, H.-R. & Okazaki, K. Electrodischarge compaction of nickel powders. *Mater. Sci. Eng. A* **104**, 191–200 (1988).
123. Yap, C. Y., Tan, H. K., Du, Z., Chua, C. K. & Dong, Z. Selective laser melting of nickel powder. *Rapid Prototyp. J.* **23**, 750–757 (2017).
124. Guo, M. *et al.* Selective laser melting additive manufacturing of pure tungsten: Role of volumetric energy density on densification, microstructure and mechanical properties. *Int. J. Refract. Met. Hard Mater.* **84**, 105025 (2019).
125. Attar, H., Calin, M., Zhang, L. C., Scudino, S. & Eckert, J. Manufacture by selective laser melting and mechanical behavior of commercially pure titanium. *Mater. Sci. Eng. A* **593**, 170–177 (2014).
126. Nirish, M. & Rajendra, R. Optimization of process parameter and additive simulation for fatigue strength development by selective laser melting of AlSi10Mg alloy. *Int. J. Mech. Eng.* **7**, 3795–3802 (2022).
127. Ciurana, J., Hernandez, L. & Delgado, J. Energy density analysis on single tracks formed by selective laser melting with CoCrMo powder material. *Int. J. Adv. Manuf. Technol.* **68**, 1103–1110 (2013).
128. Bertoli, U. S., Wolfer, A. J., Matthews, M. J., Delplanque, J.-P. R. & Schoenung, J. M. On the limitations of volumetric energy density as a design parameter for selective laser melting. *Mater. Des.* **113**, 331–340 (2017).
129. Wei, Q. S. *et al.* Effects of the processing parameters on the forming quality of stainless steel parts by Selective Laser Melting. *Adv. Mater. Res.* **189**, 3668–3671 (2011).
130. Yerokhin, A., Nie, X., Leyland, A., Matthews, A. & Dowey, S. Plasma electrolysis for surface engineering. *Surf. Coat. Technol.* **122**, 73–93 (1999).
131. Grujicic, D. & Pesic, B. Electrodeposition of copper: the nucleation mechanisms. *Electrochimica Acta* **47**, 2901–2912 (2002).
132. Story, H. & Hoffman, R. Stress annealing in vacuum deposited copper films. *Proc. Phys. Soc. Sect. B* **70**, 950 (1957).
133. Moridi, A., Hassani-Gangaraj, S. M., Guagliano, M. & Dao, M. Cold spray coating: review of material systems and future perspectives. *Surf. Eng.* **30**, 369–395 (2014).
134. Xu, B., Zhu, Z., Ma, S., Zhang, W. & Liu, W. Sliding wear behavior of Fe–Al and Fe–Al/WC coatings prepared by high velocity arc spraying. *Wear* **257**, 1089–1095 (2004).
135. Wilden, J., Wank, A. & Schreiber, F. Wires for Arc and High Velocity Flame Spraying—Wire Design, Materials, and Coating Properties. in 609–617 (ASM International, 2000).
136. Huang, Y. *et al.* Antibacterial efficacy, corrosion resistance, and cytotoxicity studies of copper-substituted carbonated hydroxyapatite coating on titanium substrate. *J. Mater. Sci.* **50**, 1688–1700 (2015).
137. He, X. *et al.* Biocompatibility, corrosion resistance and antibacterial activity of TiO<sub>2</sub>/CuO coating on titanium. *Ceram. Int.* **43**, 16185–16195 (2017).

138. Leśniak-Ziółkowska, K. *et al.* Plasma electrolytic oxidation as an effective tool for production of copper incorporated bacteriostatic coatings on Ti-15Mo alloy. *Appl. Surf. Sci.* **563**, 150284 (2021).
139. Rosa, J. L., Robin, A., Silva, M., Baldan, C. A. & Peres, M. P. Electrodeposition of copper on titanium wires: Taguchi experimental design approach. *J. Mater. Process. Technol.* **209**, 1181–1188 (2009).
140. Maddu, J., Karrolla, B., Shaik, R. U. & Burdhuhos-Nergis, D.-P. SWOT Analysis of Electrical Discharge Coatings: A Case Study of Copper Coating on Titanium Alloy. *Surfaces* **5**, 290–307 (2022).
141. Wang, L. *et al.* Osteoblast response to copper-doped microporous coatings on titanium for improved bone integration. *Nanoscale Res. Lett.* **16**, 1–15 (2021).
142. Tan, W., Zhou, Y., Kerr, H. & Lawson, S. A study of dynamic resistance during small scale resistance spot welding of thin Ni sheets. *J. Phys. Appl. Phys.* **37**, 1998 (2004).
143. Kim, D. K., Pak, H.-R. & Okazaki, K. Electrodissolve compaction of nickel powders. *Mater. Sci. Eng. A* **104**, 191–200 (1988).
144. Pantazopoulos, G. A. A short review on fracture mechanisms of mechanical components operated under industrial process conditions: Fractographic analysis and selected prevention strategies. *Metals* **9**, 148 (2019).

ProQuest Number: 30811736

INFORMATION TO ALL USERS

The quality and completeness of this reproduction is dependent on the quality  
and completeness of the copy made available to ProQuest.



Distributed by ProQuest LLC (2023).

Copyright of the Dissertation is held by the Author unless otherwise noted.

This work may be used in accordance with the terms of the Creative Commons license  
or other rights statement, as indicated in the copyright statement or in the metadata  
associated with this work. Unless otherwise specified in the copyright statement  
or the metadata, all rights are reserved by the copyright holder.

This work is protected against unauthorized copying under Title 17,  
United States Code and other applicable copyright laws.

Microform Edition where available © ProQuest LLC. No reproduction or digitization  
of the Microform Edition is authorized without permission of ProQuest LLC.

ProQuest LLC  
789 East Eisenhower Parkway  
P.O. Box 1346  
Ann Arbor, MI 48106 - 1346 USA